

Article

Ge-Hg-Rich Sphalerite and Pb, Sb, As, Hg, and Ag Sulfide Assemblages in Mud Volcanoes of Sakhalin Island, Russia: An Insight into Possible Origin

Ella V. Sokol¹, Svetlana N. Kokh^{1,*}, Anna V. Nekipelova¹, Adam Abersteiner^{2,3}, Yurii V. Seryotkin^{1,4}, Valeriy V. Ershov⁵, Olga A. Nikitenko⁵ and Anna S. Deviatiiarova¹

¹ Sobolev Institute of Geology and Mineralogy Siberian Branch Russian Academy of Sciences, 3 Koptyug Avenue, 630090 Novosibirsk, Russia; sokol@igm.nsc.ru or sokol_ag@mail.ru (E.V.S.); nekipelova@igm.nsc.ru (A.V.N.); uvs@igm.nsc.ru (Y.V.S.); devyatiyarova@igm.nsc.ru (A.S.D.)

² Department of Geosciences and Geography (GeoHel), University of Helsinki, P.O. Box 64, FIN-00014 10 Helsinki, Finland; adam.abersteiner@helsinki.fi

³ Institute of Volcanology and Seismology, Far East Branch, Russian Academy of Sciences, 683006 Petropavlovsk-Kamchatsky, Russia

⁴ Department of Geology and Geophysics, Novosibirsk State University, 2 Pirogov Street, 630090 Novosibirsk, Russia

⁵ Institute of Marine Geology and Geophysics Far Eastern Branch Russian Academy of Science, 1B, Nauki Street, 693022 Yuzhno-Sakhalinsk, Russia; valery_ershov@mail.ru (V.V.E.); nikitenko.olga@list.ru (O.A.N.)

* Correspondence: s.n.kokh@gmail.com or zateeva@igm.nsc.ru



Citation: Sokol, E.V.; Kokh, S.N.; Nekipelova, A.V.; Abersteiner, A.; Seryotkin, Y.V.; Ershov, V.V.; Nikitenko, O.A.; Deviatiiarova, A.S. Ge-Hg-Rich Sphalerite and Pb, Sb, As, Hg, and Ag Sulfide Assemblages in Mud Volcanoes of Sakhalin Island, Russia: An Insight into Possible Origin. *Minerals* **2021**, *11*, 1186. <https://doi.org/10.3390/min11111186>

Academic Editors: Gheorghe Damian, Andrei Buzatu and Andrei Ionuț Apopei

Received: 30 September 2021

Accepted: 23 October 2021

Published: 26 October 2021

Publisher's Note: MDPI stays neutral with regard to jurisdictional claims in published maps and institutional affiliations.



Copyright: © 2021 by the authors. Licensee MDPI, Basel, Switzerland. This article is an open access article distributed under the terms and conditions of the Creative Commons Attribution (CC BY) license (<https://creativecommons.org/licenses/by/4.0/>).

Abstract: We characterize the mineralogy and geochemistry of Fe, Zn, Pb, Sb, As, Hg, Ag sulfide assemblages from mud masses currently extruded by the onshore South Sakhalin and Pugachev mud volcanoes (Sakhalin Island, Russia). Abundant TI-rich pyrite in sulfide concentrate samples from the mud volcanoes coexists with common Hg- and Ge-rich sphalerite, as well as with sporadic boulangerite, robinsonite, bournonite, galena, realgar, metacinnabar, cinnabar, acanthite, and chalcopyrite. Sphalerites are remarkably enriched in Hg (locally reaching 27 wt%) and coupled with permanent abnormal enrichment in Ge (3008–3408 ppm). According to single-crystal XRD analyses and Raman spectroscopy, both Hg-poor and Hg-rich sphalerites are single-phase (Zn,Hg)₃S₄ compounds. Pyrite is of diagenetic origin, judging by its trace-element chemistry, particular morphology, and heavy S isotope composition. Another assemblage, composed of Pb-Sb-(Hg) sulfide minerals and lesser As, Cu, Ag, and Bi compounds, results from hydrothermal alteration and is genetically related to Neogene volcano-sedimentary rocks found among the ejecta of the mud volcanoes. The composition of impurities in sphalerite from mud masses indicates crystallization at temperatures lower than ~100 °C, under the leaching effect of mud volcano waters.

Keywords: sphalerite; metacinnabar; cinnabar; ZnS-HgS series; Pb-Sb sulfosalts; LA-ICPMS; mud volcano; Sakhalin; trace-element partitioning

1. Introduction

Chemically pure ZnS varieties are rare in nature. Sphalerite commonly contains a few wt% of Fe or Mn, and smaller amounts of Cd, Hg, and/or Se, which occur as impurities and rarely reach high concentrations [1]. Unusual sphalerites rich in three of the latter elements are restricted to particular environments. Sphalerites bearing mercury are known from various localities around the world and are the dominant Hg-carriers in some deposits. For instance, exceptionally high contents of Hg (up to 16.35 wt% or ~0.08 apfu Hg) were reported [2] from the Eskay Creek deposit (British Columbia, Canada). Sphalerites with high and moderate Hg contents and sometimes with high Cd are frequently found in association with zincian metacinnabar and/or cinnabar in commercial Hg deposits (e.g.,

Nikitovka in the Ukraine, Khaidarkan in Kyrgyzstan, or Aktash in Siberia, Russia), as well as in numerous occurrences within the Central Asian and Altai-Sayan mercury belts (e.g., Kadyrel in Siberia, Russia, Idermeg–Bayan-Khan-Ula in Mongolia, or Jijikurt in Kazakhstan), which contain between 2.0 and 30.0 wt% Hg (~0.01 to ~0.18 apfu Hg) [3]. Cd-Hg- and Hg-sphalerites were also reported from complex Hg-bearing Au and Hg-Zn-Fe deposits. Unique high-Hg sphalerites with 21.6–45.5 wt% Hg (~0.11 to ~0.29 apfu Hg) in zoned and 37.0–38.7 wt% (~0.23–0.24 apfu Hg) in unzoned grains were found in the Levigliani Hg-Zn-Fe sulfide deposit in Tuscany, Italy [4]. The nearby Monte Arsiccio deposit [5] is second after the Big Creek Hg-bearing antimony deposit (Big Creek district, Valley County, ID, USA) to host the Zn-Hg sulfide polhemusite ($\text{Zn}_{0.87}\text{Hg}_{0.15}\text{S}$, tetragonal with 26 wt% Hg), an extremely rare metastable tetragonal (Zn,Hg)S polymorph [6].

On the other hand, low-iron sphalerite is the most common Ge carrier [7] reported from numerous low-temperature sulfide Zn-Pb-Cu-(Ba) deposits all over the world [1,8,9], with Ge grades most often ranging from few tens to several hundreds of ppm, ~200 ppm on average [1,8–12]. Sphalerites from several deposits, such as Tres Marias in Mexico [1,13–15] or Saint-Salvy in France [9], and the occurrences of the Freiberg district in Germany [16], contain more than 1000 ppm Ge, locally up to ~3000 ppm, with an average of ~1500 ppm.

This study focuses on unusual sphalerite with abnormal uniform Ge enrichment (~3100 ppm on average) and unevenly distributed Hg reaching 27 wt%. In addition to its unusual composition, the Ge-Hg-rich sphalerites occur in a particular environment: in the mud masses extruded by two largest mud volcanic edifices of South Sakhalin and Pugachev from Sakhalin Island, a 950 km long and 25–170 km wide island in the Russian Far East. The recent geodynamics of the area has been controlled by its location at the convergent boundaries of the Eurasian, Okhotsk, North American, and Pacific Plates. Being a part of the Sakhalin-Hokkaido orogenic belt, the island, along with the Kamchatka Peninsula, is among the most active seismic regions of Russia [17–20]. The Sakhalin mud volcanism is an effect of the high regional seismicity.

According to the chemical criteria formulated by Cook and coauthors [14], the Sakhalin sphalerites are classified as extreme due to their Hg and Ge enrichment. Analyses by several physical methods in this study provided new data on sphalerite crystal chemistry, natural ZnS-HgS solid solutions, and phase relationships, allowing for an improved understanding of substitution mechanisms at high concentrations of Ge and Hg. The results have implications for the ranges of natural ZnS-HgS series and possible geological controls on sphalerite chemistry in mud volcanic environments. A special challenge has been to constrain the source of high Zn, Hg, Ge and some other chalcophile elements (Pb, Sb, As) in the Sakhalin mud volcanoes (MVs).

2. Background Geology

2.1. Local Geology

The present-day tectonic framework of the area (Figure 1a) includes the West and East Sakhalin uplifts separated by the Central Sakhalin graben, as well as the Central depression between the West Sakhalin uplift and the Central Sakhalin fold-thrust belt. The graben, interpreted as a Jurassic subduction zone, is filled with 2 to 8 km of unconsolidated Cenozoic sediments and is bounded by the West-Sakhalin and Tym-Poronay fault systems, which generated many large earthquakes in the Sea of Japan and in Sakhalin Island. The regional Tym-Poronay and East Sakhalin faults stretch all along Sakhalin Island and extend into Hokkaido Island as the Hidaku belt [19–21].

Sakhalin Island belongs to a relict zone of Late Mesozoic-mid-Miocene subduction of the Okhotsk plate beneath the eastern Eurasian margin [17,22]. Its geological structure, with well-defined N–S tectonic zoning, formed in a number of tectonic settings and deformation fronts, but it mainly shaped up during the Alpine orogeny (Figure 1). Most of the island is composed of Late Cretaceous and Early Cenozoic strata arranged in lineaments that mark main accretion stages [23,24]. Several Paleozoic blocks may be remnant islands accreted during the subduction [25]. One such block in the southern part of Sakhalin within

the East Sakhalin uplift represents the basement uplifted during a collision with the Kurile forearc (Susunai metamorphic complex).

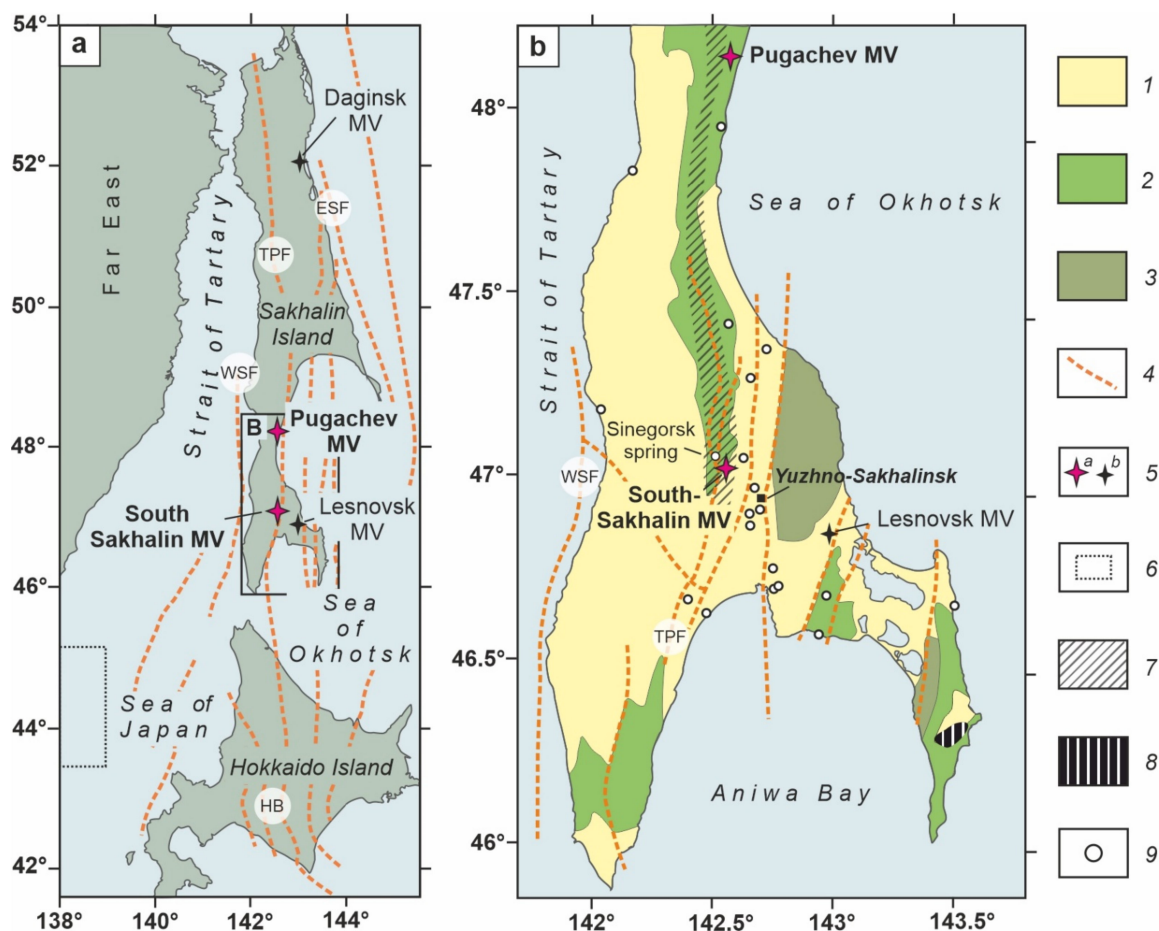


Figure 1. Geological sketch of the Sakhalin mud volcanic province. (a) Location map of mud volcanoes in Sakhalin province. (b) Enlarged box from panel (a): southern Sakhalin Island. Rock formations: 1 = Cenozoic (mostly Paleogene–Neogene) sediments; 2 = Mesozoic (K) rocks; 3 = Paleozoic rocks, after [26]; 4 = faults, after [20], abbreviated as: ESF = East Sakhalin Fault, HB = Hidaku Belt, TPF = Tym–Poronay Fault, WSF = West Sakhalin Fault. 5 = sampled (a) and unsampled (b) mud volcanoes; 6 = aureoles of atmospheric mercury dispersion, after [27]. Mineragenic zone after [28]: 7 = the belt of Sb–Hg mineralization; 8 = Neogenic Ge-rich coal. 9 = hot springs and boreholes, after [20].

Although the active phase of subduction beneath Sakhalin ceased in the mid-Miocene [22], tectonic processes are still ongoing in the crust below Sakhalin and the surrounding offshore areas, judging by high seismicity [20] and high heat flux. The local geothermal gradient in South Sakhalin (46.59–47.33° N; 142.10–143.02° E) is as high as $X_{av.} = 41.14 \pm 5.86$ °C/km (32.10–51.60 °C/km; $n = 25$), according to measurements of 1974 through 1995 in nineteen boreholes within the 30 to 2875 m depth interval [29].

Along with the seismic and geothermal activity, mud volcanism is another manifestation of ongoing tectonic movements in Sakhalin. It evolves under regional-scale compression associated with the Miocene subduction [20]. The ongoing tectonic activity, the high shallow current seismicity, the high geothermal gradient, the systems of large faults, as well as the existence of overpressure zones, and a setting of an ancient accretionary prism formed under W–E compression make the thick sequence of oil- and gas-bearing argillaceous marine sediments in southern Sakhalin favorable for mud volcanism [20,21,30]. MVs of Sakhalin Island feed from the 3–6 km thick Upper Cretaceous Bykov Fm. [30]. The Sakhalin mud volcanic province includes single large MV edifices and differs in this respect from most of other MV provinces with numerous clustering edifices of different sizes [31].

The Sakhalin MV province consists of four known areas, one in the north and three in the south of the island (Figure 1a). The Darginsk geothermal system including small gryphons and hot springs is located on the shore of the Nyi Gulf within the North Sakhalin trough and the East Sakhalin fault zone [32]. The Pugachev and South Sakhalin MV edifices (Figures 2 and 3), as well as numerous seeps of thermal and mineral waters fall within the Tym-Poronay fault zone [20,23,28].

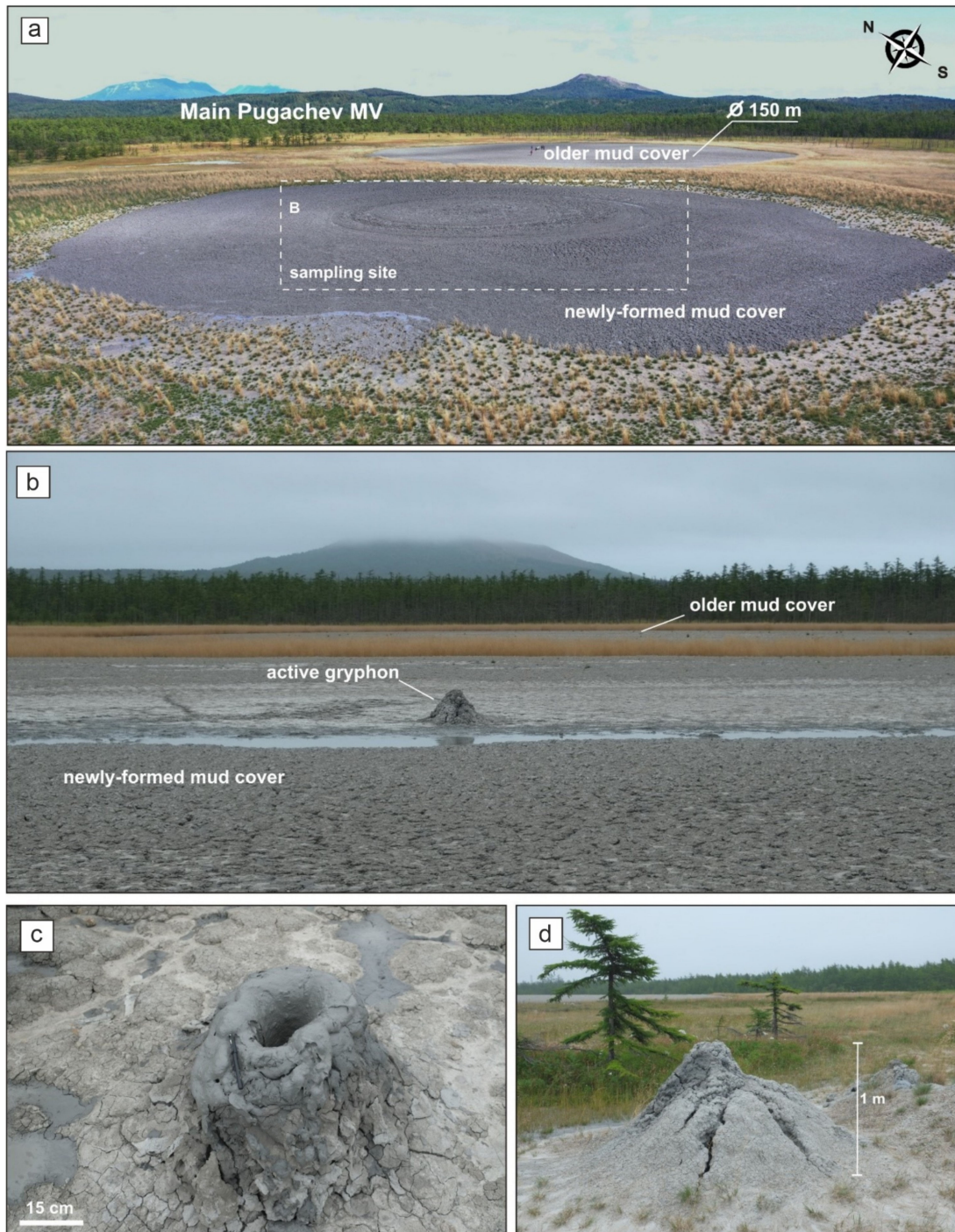


Figure 2. Pugachev mud volcanic field. (a) Main Pugachev mud volcano (MV) (48.2293° N; 142.5629° E), panoramic view. (b) Sampling site: Main Pugachev MV extruding viscous mud (September 2018). (c) Bubbling gryphon upon a newly formed mud cover (September 2018). (d) Active gryphon upon a weathered mud cover on the periphery of MV field (September 2018).

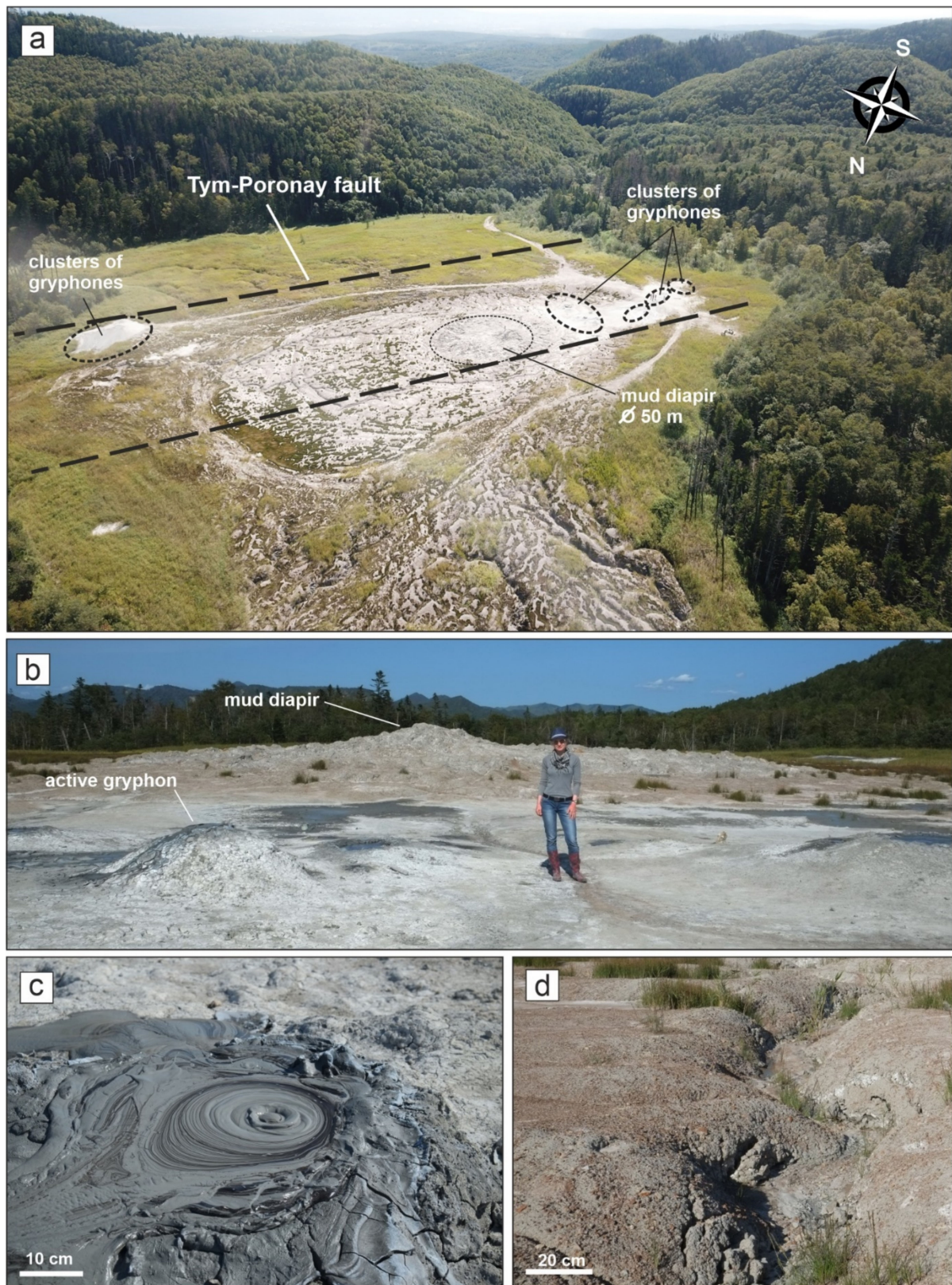


Figure 3. South Sakhalin mud volcano (47.0808° N; 142.5766° E. September 2018). (a) Panoramic view. (b) Mud diapir cut by deep cracks (at the back) and active gryphons and salsas (in the front) in the middle of the flat top of South Sakhalin MV. (c) Bubbling gryphon extruding liquefied mud with coal powder (black rings in grey mud). (d) Weathered mud cover with abundant rock fragments, Ca-Mg-rich siderite, and pyrite.

The group of Pugachev mud volcanoes and South Sakhalin mud volcano are among the largest MVs in the world. They are located in the zone of $M = 7$ seismic risk at intersections of the regional-scale Tym-Poronay reverse fault, with South Sakhalin MV near its emergent plane [33] and small faults (Figure 4). The activity of small Lesnovsky MV was revealed in 1986 [30].

2.2. Local Metallogeny

Sakhalin Island hosts more than thirty known Hg or less often Sb-Hg deposits and occurrences which are localized in the West Sakhalin, Tym-Poronay, and East Sakhalin N—S linear ore zones controlled by the regional-scale West-Sakhalin and Central-Sakhalin fault. The Central metallogenic zone is delineated by the Tym-Poronay fault, which is the main ore-controlling structure of the island and comprises poor Hg, Sb, Pb, Zn, As, Au, and W occurrences (Figure 1b) [23,26,28,34]. The cinnabar and metacinnabar aureoles, as well as As thermal springs, are known all along the Tym-Poronay fault. Most of Hg occurrences are restricted to a 10–15 km wide zone delineated by the West Sakhalin and Tym-Poronay faults in the central and southern parts of the island (Figure 1b) and fall at intersections of the major and pinnate faults [23,26]. Mercury is known from almost all Paleozoic and Mesozoic volcanosedimentary rocks and is hosted especially by mafic and intermediate small intrusions or basaltic andesite volcanics. The largest Hg occurrences lie in brittle rocks under mudrock caps. The Late Cretaceous source rocks of the Sakhalin MVs host small Hg occurrences in deformed tuffaceous sandstones capped by mudstones [23]. Mercury mineralization within the Tym-Poronay zone is localized in the crests of narrow folds or in the hanging walls of thrusts, while the Sb-Hg and Hg sites occur within zones of neotectonic movements that caused thrusting of Cretaceous sediments onto Neogene volcanosedimentary rocks (Figure 4). Zones of hydrothermally altered effusives and deformed volcanoclastics host galena, sphalerite, scheelite and gold, in addition to cinnabar [23]. The fresh mud of Pugachev MV was reported to store up to 1.68 ppm Hg [35], or 11 times the upper crustal values, and to bear metacinnabar, cinnabar, and Hg-bearing sphalerite. The presence of metacinnabar and cinnabar in the ejecta of Pugachev MV was attributed [23] to Quaternary regeneration of older Hg occurrences under the impact of MV fluids.

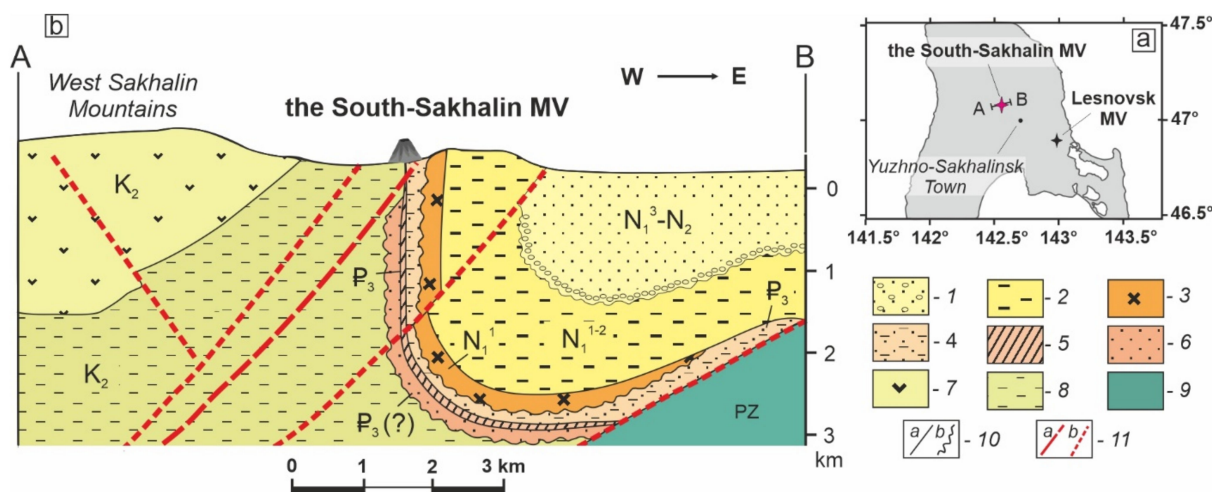


Figure 4. Cross-section of sediments beneath South Sakhalin MV, modified after [36]. (a) Sketch of southern Sakhalin Island. (b) cross-section along profile A–B. 1 = lignite-bearing conglomerate and sandstone (N_1^3 – N_2). 2 = siliceous siltstone and mudstone (N_1^{1-2}). 3 = dacitic andesite (N_1^1). 4 = sandy siltstone and mudstone (P_3). 5 = coal-bearing siltstone and mudstone (P_3). 6 = sandstone and conglomerate (P_3 (?)). 7 = volcaniclastic sediments (K_2). 8 = siltstone and mudstone (K_2). 9 = Paleozoic metamorphic rocks (PZ). 10 = concordant (a) and discordant (b) geological boundaries. 11 = man plane of the Tym-Poronay thrust (a) and other faults (b).

The Sakhalin metallogeny also includes numerous gold occurrences (East Sakhalin mountains and western coast, where the belt of Miocene epithermal Au-Ag mineralization extends from the Japan islands), as well as Neogene Ge-bearing coal (Novikovo deposit) ~150 km far from South Sakhalin MV (Figure 1b) [26,28].

3. Sampling Sites

3.1. Pugachev Mud Volcano

The Pugachev MV field is located in the central part of Sakhalin Island about 45 km south of Makarov Town and 3 km west of the Okhotsk Sea coast, at 48.2293° N; 142.5629° E. It is a cluster of the large Main Pugachev MV dome and two satellite edifices of Small North and Small South MVs (Figures 1 and 2a). The Pugachev MV field is a 10 m high flat-topped gently sloping hill reaching 58 m asl, on a 2.5 km × 2 km base, extending in the NE–SW direction. Main Pugachev MV erupted more than twenty times between 1906 and 2006, with a recurrence of 70 years for large eruptions (2000–8000 m³ of total ejecta) and 1 to 3 years for small eruptions [30,37–39]. Mud volcanism shows no distinct correlation with seismic events, except for the large eruption of 2000, which was triggered by the $M_S = 7.0$ ($I_0 = 8–9$) Uglegorsk earthquake of 4 August 2000 to a high probability [40].

During the intervals between rare high-gas factor explosive eruptions, the volcano behaves as a clay diapir, with continuous extrusion of fresh viscous mud from a conduit at the center of the edifice. The newly-formed mud cover commonly forms circles 50–200 m in diameter (Figure 2a,b), and its geometry changes only after large eruptions, such as the one of 2005 when at least 100,000 m³ of mud was expelled [37,38]. The dome of Pugachev MV fits a geophysically anomalous zone [29]: a local gravity low, ~1.0–1.5 km in diameter, low magnetization typical of brecciation zones, and a relatively high heat flux of 49–52 mW/m²; the mean annual ground temperature in this zone is 8–18 °C higher than outside the MV field. The ~1.0–1.5 km diameter must correspond to the feeding channel of the volcano.

While we were sampling the area in September 2018, Main Pugachev MV demonstrated moderate permanent activity. It had an oval-shaped ~40 m × 50 m zone of fresh wet breccia and two distinct heavily deformed old covers, with water and bubbling gas emerging through numerous cracks. The summit plateau of the mud volcano accommodated around twenty small individual cones (gryphons), all within 1 m in height and in diameter, which released minor amounts of gas and very viscous mud (Figure 2b,c). The belt of gryphons was aligned with the Tym-Poronay reverse fault, and likely has had this orientation since the onset of observations in 1938 [38].

3.2. South Sakhalin Mud Volcano

South Sakhalin MV, the largest edifice of Sakhalin Island, is located about 18 km northwest of Yuzhno-Sakhalinsk Town, in the southern part of the island, at 47.0808° N; 142.5766° E (Figure 1). It has been moderately active for the past one hundred years, with at least 6 large eruptions since 1928: 1959, 1979, between 1994–1996, 2001, and 2020 [36,41,42]. The voluminous mud-volcanic breccia produced by those events (50,000 to 200,000 m³ each), fully covered the older mud fields and changed the edifice topography [36,41]. Shallow seismic surveys beneath the central part of the volcano revealed zones of low *P*-wave velocities at 12–22 m [43] and 5–40 m [44] depths, which may correspond to a small intermediate chamber filled with gas-saturated liquefied mud.

South Sakhalin MV is a 30 m high flat-topped conical hill (300 m asl; 550 × 310 m² base) with small numerous bubbling gryphons and salsas emitting mainly water, liquefied mud, and gas (Figure 3). The number of gryphons and salsas has changed randomly from 40 to 70 since 1928 [36,41]. In 2018, the volcano was marked by a 1.0–1.5 m high mud diapir, ~50 m in diameter, cut with a network of deep cracks, and an SW–NE chain of forty gryphons and salsas grouped into five main clusters (Figure 3b). The chain of gryphons was aligned with the Tym-Poronay reverse fault, like in the case of Pugachev MV (Figure 3a). The rate of gas emanation at this volcano correlates with large earthquakes: it

increased abruptly in some gryphons from the 20 mL/s background to 40–60 mL/s after the Gorny Zavod (2006) and $M_s = 6.2$ Nevelskoy (2007) events [45,46].

4. Methods

4.1. Sampling

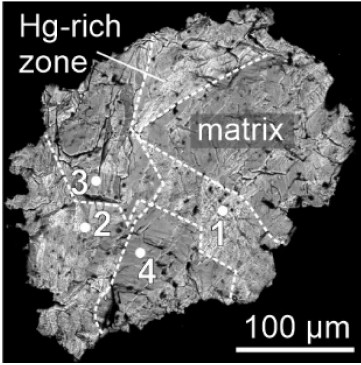
South Sakhalin and Pugachev mud volcanoes were examined and sampled during a field trip in September 2018, when both exhibited weak activity. The sampling sites were located using a Garmin GPS, in a WGC-84 system. We collected 70 samples of currently extruded liquefied fresh and slightly weathered mud masses as well as 17 samples of MV water of current expulsion, As thermal water of Sinegorsk borehole; Makarovka river and a few springs, which drainage the MV areas were also sampled. Rainwaters, including water of typhoon Jebi (tropical typhoon number 21, the strongest storm for the last 25 years in Sea of Japan), were collected as reference samples.

MV waters and currently extruding liquefied mud were sampled simultaneously into plastic vials and bottles. Water was filtered through a 0.45- μm Nucleopore filter a few hours after sampling, in order to avoid initial salt precipitation and colloid coagulation. Major cations and trace elements were analyzed in 15 water aliquots which were stored separately and then acidified with 0.5 mL of 15 N distilled nitric acid; anions were determined in another 50 mL aliquot of unacidified water. The temperature and pH of every sampled water issue were measured in situ with a manual Hanna Instruments PH ORP Combo Meter & Temperature Gauges (HI98121) to a precision of ± 0.1 °C and ± 0.1 pH.

Five large (40 kg) bulk mud samples and six samples of currently extruded viscous, low viscous or partly solidified muddy masses (2 kg) were taken for most detailed mineralogical analyses. First, clay and heavy fractions were extracted from the samples and subjected to several successive procedures of gravity and electromagnetic separation. The fractions included layered silicates (≤ 2 μm) (1), concentrates of sulfides (2), Fe-rich carbonates (3), stable heavy minerals of clastic fraction (4), as well as a light fraction with predominant quartz sand particles, sporadic fossil remnants consisting mainly of CaCO_3 , and sporadic crystals of calcite or aragonite (5). Second, pyrite (framboids and euhedral crystals separately) and sphalerite, as well as other sulfides, were hand-picked under a binocular for EPMA and SEM analyses; additionally, pyrite fractions were hand-picked in the same way for S isotope analyses. Unfortunately, it was impossible to separate sufficient amounts of sphalerite, galena, and realgar for isotope analysis.

Hg-rich sphalerite from Idermeg–Bayan-Khan-Ula polysulfide–fluorite deposit (Mongolia) described in [3] was used as reference material for X-ray diffraction structural refinement. The sample with catalogue number III-8b/1 (from Drs. V.I. Vasil'ev and A.A. Obolensky, 1976) from the Central Siberian Geological Museum of the V.S. Sobolev Institute of Geology and Mineralogy, Novosibirsk, Russia. The sample is a fragment of chalcedony quartz vein which hosts brown grains of sphalerite. Sphalerite from Idermeg-Bayan-Khan-Ula deposit is Fe-poor and Hg-rich: light brownish matrix of the grain contains 9.74–13.35 wt% Hg, and dark-brown areas contain 22.47–29.48 wt% Hg (Table 1).

Table 1. Back-scattered electron (BSE) image and representative compositions of reference Hg-rich sphalerite from Idermeg-Bayan-Khan-Ula polysulfide–fluorite deposit, Mongolia.

Sample Grain BSE-image	III-8b/1					Total
	Point	Zn	Fe	Hg	S	
	EDS data, wt%					
	1	43.81	<0.30	29.48	26.29	99.58
	2	49.47	<0.30	22.47	28.38	100.32
	3	56.40	<0.30	13.35	30.39	100.14
	4	59.10	<0.30	9.74	30.72	99.56
Formula based on S = 1, apfu						
1	0.817	0.000	0.179	1.000		
2	0.855	0.000	0.137	1.000		
3	0.910	0.000	0.070	1.000		
4 *	0.943	0.000	0.051	1.000		
Average matrix composition		(Zn _{0.926} Hg _{0.061})Σ0.987S				
Average high Hg zones composition		(Zn _{0.803} Hg _{0.158})Σ0.961S				

apfu = atoms per formula unit. EDS = energy-dispersive spectra. * The lower-Hg matrix of high-Hg Mongolian sphalerite was used for single-crystal experiment (see Section 5.3.3. X-Ray Diffraction and crystal structure).

4.2. Analytical Procedures

Analyses were mostly carried out at the Analytical Center for Multi-Elemental and Isotope Research (Sobolev Institute of Geology and Mineralogy (IGM, Novosibirsk, Russia)) and at the South Ural Research Center of Mineralogy and Geoecology (SU FRC MG, Miass, Russia). Major elements in bulk-rock samples were analyzed by the ICP-AES technique (inductively coupled plasma atomic emission spectroscopy) on a ThermoJarrell IRIS Advantage atomic emission spectrometer (ThermoJarrell Intertech Corporation, Atkinson, WI, USA) at IGM (Novosibirsk). The preconditioning procedure included fusion of powdered whole-rock samples with lithium borate [47]. Trace elements in bulk samples of mud masses and their heavy fractions were determined by mass spectrometry with inductively coupled plasma (ICP-MS) on an Agilent 7700x spectrometer (Agilent Technologies, Inc., Santa Clara, CA, USA) at the SU FRC MG (Miass, Russia). The method was described in detail by [48].

Bulk Hg contents in the mud masses and corresponding heavy fractions were measured by flameless atomic absorption spectrometry (AAS) on a Lumex RA-915M Hg analyzer (Lumex Ltd., Saint Petersburg, Russia) with an RP-91C pyrolysis attachment. Prior to analyses, the rock samples were powdered in a mortar and homogenized. The technical specifications of the instrument allow special preconditioning of solid samples to be avoided. The national standard of soil (SDPS-3) certified for heavy metals and mercury was used to calibrate the spectrometer and to check the quality of analyses. Relative analytical errors were 20% ($p = 0.95$) for concentrations from 5×10^{-7} to 2.5×10^{-2} wt% [49]. For analytical details, see [50,51].

Major-element concentrations in water samples were measured at the chemical analytical laboratory of the Geological Institute (GIN, Moscow) and at the Analytical Center of the Institute of Microelectronics, Technology and High-Purity Materials (IMT, Chernogolovka, Russia), by ICP-OES (inductively coupled plasma–optical emission spectrometry), ICP-MS, and acid and AgNO₃ titration. The analytical details were summarized previously [52]. Trace element compositions were analyzed at IMT (Chernogolovka) on a Thermo Jarrel Ash ICAP-61 (Exeter, NH, USA) and a Thermo Elemental X-7 ICP-MS (Waltham, MA, USA) analyzers following the procedure from [53]. The precision and accuracy were 10–15 rel% for all analyzed elements.

Mineral phases ($\geq 1\%$) were identified by X-ray diffraction analysis (XRD) in powdered samples. All specimens were analyzed on a Shimadzu XRD-600 diffractometer (Shimadzu Corporation, Kyoto, Japan) ($\text{CuK}\alpha$ radiation with a graphite monochromator, $\lambda = 1.54178 \text{ \AA}$). The scans were recorded from $6\text{--}60^\circ 2\theta$ at $0.05^\circ 2\theta$ increments with 5 s scanning time per step. For analytical details, see [54,55].

Scanning electron microscopy (SEM) was used to identify minerals and to characterize the morphology of sulfides, based on energy-dispersive spectra (EDS), backscattered electron (BSE) images, and X-ray element maps (EDS system). The measurements were performed at IGM (Novosibirsk) on a TESCAN MIRA 3LMU microscope (Tescan Orsay Holding, Brno, Czech Republic) equipped with an Oxford AZtec Energy Xmax-50 microanalyses system (Oxford Instruments Nanoanalysis, Abingdon, UK). For SEM examination, fragments and thin sections of sulfides were sputter coated with ~ 15 to 25-nm carbon films. EDS analyses of minerals were run in a high-vacuum mode at an accelerating voltage of 20 kV, a beam current of 1.5 nA, and a live spectra acquisition time of 20 s. Matrix correction was done using the XPP algorithm (exponential model of Pouchou and Pichoir matrix correction), implemented in the software of the microanalysis system. Metallic Co served for quantitative optimization (normalization to beam current and energy calibration of the spectrometer) [56–58]. The detection limits (3σ value) were 0.15 wt% for Mn, S, Se, Cu, Ag; 0.20 wt% for Fe, Ni, Zn, Cd, Sb; 0.30 wt% for Ga, Ge, As, Hg, Pb; and 0.40 wt% for Tl.

Electron probe microanalyses (EPMA) with wavelength-dispersive spectrometer (WDS). Mineral chemistry of sulfides was analyzed in $>100\text{--}400 \mu\text{m}$ grains on a Jeol JXA 8100 electron microprobe microanalyzer (Jeol, Tokyo, Japan) in C-coated polished thin sections, at an accelerating voltage of 20 keV, a beam current of 20 nA, and a peak counting time of 10 s. The compositions of sphalerite were determined with reference to standards: synthetic ZnS for S $\text{K}\alpha$ and Zn $\text{K}\alpha$, FeS_2 for Fe $\text{K}\alpha$, FeNiCo for Ni $\text{K}\alpha$, GaSb for Ga $\text{L}\alpha$ and Sb $\text{L}\alpha$, metallic Ge for Ge $\text{K}\alpha$, CdS for Cd $\text{L}\alpha$, InAs for In $\text{L}\alpha$ and As $\text{L}\alpha$, ZnSe for Se $\text{L}\alpha$, HgTe for Hg $\text{L}\alpha$, and Bi_2S_3 for Bi $\text{L}\alpha$. The detection limits (3σ value) for the elements were (in wt%): 0.03 for Fe and Ni; 0.04 for Sb; 0.05 for S; 0.09 for Zn; 0.10 for Hg; 0.12 for In; 0.15 for Cd; 0.16 for As; 0.18 for Se; 0.22 for Ga; 0.25 for Bi; and 0.30 for Ge. The matrix correction using the ZAF algorithm (generalized algebraic procedure; assumes a linear relation between concentration and X-ray intensity) [59] was applied to raw data prior to recalculation into elements. Analytical accuracy was within 2 rel% for $[\text{C}] > 5 \text{ wt}\%$ elements, and about 5 rel% for $[\text{C}] < 2 \text{ wt}\%$ elements.

The trace-element chemistry of low- and medium-Hg sphalerite was determined by laser ablation mass spectrometry inductively coupled plasma (LA-ICPMS) at the Department of Geosciences and Geography (University of Helsinki, Helsinki, Finland) using an Agilent 7900s ICPMS coupled to a Coherent GeoLas MV 193 nm Laser. Ablation was performed in pure helium (1.05 l/min) mixed with Ar (0.85 l/min), after ablation. Crystals and grains of sphalerite (samples PG-18-1-1, PG-18-8-1, US-18-3-6, US-18-4-4, and US-18-6-1), as well as crystals and framboidal aggregates of pyrite (samples PG-18-1-1, PG-18-7-1, PG-18-8-1, US-18-1-3, US-18-4-4) extracted from heavy fractions were analyzed in polished sections. The interior texture of every sulfide grain was examined by SEM with a special focus on mineral inclusions and compositional heterogeneities in sphalerite or mineral inclusions in pyrite. The majority of selected grains are large (100–200 μm), chemically homogeneous and generally free from visible inclusions. Analyses were conducted using a spot size of 44 μm at a fluence of 3.5 J/cm² and repetition rate of 10 Hz for pyrite and spot size of 44 μm at a fluence of 3.5 J/cm² and repetition rate of 5 Hz for sphalerite. A 30 s background with an additional 30 s for sample washout was applied before each analysis. The primary calibration of trace elements was done using USGS MASS-1, using GeoReM preferred values. A secondary standard correction was done using USGS GSD-1G, again with GeoReM preferred values. The instrument was tuned to ThO/Th ratios of $<0.3\%$ and U/Th ratios of $\sim 100\%$, doubly charged cations were tuned to $<0.4\%$ using SRM NIST610, and SRM NIST612 as unknown. The measured isotopes were: ²⁴Mg, ²⁷Al, ²⁸Si, ³³S, ³⁴S,

³⁹K, ⁴³Ca, ⁴⁴Ca, ⁵¹V, ⁵²Cr, ⁵⁵Mn, ⁵⁶Fe, ⁵⁷Fe, ⁵⁹Co, ⁶⁰Ni, ⁶⁵Cu, ⁶⁶Zn, ⁷⁰Ge, ⁷¹Ga, ⁷⁵As, ⁸²Se, ⁹⁵Mo, ¹⁰⁷Ag, ¹¹¹Cd, ¹¹⁵In, ¹²¹Sb, ¹²⁵Te, ¹⁹⁷Au, ²⁰²Hg, ²⁰⁵Tl, ²⁰⁸Pb, ²⁰⁹Bi and ²³⁸U.

Data reduction was undertaken using the program SILLS (v1.0.4; mineralsystems.ethz.ch/software/sills.html, 4 April 2008). Zinc (⁶⁶Zn) and iron (⁵⁷Fe) values, which were previously determined by EDS and WDS, were used as internal standards for data reduction of LA-ICPMS analyses of sphalerite and pyrite, respectively.

Crystals with different Zn/Hg ration were first inspected with optical and scanning electron microscopes, after which crystals (or their fragments) were selected for X-ray single-crystal diffraction studies. Selected (Zn,Hg)S crystals was performed on a Stoe IPDS-2T diffractometer (image-plate detector, graphite-monochromatized MoK α radiation) at the Novosibirsk State University using ω -scans technique with scan width of 1° per frame. Data reduction was performed with the CrysAlis Pro 171.37.35 program package. Multi-scan technique was used for a semi-empirical absorption correction. Crystal structures were determined with the SHELXL-2018/3 package [60]. The Zn and Hg occupancies of M-positions were refined assuming their full populations. Cations present in minor amounts (Fe and Cd) were not taken into account in the refinement.

Raman spectra of high-quality sphalerite crystals (grain 9-6, sample US-18-6-1) were recorded on a Horiba Jobin Yvon LabRAM HR800 spectrometer (Horiba Jobin Yvon S.A.S., Lonjumeau, France). The spectra were excited with 532-nm green line of a Thorlabs 50-mW power neodymium Nd:YAG laser working at double-harmonic frequency. The radiated laser power was attenuated with optical filters, and the beam power incident onto the sample was about ~0.1 mW. The scattered light was recorded by a 1024-channel Peltier-cooled CCD detector (Andor, Oxford Instruments, international company based in Belfast, Northern Ireland) in a region of 50 to 3000 cm⁻¹ at a resolution of 2 cm⁻¹. The excitation was with Olympus objectives at magnifications of $\times 50$ (WD = 0.4 mm) and $\times 100$ (WD = 0.2 mm). The Raman spectra of the selected sphalerite (grain 9–6) were deconvolved into Voigt amplitude functions using the Model S506 Interactive PeakFit software (2002 Spectroscopy Software, Canberra Industries, Meriden, CT, USA).

Sulphur isotopic compositions of pyrite (quoted as ³⁴S per mille (‰) relative to the Canyon Diablo Troilite (CDT) standard) were analyzed on a Delta+ Advantage mass-spectrometer (Thermo Finnigan, Waltham, MA, USA) in IGM (Novosibirsk) using NBS-123 and IAEA-S-1 standards, with ³⁴S values reproduced to no worse than 0.15‰ CDT.

5. Results

5.1. General Characteristic of Eruption Products of Pugachev and South Sakhalin MVs

The eruption products of the Sakhalin MVs include the gas, water, and solid components. South Sakhalin and Pugachev MVs differ in the relative percentages of emitted gases: more carbon dioxide in the former (up to 95 vol% CO₂ against 5 to 35% CH₄) and more methane in the latter (50% to 85% CH₄ against 40% CO₂), with minor amounts of oxygen and nitrogen [61,62].

The MV waters of South Sakhalin volcano have HCO₃-Cl/Na-Mg chemistry (dominated by HCO₃) and low salinity (TDS, total dissolved solids), which is common to waters of this kind in the Pacific active belt [21,42,62–64]. During the field observations of 2018, active bubbling salsas (gas flow 7.1–20.8 mL/s) emitted MV water with Eh_{av.} = –66.2 and pH from 7.5 to 8.3 (pH_{av.} = 7.6). The TDS concentration was comparable with that in As mineral water of Sinegorsk borehole: 12.5–14.7 g/L against ~11 g/L of NaCl equivalent [21]. In addition to boron and lithium enrichment (44–55-times seawater value B, K_{EF} = (C)_{MV}/(C)_{SW}) and K_{Li} = 27–38), which is typical of MV fluids [52,55,65,66], the South Sakhalin MV waters are rich in several other elements (quoted as average over n = 29): 6600 µg/L Ba (K_{Ba} = 190–690), 40 µg/L As (K_{As} = 12–81), 12 µg/L Pb (K_{Pb} = 4–8), 1.8 µg/L Sb (K_{Sb} = 4–16), and 32–83 µg/L Zn (K_{Zn} up to 200) in each third MV water sample (Figure 5). The contents of Ga (<2 µg/L), Ge (<2 µg/L), Cu (<20 µg/L), and Se (<19 µg/L) are below the detection limits. According to our data (sampling 2018) and published evidence for 2001–2005 [67], the surface waters of the southern Sakhalin area

have high enrichment in Zn ($K_{Zn} = 114\text{--}273$) and Cu ($K_{Cu} = 8.5\text{--}12$), and those of the Sinegorsk borehole bear $82 \mu\text{g/L}$ Zn ($K_{Zn} = 275$).

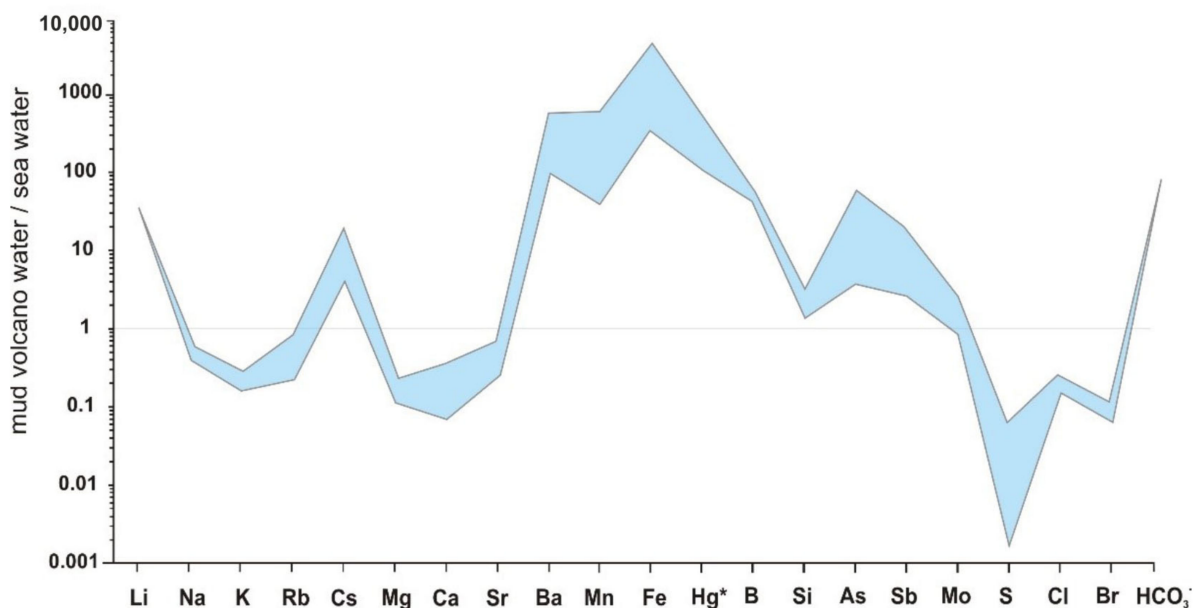


Figure 5. Multi-element seawater-normalized [68] patterns of South Sakhalin MV waters. * Mercury content in seawater according to [69].

The $\text{HCO}_3\text{--Cl/Na}$ Pugachev MV waters have low average TDS ($3.0\text{--}8.0 \text{ g/L}$, NaCl equivalent) due to dilution with rainwater and relatively high Cl/HCO_3 ratios [21,42,63]. The least diluted samples contain $141\text{--}206 \mu\text{g/L}$ As, $3.35\text{--}8.16 \mu\text{g/L}$ Sb, $71.1\text{--}95.7 \mu\text{g/L}$ Zn, $0.9\text{--}12.0 \mu\text{g/L}$ Pb, and $2.3\text{--}4.2 \mu\text{g/L}$ Ge, while the contents of Ga ($<2 \text{ mkg/L}$), Cu ($<20 \text{ mkg/L}$), and Se ($<6 \text{ mkg/L}$) are below the respective detection limits.

The samples of 2018 contain mercury: $0.14\text{--}0.50 \mu\text{g/L}$ Hg ($X_{av.} = 0.33$; $n = 4$) in the Pugachev MV water and $0.10\text{--}0.64 \mu\text{g/L}$ ($X_{av.} = 0.41$; $n = 9$) in those of South Sakhalin MV. Meanwhile, the Hg contents in the local surface waters are quite moderate: e.g., $0.22 \mu\text{g/L}$ Hg in the Makarovka River (near Pugachev MV); $0.41 \mu\text{g/L}$ and $0.37 \mu\text{g/L}$ Hg in a creek and a spring, respectively, that drain South Sakhalin MV. The Hg contents were higher in As mineral water from Sinegorsk borehole (0.64 to $0.74 \mu\text{g/L}$) and in the rainwater of Jebi typhoon (05.09.2018) that arrived from the Japan islands (up to $0.81 \mu\text{g/L}$), but as low as $0.06 \mu\text{g/L}$ in local precipitation (rainfall of 09.10.2018 in Yuzhno-Sakhainsk).

The mud erupted by both sampled volcanoes mainly consists of silt and clay (a total of $\sim 30 \text{ wt}\%$ illite plus illite-smectite and $2\text{--}5 \text{ wt}\%$ kaolinite), with quite high percentages of sand and sedimentary (sandstone with carbonate cement, glauconite- and coal-bearing sandstone, silicified mudstone, etc.) or less often volcanosedimentary fine debris. All analyzed samples bear Fe-Ca-Mg carbonates (Ca-Mg-rich siderite or oligonite, up to $2\text{--}5 \text{ wt}\%$) and much smaller percentages of sulfides (mainly pyrite). Fresh mud may include up to $60 \text{ wt}\%$ of clastic material ($29\text{--}37 \text{ wt}\%$ quartz, $18\text{--}24 \text{ wt}\%$ plagioclase, and $5\text{--}11 \text{ wt}\%$ K feldspar). The Pugachev MV mud masses contain montmorillonite and calcite-kaolinite in small veins. Old mud covers in Sakhalin have heavy mineral fractions and debris accumulated on the top, while the fine fractions become washed out in the wet climate. This is, for instance, the case of sample US-18-6-1 with 22% Ca-Mg-rich siderite (Figure 3d).

5.2. Heavy Fractions in Ejecta of Sakhalin MVs: Mineralogy and Geochemistry

Mineral assemblages identified in heavy-fraction samples of both Sakhalin MVs share general similarity. They consist of $94\text{--}97\%$ Fe-Mg-Ca siderite-ankerite carbonates, $\leq 6\%$ pyrite, and $\leq 1 \text{ wt}\%$ calcite and aragonite. All such samples contain similar as-

semblages of ultrastable minerals, with predominant double-headed zircon crystals and colorless F-Cl-bearing apatite, and with few grains of rutile, ilmenite, garnet, clinopyroxene and amphibole. The South Sakhalin MV mud masses and pulp enclose numerous fragments and fine debris of coaliferous rocks (Figure 3c), and often contain spherulitic dawsonite ($\text{NaAl}(\text{CO}_3)(\text{OH})_2$) and sporadic bastnäsite ($\text{LREE}(\text{CO}_3)\text{F}$) grains. Sulfate assemblages consisting of baryte, gypsum, and anglesite (PbSO_4), as well as rhabdophane ($\text{LREE}(\text{PO}_4)\cdot n\text{H}_2\text{O}$) and florencite ($\text{LREEAl}_3(\text{PO}_4)_2(\text{OH})_6$) authigenic phosphates, are identical at both sites.

The heavy-fraction mud samples from both Sakhalin MVs bear diverse Fe, Zn, Pb, As, Hg, Sb, Ag, and Cu sulfides (14 mineral species totally) (Table 2) and show similar patterns of chalcophile elements.

Table 2. Sulfide assemblages extracted from the heavy fractions and mud masses of Pugachev and South Sakhalin MVs, Sakhalin Island.

Mineral	Formula	Pugachev MV				South Sakhalin MV			
		PG-18-1-1	PG-18-8-1	PG-18-7-1	US-18-1-3	US-18-6-1	US-18-5-3	US-18-4-4	
Pyrite (biomorphic and framboidal aggregates)	FeS_2 cub	●●	●●	●	●●	●●	●	●●	
Pyrite (crystals)	FeS_2 cub	●●	●	●●	●●	●●	●	●	
Sphalerite low-Hg (Hg < 0.3 wt%)	ZnS cub	●	■	◆		*		■	
Sphalerite medium-Hg (0.3 < Hg ≤ 3 wt%)	$(\text{Zn,Hg})\text{S}$ cub	■	◆	◆	◆	■	◆	◆	
Sphalerite high-Hg (3 < Hg ≤ 27 wt%)	$(\text{Zn,Hg})\text{S}$ cub	◆	◆			◆			
Galena	PbS	◆	◆		◆	■	◆	◆	
Marcasite	FeS_2 rhom		◆	◆	■	■			
Realgar	As_4S_4	◆	◆	◆			◆	◆	
Boulangerite	$\text{Pb}_5\text{Sb}_4\text{S}_{11}$	◆	◆	◆	◆				
Acanthite	$\alpha\text{-Ag}_2\text{S}$	*	*	*	*	*			
Chalcopyrite	CuFeS_2	*					■		
Bournonite	CuPbSbS_3	◆	◆	◆					
Metacinnabar	HgS cub	◆	◆						
Robinsonite	$\text{Pb}_4\text{Sb}_6\text{S}_{13}$	◆							
Cinnabar	HgS trig	*		*					
Moeloite	$\text{Pb}_6\text{Sb}_6\text{S}_{17}$	*							
Stibnite	Sb_2S_3	*							

Symbols show relative mineral percentages ●● = >20 vol% (main); ● = 10–20 vol% (abundant); ■ = 1–10 vol% (rare); ◆ = <1 vol% (accessory); * = sporadic; no symbol = absent.

The contents of Co, Ni, Mo, Cd, and Tl are lower than the respective upper continental crust (UCC) values in bulk mud samples but correspond to the UCC reference in the heavy fractions (Table 3). Other chalcophile elements (Zn, Hg, As, Ge, Se, and Cu) occur in moderate amounts in bulk mud masses but are high in the heavy fractions. In the heavy fraction mud samples from Pugachev MV, the excess relative to the UCC values reaches two orders of magnitude for Hg and Se, around ten times for Zn, Sb, As and Ge, and ~1.5 times for Bi, Pb and Cu.

Table 3. Average trace-element compositions (ICP MS data, ppm) of mud and heavy fractions from South Sakhalin and Pugachev MVs, Sakhalin Island.

	UCC, ppm	South Sakhalin MV		Pugachev MV	
		Mud Masses n = 21	Heavy Fractions n = 8	Mud Masses n = 12	Heavy Fractions n = 7
Zn	67.0	73.2	172	72.5	179
Hg	0.05	0.07	0.09	0.53	1.24
As	4.80	9.20	14.9	11.4	31.5
Ge	0.40	0.80	1.05	0.77	2.03
Se	0.09	<1.80	2.88	<1.80	3.05
Cu	28.0	39.4	44.9	25.9	42.1
Sb	0.40	0.50	0.47	0.90	2.03
Bi	0.16	0.25	0.27	0.21	0.20
Pb	17.0	18.4	19.2	13.8	26.2
Co	17.3	10.8	14.4	9.60	19.7
Ni	47.0	22.1	30.1	20.8	43.6
Mo	1.10	0.28	0.32	0.29	0.43
Cd	0.09	0.12	0.09	0.08	0.11
Tl	0.90	0.44	0.43	0.40	0.40

Upper Continental Crust (UCC) composition of after [70]. Values markedly above UCC values are in bold.

5.2.1. FeS₂ Modifications

The heavy mineral fractions in mud masses from both MVs contain diverse sulfides with predominant pyrite, whereas marcasite is found occasionally as intergrown prismatic crystals (Figure 6). Pyrite occurs as botryoidal aggregates and pseudomorphs after fossil remnants composed of framboids (Figure 6a,c,d), as well as coarse euhedral crystals (Figure 6b,f,g,h). Pyrite is often intergrown with clastic quartz, plagioclase, and Fe-rich authigenic carbonates, less often with baryte, and rarely with sulfosalts, galena, and acanthite. Pyrite was found once intergrown with ZnS but never with HgS. The interstitials between pyrite crystals and framboids are often filled with clayey matter. Framboids show a complete recrystallization series ending with compact aggregates of isometric euhedral crystals. Some framboids demonstrate sunflower structures with a framboidal core and radiating outer crystals (Figure 6e). Primary framboids are mostly spherical (up to 50 µm) and consist of ordered cubic, cubic-octahedral, or octahedral grains (Figure 6d). Pyrite occurs as up to 200 µm octahedral, cubic-octahedral or cubic crystals or their intergrowths (Figure 6f,g). Some crystals have stepped growth layers and are dusted with microcrystals of later generations (Figure 6h).

Trace-element contents in pyrite framboids and crystals, determined by LA-ICPMS, are the highest in framboidal pyrite: 744 ppm Mn, 394 ppm Ni, 361 ppm Cu, 108 ppm As, 96.6 ppm Pb, 85.6 ppm Co, 55.1 ppm Zn, and 31.0 ppm Tl (average over n = 8). Pyrite framboids also carry minor amounts of Hg (2.06–27.0 ppm), Sb (2.05–13.0 ppm), Mo (2.49–12.8 ppm), Ag (1.20–5.57 ppm), Ge (up to 1.78 ppm), Bi (up to 1.41 ppm), V (0.44–0.86 ppm), Au (up to 0.19 ppm), and Ga (up to 0.15 ppm); Se and Cd are below the detection limits.

Pyrite crystals have relatively low trace-element concentrations: 47.29 ppm As, 22.20 ppm Ni, 20.73 ppm Mn, 13.13 ppm Zn, and 12.98 ppm Tl (average over n = 13). Other trace elements are low or very low, such Ge (0.18–14.16 ppm), Co (0.11–8.07 ppm), Mo (≤8.14 ppm), Cu and Sb (≤5.35 ppm), Pb (0.29–3.65 ppm), Hg (≤1.93 ppm), V (≤0.48 ppm), Ga (≤0.13), and Ag (≤0.04). The concentrations of Se, Cd, Te, and Au are below the detection limits. Some framboidal pyrites show irregular spikes of 4181 ppm As, 1017 ppm Pb, 943 ppm Cu, 2139 ppm Ni, 1046 ppm Co, 301 Tl, 70 ppm Bi, 47 ppm Ag, and 31 ppm Se, or around ten times the values common to framboids. The abnormal trace-element contents may be due to sub-micrometer inclusions of Pb-Sb-(Cu) sulfosalts, galena, acanthite, and realgar.

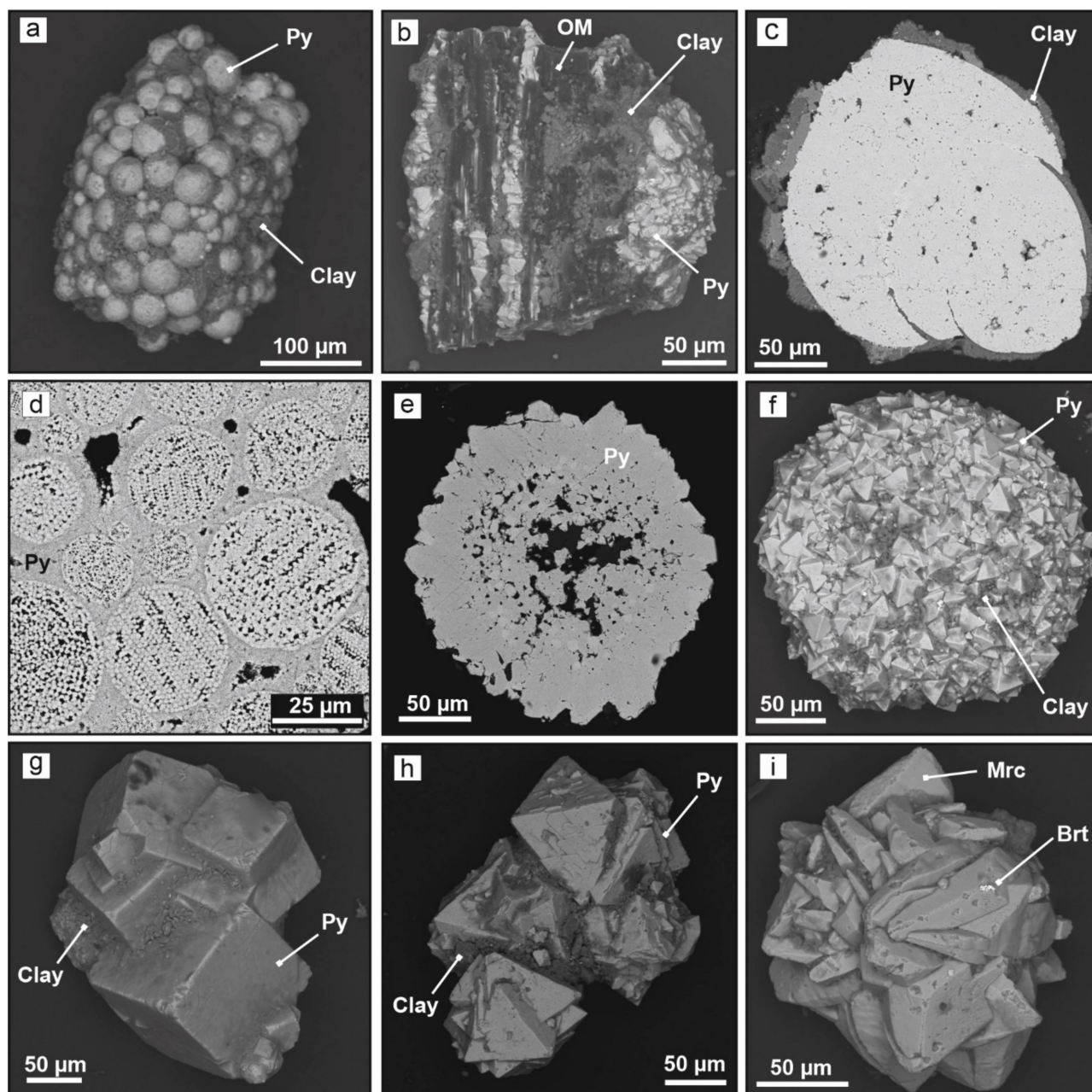


Figure 6. Back-scattered electron (BSE) images showing the morphology of pyrite (a–h) and marcasite (i) from mud masses extruded by South Sakhalin (a) and Pugachev (b–i) MVs. (a) Botryoidal aggregate of primary spherical pyrite framboids. (b) Pyrite layers in coal-bearing shale (c) Pseudomorphs after fossil remnant. (d) Botryoidal aggregate of spherical pyrite framboids buried in pyrite matrix. Most framboids are ordered and filled. (e) Sunflower structures with framboidal core rimmed by radiating outer crystals. (f) Pseudomorph after fossil remnant composed of octahedral crystals that formed during the final stage of the framboids recrystallization. (g) Intergrowth of large cubic pyrite crystals coexisting with clay. (h) Octahedral pyrite crystals and their aggregates. Some crystals are sputtered with microcrystals of later generations. (i) Tabular and prismatic crystals of marcasite coexisting with baryte. Brt = baryte; Mrc = marcasite; OM = organic matter; Py = pyrite.

Both framboids and crystals of pyrite show ^{34}S depletion relative to seawater sulfates (Figure 7). The $\delta^{34}\text{S}$ values are lower in crystals than in framboids: +14.0‰ to +14.8‰ CDT for South Sakhalin (US-18-6-1) and +14.2‰ to +15.8‰ for Pugachev (PG-18-8-1) mud samples against +18.5‰ to +19.3‰ (US-18-6-1) and +19.6‰ (US-18-1-3) for South Sakhalin MV and +18.0‰ for the same Pugachev sample. The $\delta^{34}\text{S}$ values of large pyrite

crystals from Upper Cretaceous sandstone clasts erupted by South Sakhalin MV (seven measurements) fall within the +12.9‰ to +14.2‰ interval, i.e., are close to $\delta^{34}\text{S}$ in pyrite crystals from the mud samples.

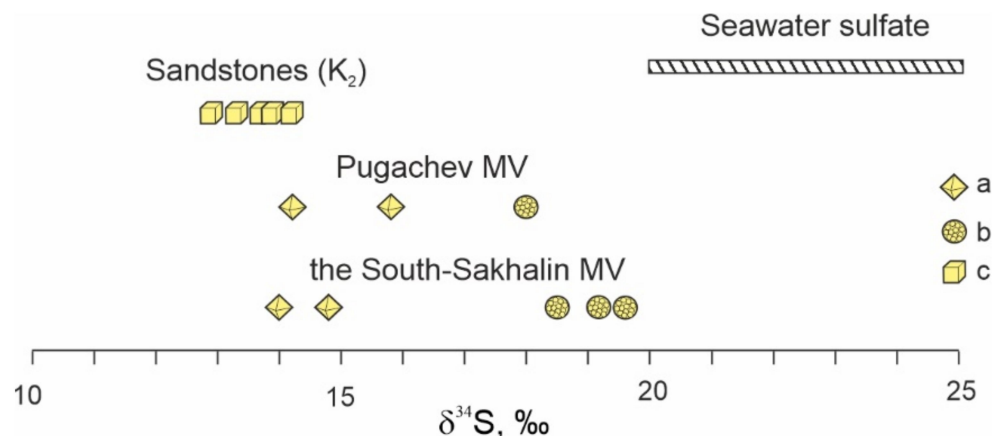


Figure 7. Sulfur isotope composition of pyrite crystals (a) and framboids (b) extracted from Sakhalin MVs and pyrite crystals from Upper Cretaceous sandstone (c). Sulfur isotope composition of seawater sulfate after [71].

Marcasite occurs in minor amounts as intergrown prismatic crystals and commonly forms radiating aggregates (Figure 6i). The surface of marcasite crystals is sometimes encrusted with fine baryte grains. Note, however, that the samples we analyzed lack typical hydrothermal textures of pyrite-marcasite intergrowths or marcasite rims over pyrite. Manganese (≤ 1.2 wt%) is the only reliably determined impurity in marcasite.

5.2.2. Pb, Sb, As, Hg, Cu, and Ag Hosts

In addition to pyrite, all heavy fractions from the Sakhalin MV ejecta contain sphalerite (see Section 4.2), while sulfide concentrates from both MVs bear galena, realgar, and acanthite (as microinclusions in other sulfide hosts). Boulangerite was found in a half of samples, few micrometer grains of chalcopyrite in two samples, and other Pb-Sb-(Cu) sulfosalts, as well as Hg and Sb sulfides, were found at Pugachev MV only (Table 2 and Figure 8).

Galena occurs ubiquitously in heavy mineral fractions as small cleavage fragments, less often as perfect cubic or octahedral crystals (≤ 200 μm) with sharp edges, or still more rarely as rounded anhedral grains locally replaced by anglesite (PbSO_4) (Figure 8g,h). The galena grains in heavy fractions are monomineral or are occasionally intergrown with Pb-Sb sulfosalts or with baryte; sometimes, they enclose kaolinite or very rarely fine chalcedony-like SiO_2 . SEM-EDS analyses of galena from the Pugachev site reveal ubiquitous Se (0.32–2.10 wt%; $X_{\text{av.}} = 1.14$ wt%; $n = 10$) but rare Cu (≤ 0.67 wt%), Sb (≤ 0.94 wt%), Ni (≤ 1.96 wt%), and Bi (≤ 3.0 wt%). The enrichment of galena grains in Se ($X_{\text{av.}} = 19,567$ ppm; $n = 4$) and Sb ($X_{\text{av.}} = 1825$ ppm) is confirmed by LA-ICPMS, which also reveals moderate but stable contents of Ag ($X_{\text{av.}} = 277$ ppm) and low variable As ($X_{\text{av.}} = 120$ ppm), Hg ($X_{\text{av.}} = 110$ ppm), and Bi ($X_{\text{av.}} = 26.4$ ppm). The difference between Sb and Bi contents determined by SEM-EDS and LA-ICPMS may be due to the presence of submicron Pb-Sb-(Bi) sulfosalts inclusions.

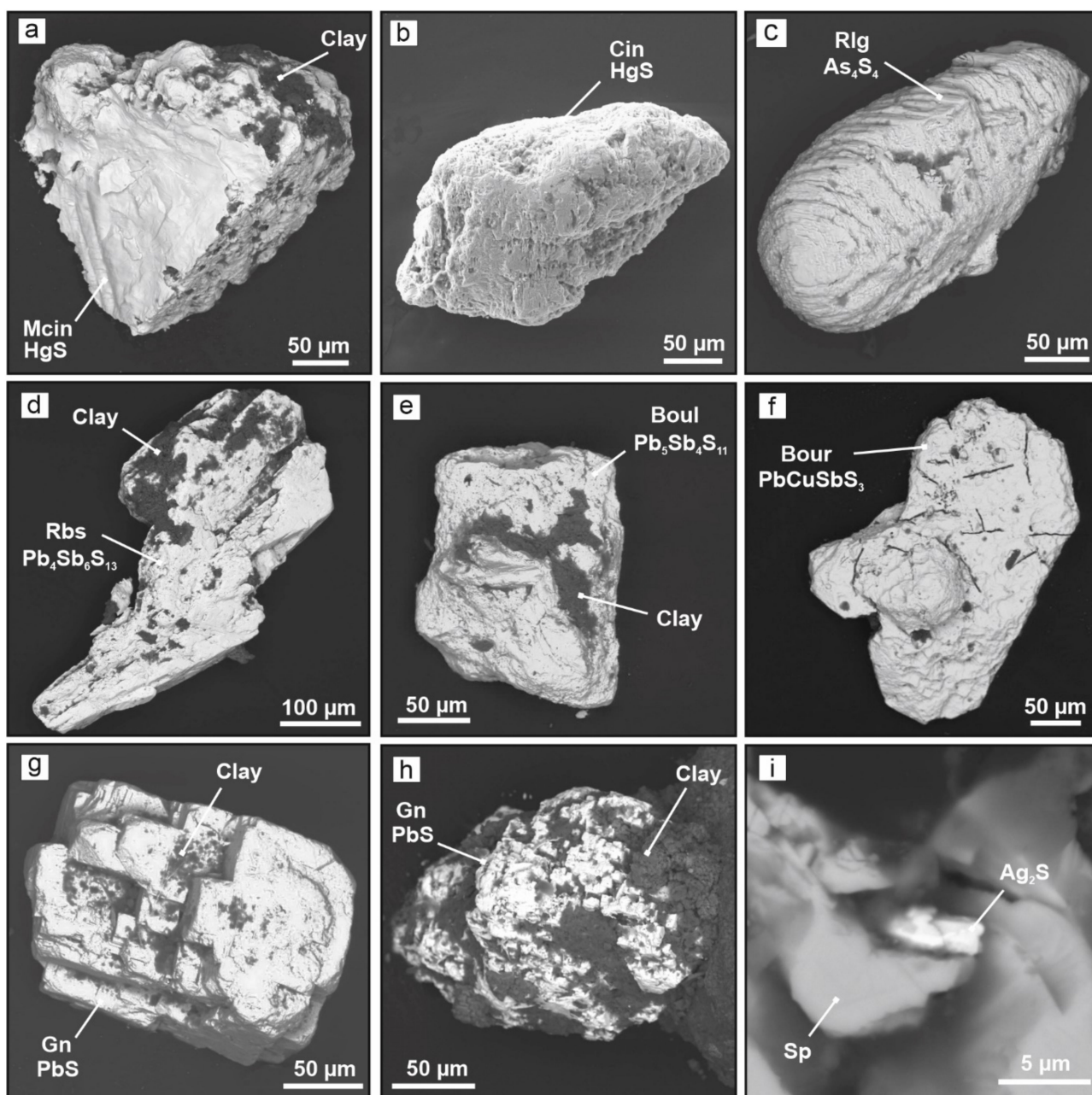


Figure 8. Morphology of host sulfides for Hg, As, Pb, Sb, Cu, and Ag from mud masses extruded by Pugachev (a–g,i) and South Sakhalin (h) MVs. (a) Metacinnabar grain; surface contaminated with clay. (b) Rounded fragment of rhombohedral cinnabar crystal. (c) Rounded elongated grain of realgar. Angular grains of Pb, Sb, Cu sulfosalts contaminated with clay: (d) = robinsonite. (e) = boulangerite, (f) = bournonite. (g,h) Cubic galena crystals with rough growth steps. (i) Particles of silver sulfide (α -Ag₂S?) on the surface of sphalerite crystal. (a,c–i) back-scattered electron (BSE) images, (b) secondary electron (SE) image. Boul = boulangerite; Bour = bournonite; Cin = cinnabar; Gn = galena; Mcin = metacinnabar; Rbs = robinsonite; Rlg = realgar; Sp = sphalerite.

Pb-Sb-(Cu) sulfosalts are often found in heavy fractions, though in moderate amounts: boulangerite (Pb₅Sb₄S₁₁), robinsonite (Pb₄Sb₆S₁₃ with up to 1.5 wt% Bi), and bournonite (PbCuSbS₃) in the Pugachev samples and only scarce boulangerite micrograins in those of South Sakhalin MV. All sulfosalts occur as cleaved clasts or less often as complex intergrowths (Figure 8d–f). Boulangerite sporadically hosts tiny pyrite inclusions or forms aggregates with galena and another Pb-Sb sulfosalts (moeloite (?), Pb₆Sb₆S₁₇) (Table 2). The LA-ICPMS analysis of two quite large boulangerite fragments shows similar impurity

contents of 5742–5937 ppm Se, 784–934 ppm As, 706–842 ppm Bi, 56–59 ppm Te, 44–51 ppm Hg, and ~7 ppm Tl.

Spindle-shaped realgar grains ($\leq 400 \mu\text{m}$), with stepped surfaces, are few but occur in most of the heavy fraction samples (Figure 8c). Some grains have minor amounts of orange-yellow orpiment on the surfaces. According to SEM analyses, its composition corresponds to As_4S_4 stoichiometry with Sb as the only ubiquitous impurity (0.3–0.4 wt%). Only few ($< 10 \mu\text{m}$) ingrown stibnite (Sb_2S_3) patches were found in the realgar host. The contents of Sb in realgar determined by LA-ICPMS vary from 2942 to 9711 ppm ($X_{\text{av.}} = 5432 \text{ ppm}$; $n = 9$); the variations may be due to the presence of enclosed stibnite (Sb_2S_3) or some other Sb-bearing phase, namely getchellite (AsSbS_3). The mineral also contains minor amounts of Hg ($X_{\text{av.}} = 8.71 \text{ ppm}$) and Bi ($X_{\text{av.}} = 6.22 \text{ ppm}$).

Hg sulfides are restricted to few grains in the heavy fractions from Pugachev MV. Most of them are single-phase angular or subangular $\leq 300 \mu\text{m}$ fragments of metacinnabar (Figure 8a). Some grains have rough surfaces with inclusions of Fe-Ca-Mg carbonates or clay entrapped during their growth, or occasionally with ingrown Pb-Sb sulfosalt (boulangerite?). Metacinnabar contains either Zn (1.14–3.29 wt%; $X_{\text{av.}} = 2.3 \text{ wt\%}$; $n = 10$) or Se (1.18–3.40 wt%; $X_{\text{av.}} = 2.3 \text{ wt\%}$; $n = 6$) impurities and comparable amounts of Fe and Ni (~0.3 wt% and 0.4 wt%, respectively). Cinnabar is very rare and has a HgS composition (Figure 8b,f).

Very scarce chalcopyrite occurs as inclusions in Pb-Sb sulfosalt-galena aggregates. Other sulfides often enclose tiny ($< 5 \mu\text{m}$) grains of Ag sulfide (most probably acanthite $\alpha\text{-Ag}_2\text{S}$; $\text{Ag} \approx 86 \text{ wt\%}$; $\text{S} \approx 13 \text{ wt\%}$) (Figure 8i).

5.3. Sphalerite

5.3.1. Morphology

Sphalerite is a common sulfide mineral in all heavy fraction samples from both Sakhalin MVs, being mainly found in the $< 0.5 \text{ mm}$ fraction and especially abundant in fine fractions of 0.2–0.06 mm. We analyzed ~200 grains and determined mineral chemistry and zonation in eighty polished grains. The mineral is highly lustrous, translucent to transparent, and varies in color from light yellow or light brownish to deep honey, reddish and cinnamon-brown; green crystals are very rare. The most frequently found sphalerites are well-defined honey-yellow and reddish tetrahedrons {111} with sharp edges and corners, pseudo-octahedral crystals, and cleavage clasts, while simple twins with (111) axis are rare, and trigon-tritetrahedron crystals are sporadic (Figures 9 and 10).

Sometimes sphalerite occurs as multi-headed regenerated crystals, complex intergrowths (Figure 10c,d), and anhedral to subhedral grains, very rarely as skeletal crystals (two findings). Complex lamella twins sometimes appear on the etched surface of Hg-enriched grains (Figure 10e).

Sphalerites containing $> 2 \text{ wt\%}$ Hg often show vuggy microstructure and regular (Figure 10b) or irregular (Figure 10f) etch features. The analyzed sphalerites bear numerous inclusions of Fe-Ca-Mg carbonates and/or clayey matter encapsulated during the crystal growth. The entrapped clay particles in some of such crystals obstructed normal layer growth, which eventually led to splitting and multi-headed growth (Figure 10d). Inclusions of opaque minerals in sphalerites are extremely rare: purposeful SEM inspection has revealed only sporadic microinclusions of galena (Figure 11a) and acanthite (Figure 8i), and a single Pb-Sb sulfosalt inclusion.

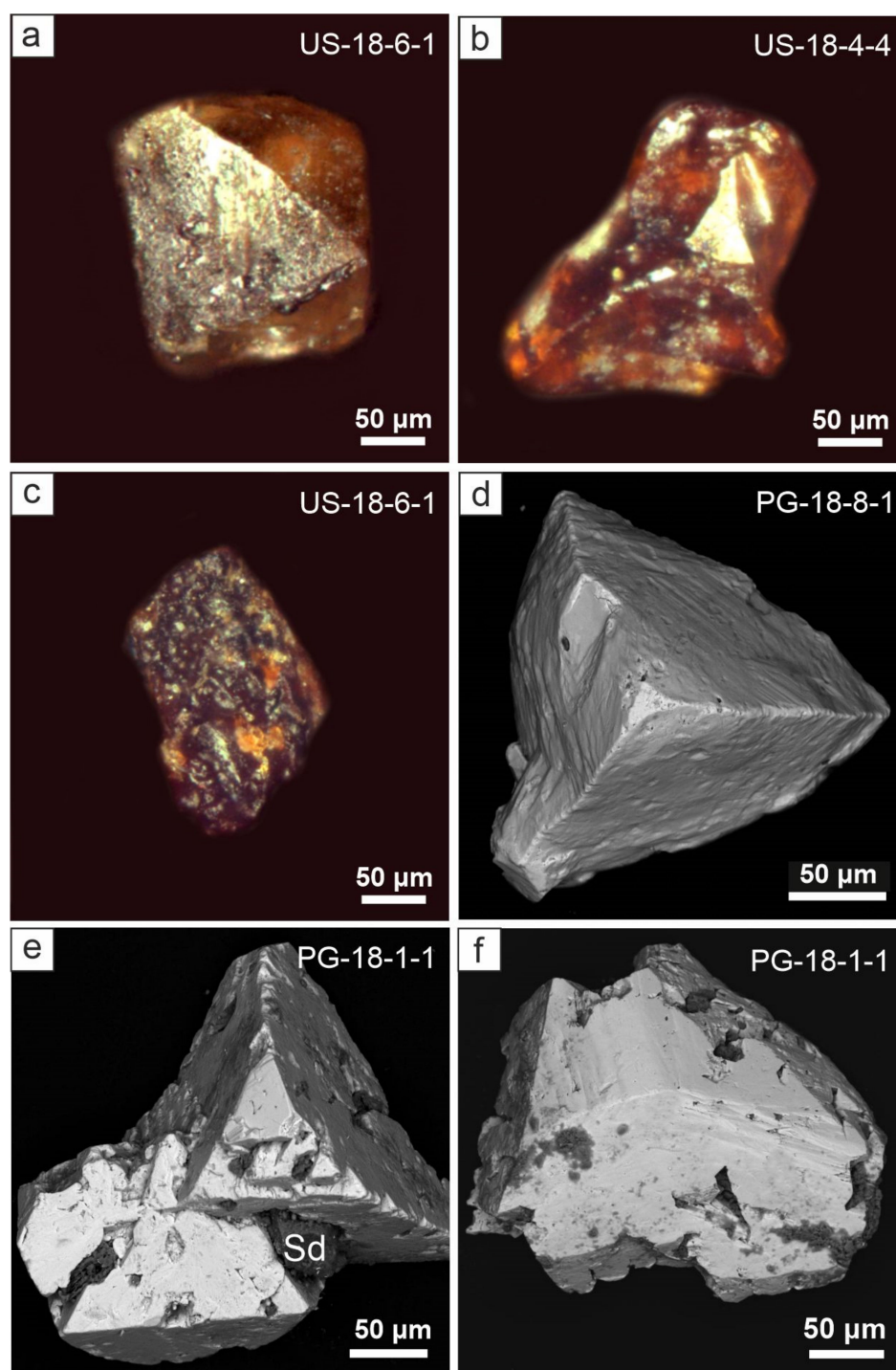


Figure 9. Appearance and morphology of low-Hg (<0.3 wt%) sphalerites from mud masses of South Sakhalin (a–c) and Pugachev (d–f) MVs. Optical images: (a) pseudo-octahedron, (b) intergrowth of tetrahedrons, (c) irregular fragment of heavily etched grain. BSE images: (d) tetrahedron with rounded and slightly etched tetrahedron surface, (e) intergrowths of sphalerite tetrahedrons with clay matter and siderite, (f) trigon-tritetrahedron. Sd = siderite.

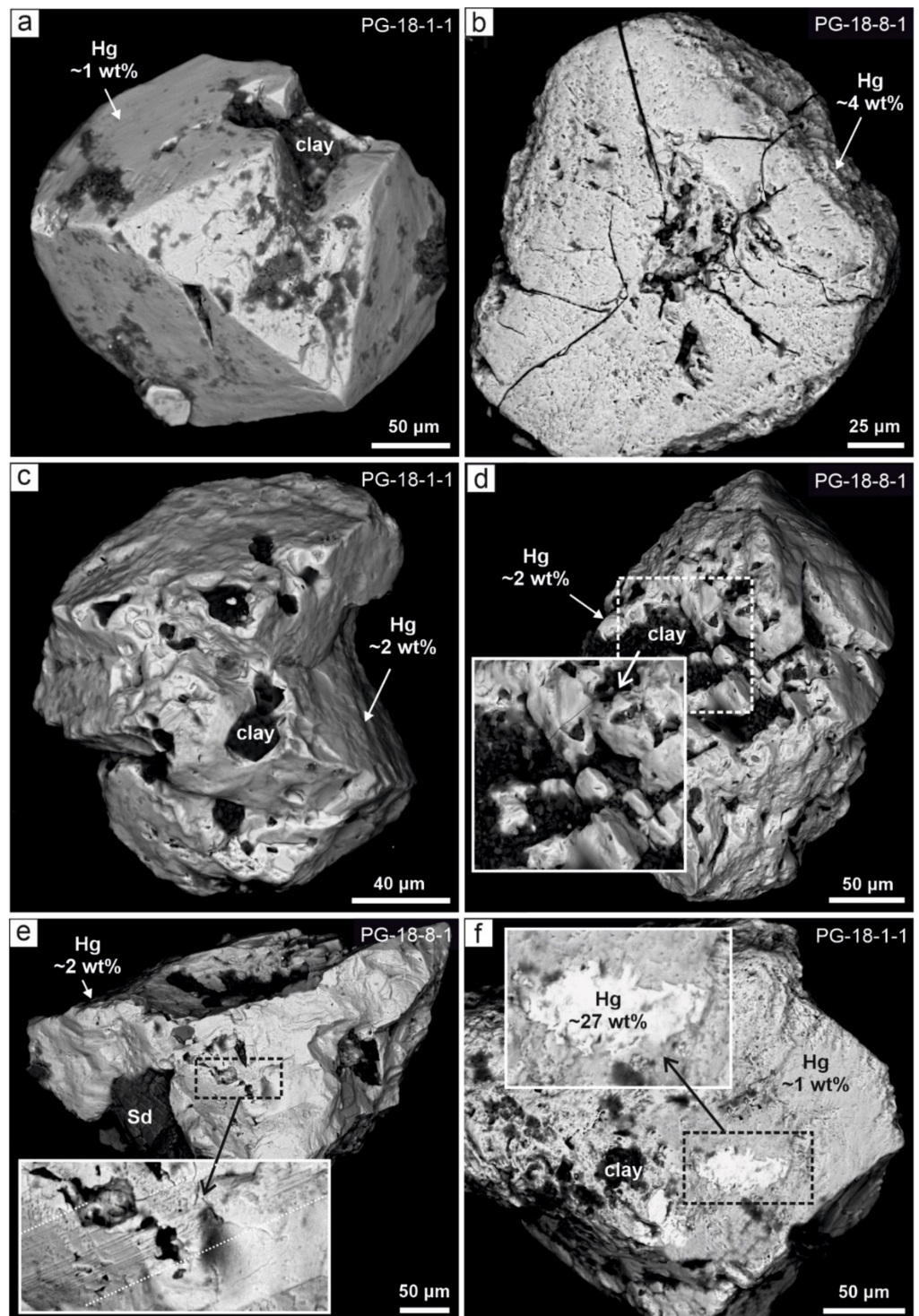


Figure 10. Morphology of medium-Hg and high-Hg sphalerites (1–27 wt% Hg) from mud masses of Pugachev MV, BSE images. (a) Tetrahedron with clayey matter inclusions. (b) Heavily etched rounded grain. (c,d) Sphalerite grains with smoothed edges and corners; its surface poisoned by clayey matter. (e) Intergrowth of siderite and sphalerite tetrahedron with a single set of polysynthetic twins. (f) Etched surface of sphalerite with high-Hg patches. Sd = siderite.

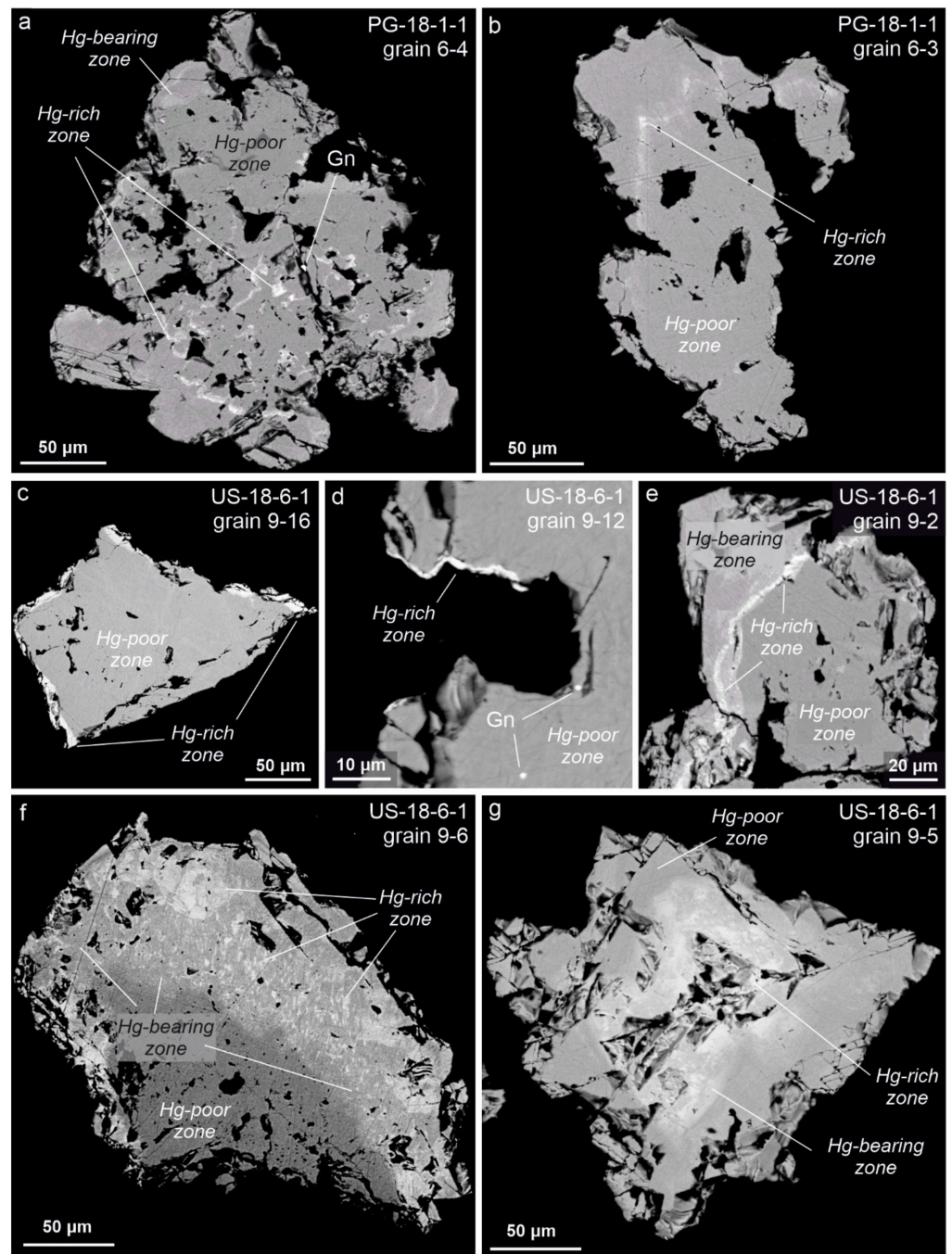


Figure 11. Back-scattered electron (BSE) images of mercury distribution in heterogeneous sphalerite. For specific Hg concentrations in sphalerites (a,b,f,g) see Tables 4 and 6. (a,b,e) wavy thin belts of high and moderate Hg contents in a Hg-poorer matrix. (c,d) Hg-poor sphalerite grain decorated by later Hg-rich rim. (f) mottled textures between Hg-rich and Hg-bearing clots in the Hg-enriched wide rim. (e) oscillatory zoning of Hg in sphalerite twin with high-Hg cores.

5.3.2. Chemistry

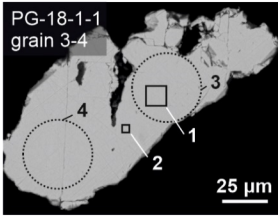
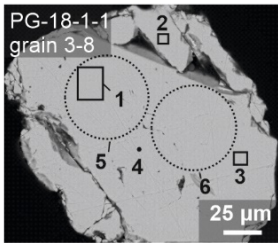
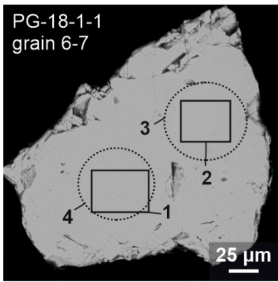
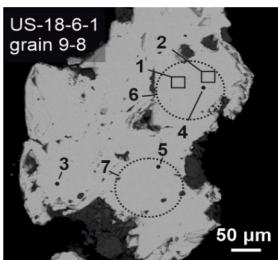
In addition to Zn and S, only Fe, Cd, and Hg were detectable by local microanalysis, while all other impurities were below the detection limits (Tables 4–6). In terms of mercury contents, sphalerites from the Sakhalin MV samples are low-Hg (hundreds of ppm to 1 wt%), medium-Hg (1–3 wt%), or high-Hg (3 to 26.9 wt%) varieties.

Table 4. Representative compositions (WDS) of sphalerite from mud masses of Pugachev and South Sakhalin MVs.

Sample	Grain	WDS Data, wt%					Formula Based on S = 1, apfu					
		Zn	Fe	Cd	Hg	S	Total	Zn	Fe	Cd	Hg	S
Pugachev MV												
PG-18-1-1	1-2	66.43	0.19	<0.15	<0.10	32.66	99.28	0.997	0.003	0.000	0.000	1.000
	1-3	66.00	0.16	<0.15	0.30	32.62	99.07	0.996	0.003	0.000	0.001	1.000
	2-1	66.29	<0.03	<0.15	<0.10	32.72	99.00	1.000	0.000	0.000	0.000	1.000
	2-3	66.43	0.48	<0.15	<0.10	32.66	99.57	0.992	0.008	0.000	0.000	1.000
	2-8	65.59	0.13	<0.15	1.04	33.32	100.08	0.993	0.002	0.000	0.005	1.000
	3-3	66.06	0.24	<0.15	<0.10	32.82	99.13	0.996	0.004	0.000	0.000	1.000
	3-8	66.27	0.13	<0.15	<0.10	32.89	99.3	0.998	0.002	0.000	0.000	1.000
	6-3 *	66.12	0.17	<0.15	<0.10	32.71	99.01	0.997	0.003	0.000	0.000	1.000
		63.72	0.37	<0.15	2.70	32.48	99.26	0.980	0.007	0.000	0.014	1.000
		62.08	0.70	<0.15	4.51	32.49	99.78	0.964	0.013	0.000	0.023	1.000
		61.11	0.63	<0.15	6.17	31.62	99.53	0.957	0.012	0.000	0.031	1.000
	6-4 *	65.80	0.31	0.22	0.31	32.55	99.21	0.991	0.005	0.002	0.002	1.000
		63.87	0.76	<0.15	1.69	32.74	99.06	0.978	0.014	0.000	0.008	1.000
		59.52	1.31	<0.15	7.79	32.01	100.63	0.936	0.024	0.000	0.040	1.000
		58.01	1.52	<0.15	10.01	31.33	100.87	0.920	0.028	0.000	0.052	1.000
	6-5	65.85	<0.03	<0.15	1.07	32.96	100.09	0.995	0.000	0.000	0.005	1.000
		64.96	0.14	<0.15	1.57	32.75	99.42	0.990	0.002	0.000	0.008	1.000
	6-6	66.10	0.21	<0.15	<0.10	32.79	99.1	0.996	0.004	0.000	0.000	1.000
	6-9	64.56	<0.03	<0.15	1.38	33.27	99.01	0.993	0.000	0.000	0.007	1.000
		62.90	0.45	<0.15	3.47	32.47	99.28	0.974	0.008	0.000	0.018	1.000
South Sakhalin MV												
US-18-4-4	4-3	66.56	<0.03	0.20	<0.10	32.90	99.66	0.998	0.000	0.002	0.000	1.000
	4-4	66.45	0.04	0.20	<0.10	32.41	99.10	0.998	0.001	0.002	0.000	1.000
65.96		<0.03	0.17	<0.10	32.56	99.10	0.998	0.000	0.002	0.000	1.000	
US-18-6-1	9-2 *	66.24	0.26	<0.15	<0.10	32.66	99.16	0.995	0.005	0.000	0.000	1.000
		62.62	0.85	<0.15	3.69	32.34	99.51	0.966	0.015	0.000	0.019	1.000
		57.18	1.78	<0.15	8.76	31.71	99.43	0.920	0.034	0.000	0.046	1.000
	9-5 *	65.63	0.09	<0.15	<0.10	33.50	99.21	0.999	0.001	0.000	0.000	1.000
		64.87	0.10	<0.15	1.96	32.56	99.48	0.988	0.002	0.000	0.010	1.000
		61.53	0.35	<0.15	5.55	31.98	99.42	0.965	0.006	0.000	0.028	1.000
		58.98	0.79	<0.15	9.47	31.59	100.82	0.936	0.015	0.000	0.049	1.000
		55.04	0.95	<0.15	14.09	30.45	100.53	0.906	0.018	0.000	0.076	1.000
US-18-6-1	9-6 *	66.01	0.08	<0.15	<0.10	32.96	99.05	0.999	0.001	0.000	0.000	1.000
		65.98	0.26	<0.15	0.25	32.99	99.48	0.994	0.005	0.000	0.001	1.000
		64.09	0.19	<0.15	2.26	32.56	99.09	0.985	0.003	0.000	0.011	1.000
		62.60	0.34	<0.15	4.77	32.63	100.34	0.970	0.006	0.000	0.024	1.000
		59.51	0.56	<0.15	7.61	31.78	99.47	0.950	0.010	0.000	0.040	1.000
		52.92	1.17	<0.15	16.43	29.87	100.39	0.887	0.023	0.000	0.090	1.000
	9-12 *	65.99	0.48	<0.15	<0.10	32.66	99.13	0.992	0.008	0.000	0.000	1.000
		56.07	0.49	<0.15	10.17	32.65	99.38	0.936	0.008	0.000	0.056	1.000
	9-16 *	66.44	0.11	<0.15	<0.10	32.49	99.03	0.998	0.002	0.000	0.000	1.000
		56.09	0.17	<0.15	10.26	32.62	99.14	0.941	0.003	0.000	0.056	1.000

* Sphalerite with heterogeneous Hg distribution characterized by analyses of low-Hg matrix, medium-Hg and high-Hg patches; Hg map is shown in Figure 11 and Table 6. apfu = atoms per formula unit.

Table 5. Representative back-scattered electron (BSE) images and compositions of sphalerite with homogenous Hg distribution; mud masses of Pugachev and South Sakhalin MVs, Sakhalin Island.

Pugachev MV											
BSE image	Data	Point	Zn	Fe	Ga	Ge	Hg	Cd	S	Total	
	EDS, wt%	1	65.98	<0.20	<0.30	<0.30	<0.30	<0.20	33.08	99.06	
		2	66.49	<0.20	<0.30	<0.30	<0.30	<0.20	32.99	99.48	
	LA-ICPMS, ppm	3	-	493	86.6	3292	101	634	-	-	
		4	-	440	89.5	3317	83.2	647	-	-	
	EDS, wt%	1	66.20	<0.20	<0.30	<0.30	<0.30	<0.20	32.99	99.19	
		2	66.28	<0.20	<0.30	<0.30	<0.30	<0.20	33.00	99.28	
		3	66.37	<0.20	<0.30	<0.30	<0.30	<0.20	33.41	99.78	
	WDS, wt%	4	66.27	0.13	<0.22	<0.30	<0.10	<0.15	32.89	99.30	
	LA-ICPMS, ppm	5	-	783	114	3367	132	330	-	-	
		6	-	808	141	3395	170	527	-	-	
	EDS, wt%	1	66.28	<0.20	<0.30	<0.30	<0.30	<0.20	33.09	99.37	
		2	66.88	<0.20	<0.30	<0.30	<0.30	<0.20	33.09	99.97	
	LA-ICPMS, ppm	3	-	268	130	3250	1365	351	-	-	
		4	-	270	88.6	3249	1331	332	-	-	
	South Sakhalin MV										
		EDS, wt%	1	67.00	0.26	<0.30	<0.30	<0.30	<0.20	33.44	100.87
2			66.33	0.38	<0.30	<0.30	<0.30	<0.20	33.26	99.97	
WDS, wt%		3	66.56	0.23	<0.22	<0.30	<0.10	<0.15	32.29	99.09	
		4	66.24	0.26	<0.22	<0.30	<0.10	<0.15	32.66	99.16	
		5	66.44	0.29	<0.22	<0.30	<0.10	<0.15	32.67	99.40	
LA-ICPMS, ppm		6	-	1551	257	3185	265	230	-	-	
		7	-	1675	284	3174	341	298	-	-	

- = not measured.

Table 6. Representative back-scattered electron (BSE) images and compositions of sphalerite with heterogenous Hg distribution; mud masses of Pugachev and South Sakhalin MVs, Sakhalin Island.

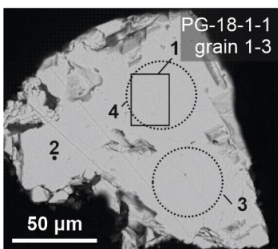
Pugachev MV										
BSE image	Data	Point	Zn	Fe	Ga	Ge	Hg	Cd	S	Total
	EDS, wt%	1	66.64	<0.20	<0.30	<0.30	<0.30	<0.20	32.96	99.60
	WDS, wt%	2	66.00	0.16	<0.22	<0.30	<0.10	<0.15	32.62	99.07
	LA-ICPMS, ppm	3	-	920	199	3389	857	422	-	-
		4	-	1264	235	3381	1292	346	-	-

Table 6. Cont.

Data	Point	Zn	Fe	Ga	Ge	Hg	Cd	S	Total
EDS, wt%	1	58.82	0.85	<0.30	<0.30	8.58	<0.20	31.55	99.80
	2	66.56	0.25	<0.30	<0.30	<0.30	<0.20	33.23	100.04
WDS, wt%	3	66.22	0.17	<0.22	<0.30	<0.10	<0.15	32.71	99.01
	4	62.90	0.45	<0.22	<0.30	3.47	<0.15	32.47	99.28
	5	63.72	0.37	<0.22	<0.30	2.70	<0.15	32.48	99.26
LA-ICPMS, ppm	6	-	1086	104	3119	534	619	-	-
	7	-	2017	58.7	3084	7507	563	-	-

South Sakhalin MV									
Data	Point	Zn	Fe	Ga	Ge	Hg	Cd	S	Total
EDS, wt%	1	66.21	0.19	<0.30	<0.30	<0.30	<0.20	33.21	99.61
	2	65.64	0.22	<0.30	<0.30	<0.30	<0.20	33.20	99.06
	3	66.73	<0.20	<0.30	<0.30	<0.30	<0.20	33.35	100.08
WDS, wt%	4	66.19	0.17	<0.22	<0.30	0.19	<0.15	32.72	99.27
	5	65.97	0.22	<0.22	<0.30	0.30	<0.15	32.63	99.13
LA-ICPMS, ppm	6	-	1314	294	3141	1487	259	-	-
	7	-	1088	259	3171	1082	296	-	-

Data	Point	Zn	Fe	Ga	Ge	Hg	Cd	S	Total
EDS, wt%	1	59.81	0.46	<0.30	<0.30	7.92	<0.20	31.56	99.75
	2	58.95	0.62	<0.30	<0.30	8.99	<0.20	31.20	99.76
	3	57.79	0.69	<0.30	<0.30	11.36	<0.20	30.86	100.70
	4	58.37	0.58	<0.30	<0.30	9.73	<0.20	30.97	99.65
	5	59.28	0.40	<0.30	<0.30	8.52	<0.20	31.37	99.57
WDS, wt%	6	66.01	0.08	<0.22	<0.30	<0.10	<0.15	32.96	99.05
	7	66.05	0.29	<0.22	<0.30	0.34	<0.15	32.59	99.28
	8	64.09	0.19	<0.22	<0.30	2.26	<0.15	32.56	99.09
	9	63.47	0.35	<0.22	<0.30	3.39	<0.15	32.57	99.78
	10	59.51	0.56	0.39	<0.30	7.61	<0.15	31.78	99.87
	11	-	2711	82.9	2968	14,053	710	-	-
LA-ICPMS, ppm	12	-	1811	145	3015	4566	571	-	-

- = not measured.

All medium-Hg and high-Hg sphalerite grains are inhomogeneous, with extremely Hg-rich sites of different shapes and sizes. Both textural and compositional heterogeneities of micron to hundreds of micron scale are detectable in BSE images and maps (Table 6, Figures 11–13).

Most often Hg-sphalerite grains contain thin irregular bands (Figure 11a,b,e); few grains had continuous 1 to 10 µm wide Hg-rich rims (Figure 11c,d) or up to 70 µm mottled rims with Hg-rich patches (Figure 11e,f and Figure 13a). All inhomogeneous grains show sharp contrasts between a low-Hg matrix and high-Hg sites (Tables 4 and 5, and Figure 6), except for a less prominent difference in one sphalerite twin (grain 9-5) with oscillatory zoning where up to 16.43 wt% Hg was recorded within a Fe-enriched core (Table 4, Figures 11g and 13b).

Iron is in a range of <0.03–0.50 wt% in 85 % of sphalerite analyses (WDS-EDS and SEM-EDS, n = 201), and sometimes shows a zoned pattern like Hg, but only in high-Hg grains, which is most prominent in elemental maps (Figures 12 and 13). The Fe contents are the lowest in low-Hg sphalerites (Tables 4 and 5), except for the 0.37–1.78 wt% values at sites with 1.69 to 16.43 wt% Hg (Tables 4 and 6). The contents of Hg and Fe show positive correlation in medium- and high-Hg sphalerites but do not correlate in low-Hg varieties (Figure 14). The Hg and Fe contents vary synchronously in different growth zones of both grains in the sphalerite twin (9–5) with the greatest Hg enrichment (Figure 13b).

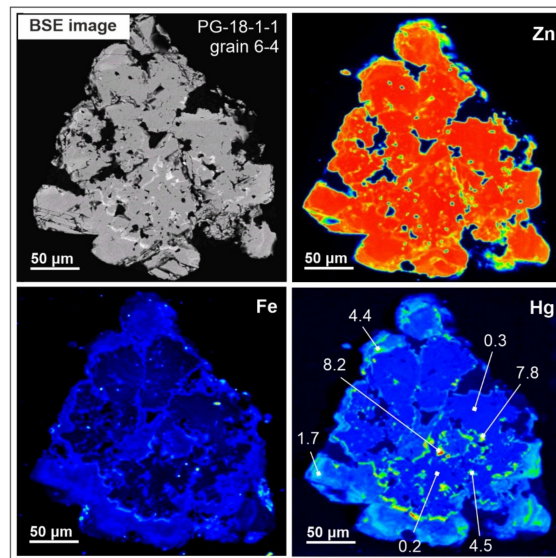


Figure 12. Back-scattered electron (BSE) images and element maps (Zn, Fe, Hg) showing irregular distribution of Hg in Pugachev MV sphalerite, with wt% Hg contents (EDS and WDS data) of selected points. For representative composition of sphalerite, see Table 4.

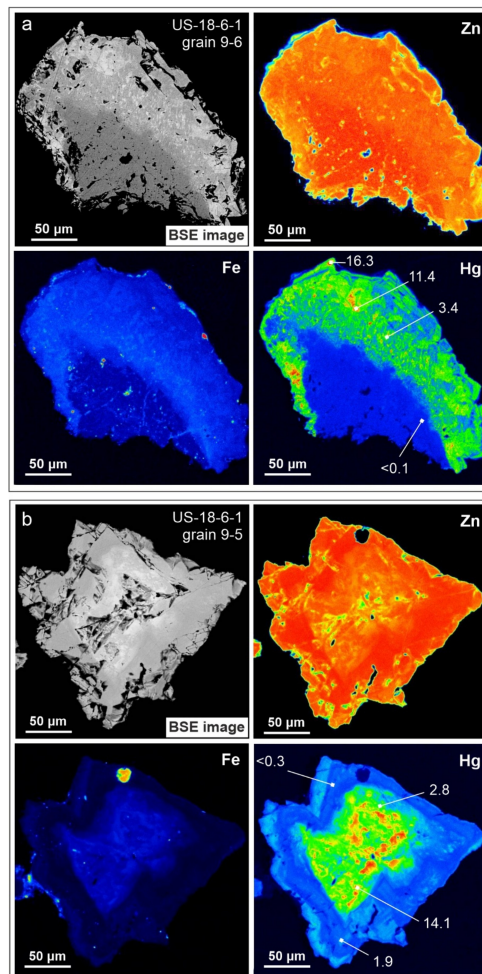


Figure 13. Back-scattered electron (BSE) images and element maps (Zn, Fe, Hg) of irregular (a) and zonal (b) distribution of Hg in South Sakhalin MV sphalerite. The numbers show Hg contents in wt% (WDS-EDS data). For representative compositions of the grains see Tables 4 and 6.

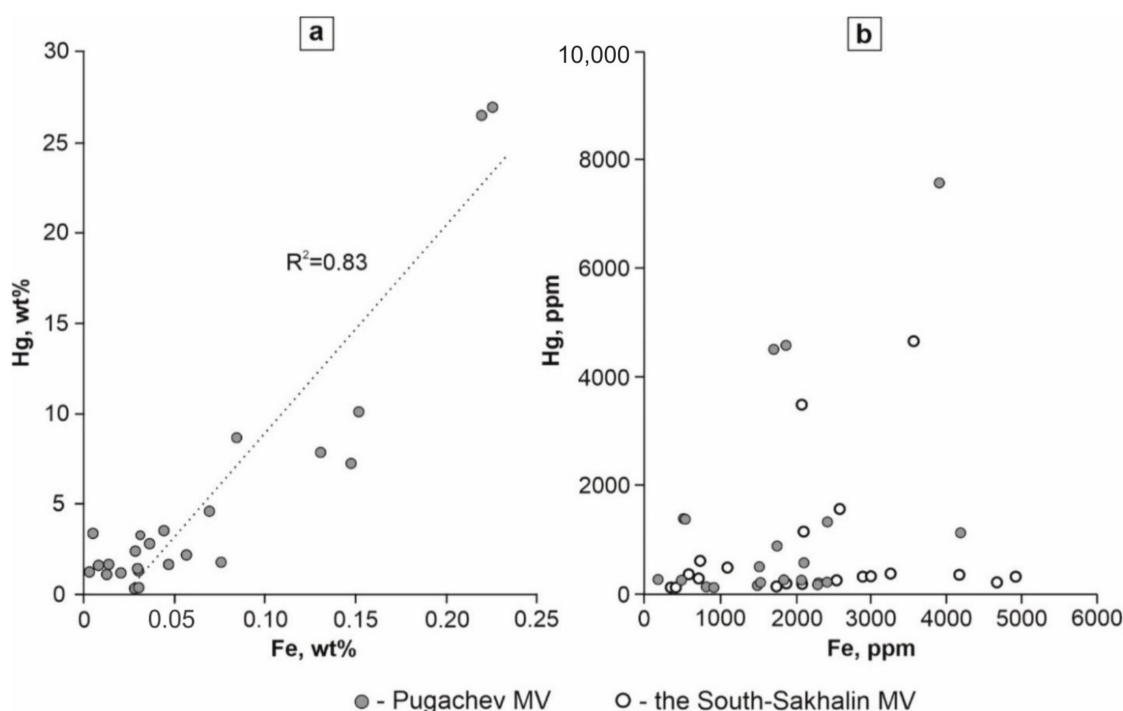


Figure 14. Hg/Fe ratios in shalerites from mud masses of Pugachev and South Sakhalin MVs. Hg and Fe contents: (a) in wt%, WDS-EDS data; (b) in ppm, LA-ICPMS data.

Cadmium in the analyzed shalerites was commonly below the EPMA or SEM-EDS detection limits and reached 0.20 wt% in two grains only (Tables 4–6). To avoid Hg contamination of the analyzer, the LA-ICPMS analysis was applied to sphalerite grains or sites where Hg was within 1.5 wt% (Tables 5 and 6). The LA-ICPMS data (Tables 7 and 8) show extremely large ranges of elements in low- and middle-Hg shalerites extracted from the Pugachev and South Sakhalin mud samples. The contents of Fe, Cd and Hg determined by LA-ICPMS match well with the EDS and WDS values (Tables 4–6).

Table 7. Average trace-element compositions of low-Hg sphalerite with homogenous Hg distribution from mud masses of Pugachev (n = 13) and South Sakhalin (n = 22) MVs, Sakhalin Island. LA-ICP-MS data, ppm.

	Pugachev MV			South Sakhalin MV		
	Average	Minimum	Maximum	Average	Minimum	Maximum
Mn	2.70	0.808	6.61	6.47	0.783	36.3
Fe	956	256	1519	946	205	2490
Co	7.14	0.78	19.4	8.76	0.691	30.8
Ni	0.255	0.019	5.76	0.478	0.028	4.32
Cu	248	151	411	188	3.02	388
Ge	3295	3180	3395	3258	3123	3408
Ga	91.1	37.7	536	86.2	2.68	284
As	8.96	0.600	50.9	5.03	0.299	132
Se	84.6	33.6	162	99.3	37.5	172
Ag	4.80	1.04	10.9	5.75	0.711	16.5
Cd	455	89.0	679	997	129	3964
In	1.31	0.31	11.3	1.54	0.049	6.91
Sb	56.4	14.0	219	61.9	1.25	576
Hg	153	81.0	232	222	69.4	564
Tl	0.293	0.018	0.607	0.357	0.008	8.74
Pb	52.2	6.95	150	46.1	0.732	605
Bi	0.210	0.034	0.778	0.530	0.010	2.07

Table 8. Average trace-element compositions of low- and medium-Hg sphalerite with heterogenous Hg distribution from mud masses of Pugachev (n = 6) and South Sakhalin (n = 12) MVs, Sakhalin Island. LA-ICP-MS data, ppm.

	Pugachev MV			South Sakhalin MV		
	Average	Minimum	Maximum	Average	Minimum	Maximum
Mn	5.02	2.80	7.24	5.92	0.763	17.7
Fe	950	268	2168	1832	907	5621
Co	27.7	4.77	50.4	27.1	6.23	52.2
Ni	—	bdl	bdl	1.15	0.124	1.00
Cu	309	94.8	528	397	169	901
Ge	3337	3249	3396	3113	2968	3305
Ga	156	51.8	235	128	16.1	294
As	6.63	0.486	12.5	10.2	0.713	33.3
Se	73.6	25.4	120	72.5	29.9	297
Ag	4.56	2.21	30.3	5.42	1.26	11.8
Cd	393	242	666	504	259	710
In	0.945	0.064	3.92	3.59	0.184	9.72
Sb	131	22.1	3.42	79.2	10.1	149
Hg	1058	456	1365	5412	284	22358
Tl	0.121	0.054	0.381	0.154	0.016	0.497
Pb	47.7	11.3	92.9	45.4	11.9	107
Bi	0.201	0.037	0.883	0.367	0.044	0.631

bdl = below detection limit; - = not measured.

Analysis by LA-ICPMS was applied to selected sphalerite sites free from obvious inhomogeneities (inclusions, defects, grain boundaries, etc.), but some grains still showed spikes or at least elevated contents of some elements (Figures 15 and 16).

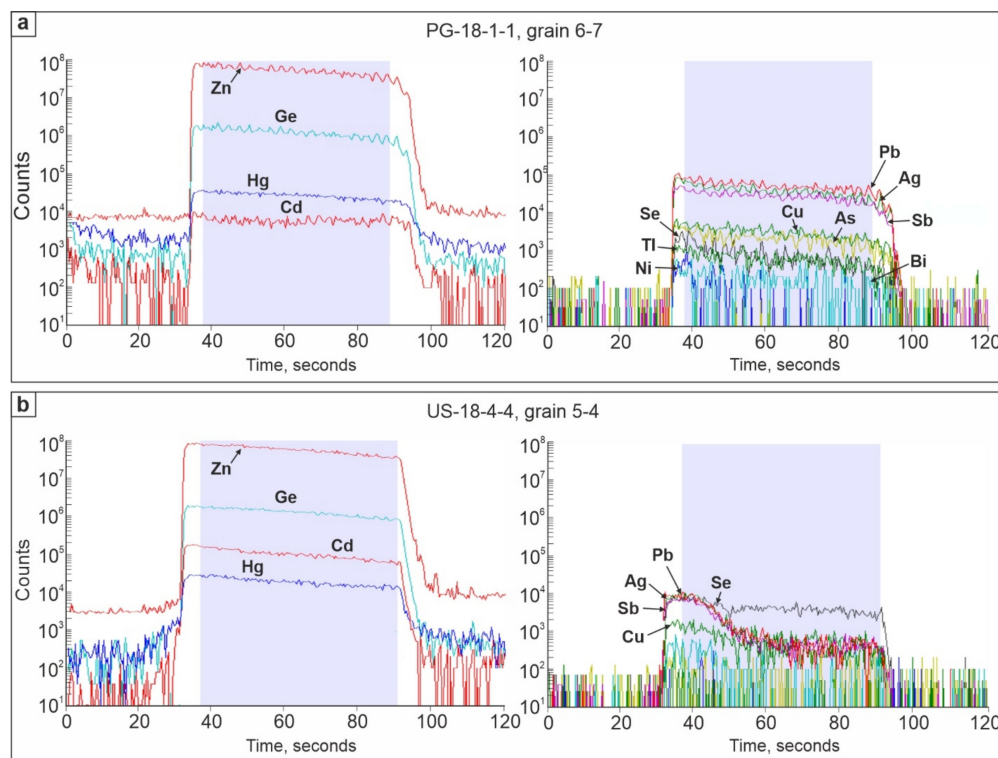


Figure 15. Representative single-spot LA-ICPMS spectra (blue shading) for selected elements in homogenous low-Hg sphalerites without mineral inclusions (a) and with Pb-Sb-Cu-(Ag) sulfosalts micro-scale inclusion (b). For sphalerite compositions, see Tables 4 and 6.

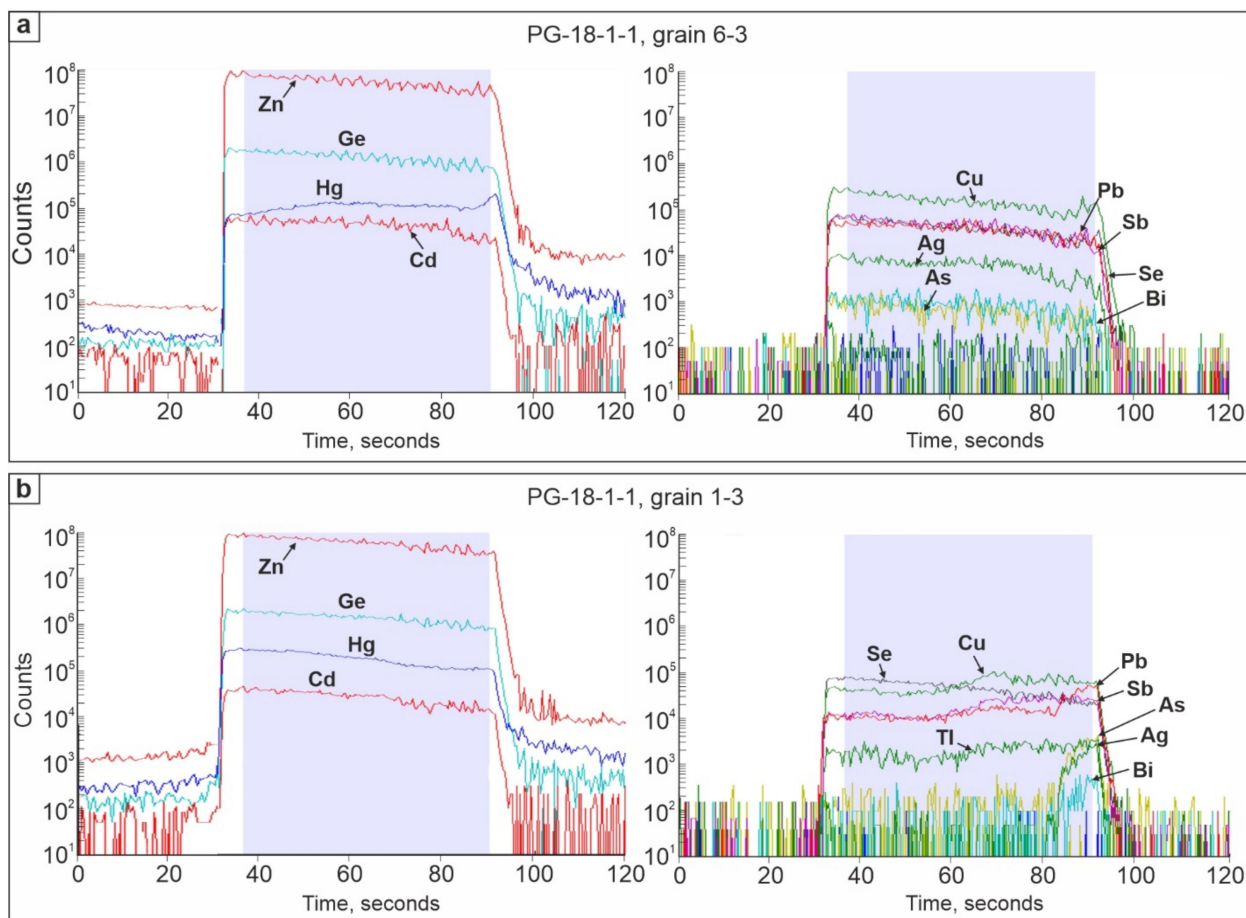


Figure 16. Representative single-spot LA-ICPMS spectra (blue shading) for selected elements in heterogeneous medium-Hg sphalerites without mineral inclusions (a) and with Pb-Sb-(Cu-Ag-Bi) sulfosalt and/or galena inclusions (b). For details of Hg distribution see Figures 11 and 13. For sphalerite compositions see Tables 4 and 6.

The ablation profiles were smooth for Ge, Cd, In, Mn, Co, and Tl, which thus were evenly distributed on the spot scale [1]. The distribution of mercury was even in low-Hg sphalerites and in the Hg-poor matrix of Hg-bearing grains (Figures 15 and 16b, Tables 4 and 5). The profiles of other elements (Sb, Pb, Bi, and Ag, as well as Cu, Se, and As in some samples) were sometimes irregular, possibly, because of micrometer inclusions of the respective minerals (Figures 15b and 16). This inference was confirmed by findings of sporadic Pb-Sb-(Cu,Bi) sulfosalt, galena, and Ag sulfide mineral microinclusions. It was reasonable to expect the corresponding element spikes, since the LA-ICPMS spot size far exceeded the sizes of the inclusions (Table 6 and Figure 11d). The trace-element compositions of low-Hg (1) and medium- or high-Hg (2) sphalerites with evenly and unevenly distributed Hg, respectively, are considered separately below.

All analyzed sphalerites of group 1 are depleted in Fe (1833 ppm in Pugachev MV and 2153 ppm in South Sakhalin MV) and in Mn but have abnormal Ge contents, with narrow ranges of 3123 to 3408 ppm at both MV edifices (Table 7). Both Fe and Mn show minor variability, with the highest contents in a single grain. Cadmium is commonly in hundreds of ppm, without spikes, in low-Hg homogeneous sphalerites from Pugachev MV, and is notably higher in South Sakhalin MV. The average concentrations of Cu, Ga, Se, Sb, and Pb are low and comparable in both MVs. The sphalerites of this group are also remarkable in very low contents of As, Co, Ag, In, Bi, Tl and Ni. Frequent sporadic, often coupled, spikes in Sb (up to 218 ppm and 576 ppm) and Pb (up to 141 ppm and 605 ppm) most likely result from entrapped Pb-Sb sulfosalt inclusions within the analyzed spots (Figures 15 and 16). Few spikes of Ga (up to 536 ppm), In (11.3 ppm) and Ni (5.76 ppm)

were observed in sphalerites from the Pugachev mud samples, whereas As spikes (up to 132 ppm) were restricted to those from South Sakhalin MV.

The trace element compositions of high- and medium-Hg sphalerites with unevenly distributed Hg (group 2) are generally similar to those of group 1 (Tables 7 and 8), with Ge enrichment and depletion in Fe and Mn. The contents of Se, Pb, As, Ag, Bi, and Tl are comparable between the two volcanoes and with the respective values in the group 1 sphalerites. On the other hand, the sphalerites of group 2, from both MVs, contain more Cu, Ga, Co and In; Cd is higher in the South Sakhalin sphalerites (504 ppm average, single spike of 1578 ppm) than in those of the Pugachev samples (393 ppm Cd, no spikes).

The majority of sphalerite grains with unevenly distributed Hg are from South Sakhalin MV. The average Hg content in their matrix (LA-ICPMS determination) reaches 5415 ppm and the maximum value is 22,358 ppm (Table 8). Inhomogeneous sphalerite grains in the Pugachev mud samples are very sporadic and have quite similar values of average and maximum Hg contents in the matrix (1058 ppm and 1365 ppm, respectively). Concentrations of Mo, Te, and Au exceed their detection limits in only few cases and show no significant difference between the sphalerites of groups 1 and 2. Nickel contents rarely exceed the detection limit. Cobalt varies from $n \cdot 10^{-1}$ to few tens of ppm, with a single spike coupled with those of Fe and Cu, apparently due to the presence of a complex Fe-Cu sulfide inclusion. Bismuth is commonly within $n \cdot 10^{-2}$ to $n \cdot 10^{-1}$ ppm and exceeds 1 ppm in four grains only.

5.3.3. X-ray Diffraction and Crystal Structure

Single-crystal experiments were applied to five natural samples of the ZnS_{cub} - HgS_{cub} series containing 83.2 ppm to 80.25 wt% Hg. Crystal structure was resolved in three pure transparent sphalerite grains from the South Sakhalin and Pugachev mud samples (Table 9), as well as in Zn-bearing metacinnabar from Pugachev MV ($Hg_{3.42}Zn_{0.39}Fe_{0.05}Ni_{0.04}\Sigma_{3.90}S_4$, (Table 9 and Figure 8a) and a fragment of Hg-rich sphalerite from the Idermeg-Bayan-Khan-Ula polysulfide-fluorite deposit in Mongolia ($(Zn_{3.704}Hg_{0.244})\Sigma_{3.95}S_4$, Tables 1 and 9). All samples have deficit of cations in chemical analyses.

Table 9. Unit-cell metrics and composition of (Zn,Hg)S.

Sample	Grain	EDS-WDS Data, Average Composition	XRD, Refinement of Structure	a_{exp} , Å	a_{calc} , Å
PG-18-1-1	1-2	$(Zn_{0.995}Fe_{0.01})\Sigma_{0.996}S$	$Zn_{4.01(2)}S_4$	5.40658(13)	5.40728
PG-18-1-1	6-3	$(Zn_{0.975}Hg_{0.02}Fe_{0.01})\Sigma_{0.979}S$	$Zn_{3.948(12)}Hg_{0.052(12)}S_4$	5.40415(18)	5.41339
US-18-6-1	9-5	$(Zn_{0.950}Hg_{0.03})\Sigma_{0.953}S$	$Zn_{3.904(12)}Hg_{0.096(12)}S_4$	5.4208(2)	5.4209
III-8b/1	1	$(Zn_{0.943}Hg_{0.051})\Sigma_{0.961}S$	$Zn_{3.776(16)}Hg_{0.224(16)}S_4$	5.4345(5)	5.4336
PG-18-1-1	2	$(Hg_{0.855}Zn_{0.09}Fe_{0.01})\Sigma_{0.955}S$	$Hg_{3.56(12)}Zn_{0.44(12)}S_4$	5.83204(18)	5.82565

The details of data acquisition and structural parameters of the samples are summarized in Table 10. The samples of ZnS_{cub} , with 83.2 ppm Hg (grain 1-2, PG-18-1-1), and zincian metacinnabar (grain 2, PG-18-1-1) are twinned on the (111) plane and have relative twin domain sizes of 0.79/0.21 and 0.56/0.44, respectively. The twinning was taken into account while integrating the analytical intensities. The structure was refined using diffraction arrays for the larger domain. Grains 6-3 (sample PG-18-1-1) and 9-5 (sample US-18-6-1) are medium-Hg and high-Hg sphalerites with strongly uneven Hg distribution (Tables 4 and 6, Figure 11b,g and Figure 13b). The structure of these samples, each comprising two slightly disoriented domains, was refined using the diffraction arrays of the domains occupying 85–90 vol.% in each sample. The disorientation angle is quite small (0.90 – 1.08°) in three sphalerite samples, slightly larger (1.63°) in metacinnabarite, and the greatest (4.88°) in the high-Hg sphalerite from Mongolia (grain 1; sample III-8b/1), which is likewise a {111} twin with the 0.78/0.22 domain ratio (Table 10).

Table 10. Data collection and structure refinement details for (Zn,Hg)S.

Sample Grain	PG-18-1-1 1-2	PG-18-1-1 6-3	US-18-6-1 9-5	III-8b/1 1	PG-18-1-1 2	
Crystal size (μm)	$420 \times 330 \times 20$	$170 \times 150 \times 120$	$230 \times 200 \times 150$		$150 \times 70 \times 60$	
Space group	$F\bar{4}3m$	$F\bar{4}3m$	$F\bar{4}3m$	$F\bar{4}3m$	$F\bar{4}3m$	
Mosaicity (deg.)	0.90	0.96	1.08	4.88	1.63	
a (\AA)	5.40658(13)	5.40415(18)	5.4208(2)	5.4345(5)	5.83204(18)	
V (\AA^3)	158.040(11)	157.827(16)	159.288(18)	160.50(4)	198.364(18)	
d (g/cm^3)	4.095	4.185	4.204	4.340	7.224	
$F(000)$	184	187	189	195	359	
μ ($\text{MoK}\alpha$) (mm^{-1})	16.178	17.426	18.082	20.363	69.951	
θ range for data collection	6.536–29.458	6.540–29.478	6.518–29.369	6.503–29.297	6.058–29.174	
Scan width ($^\circ$ /frame)	1	1	1	1	1	
Exposure (min/frame)	5	5	10	10	10	
No. of measured reflections	1162	1198	668	935	641	
No. of unique reflections	34	38	38	37	40	
No. of observed reflections ($I > 2\sigma(I)$)	34	38	38	37	40	
R_{int}	0.1515	0.0683	0.0949	0.0982	0.3038	
No. of parameters refined	6	4	4	5	4	
Flack parameter	0.01(11)	0.11(6)	0.05(6)	0.08(7)	−0.1(4)	
$R1, wR2$ for $I > 2\sigma(I)$	0.0195, 0.0463	0.0157, 0.0401	0.0168, 0.0395	0.0213, 0.0517	0.0621, 0.1459	
$R1, wR2$ all data	0.0195, 0.0463	0.0157, 0.0401	0.0168, 0.0395	0.0213, 0.0517	0.0621, 0.1459	
GoF	1.167	1.325	1.161	1.469	1.316	
Residual electron density ($e/\text{\AA}^3$)	0.453, −0.560	0.273, −1.014	0.398, −0.633	0.495, −0.676	1.444, −1.991	
Atomic position parameters (coordinates, U_{eq} (\AA^2) values, and occupancies) and interatomic distances (\AA)						
M ($\frac{1}{4}, \frac{1}{4}, \frac{1}{4}$)	Occ.	$\text{Zn}_{1.003(7)}$	$\text{Zn}_{0.987(3)}\text{Hg}_{0.013(3)}$	$\text{Zn}_{0.976(3)}\text{Hg}_{0.024(3)}$	$\text{Zn}_{0.944(4)}\text{Hg}_{0.056(4)}$	$\text{Hg}_{0.89(3)}\text{Zn}_{0.11(3)}$
	U_{eq}	0.0110(12)	0.0116(2)	0.0126(3)	0.0134(4)	0.0310(12)
S (0,0,0)	U_{eq}		0.0094(4)	0.0107(5)	0.0131(4)	0.021(6)
	$M-S(6\times)$	2.34112(6)	2.34022(7)	2.34726(8)	2.3532(2)	2.52535(8)

The powder diffraction pattern generated from the frames of a single-crystal diffraction experiment for the Mongolian high-Hg sphalerite includes a peak corresponding to 100 reflection of wurtzite (Figure 17). However, this peak is absent from the diffraction profiles of other analyzed samples, with five times smaller disorientation angles.

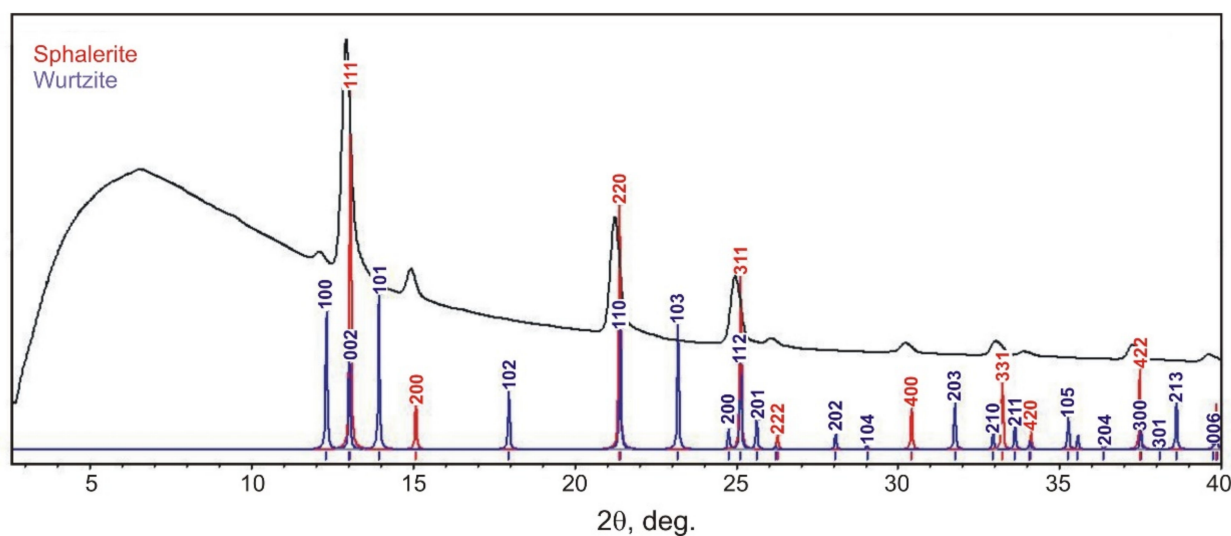


Figure 17. The powder diffraction pattern generated from the frames of a single crystal diffraction experiment of Mongolian high-Hg sphalerite in comparison with calculated powder diffraction patterns of sphalerite (red line) and wurtzite (blue line).

The collected spectra were of modest quality but allowed refining the structure of all five ZnS–HgS samples, including the occupancy of mixed cation M-sites (Tables 9 and 10). The structure refinement results show that the Hg occupancy of M-sites in low-, medium-, and high-Hg sphalerites determined by the XRD analysis is consistent with the average values obtained by chemical analyses.

The analyzed medium- and high-Hg sphalerites have larger unit-cell sizes than pure ZnS_{cub} , with the a -parameter increasing linearly with the share of Hg in the M-sites. It is related with the M occupancy of Hg as a (Å) = 5.40664(13) + 0.4929(3) × Occ(Hg) (Figure 18). Note that the point corresponding to low-Hg sphalerite 2 departs from this trend, and its a -parameter is even smaller than in Hg-free sphalerite. At low Hg contents, its M occupancy is apparently determined to a larger error.

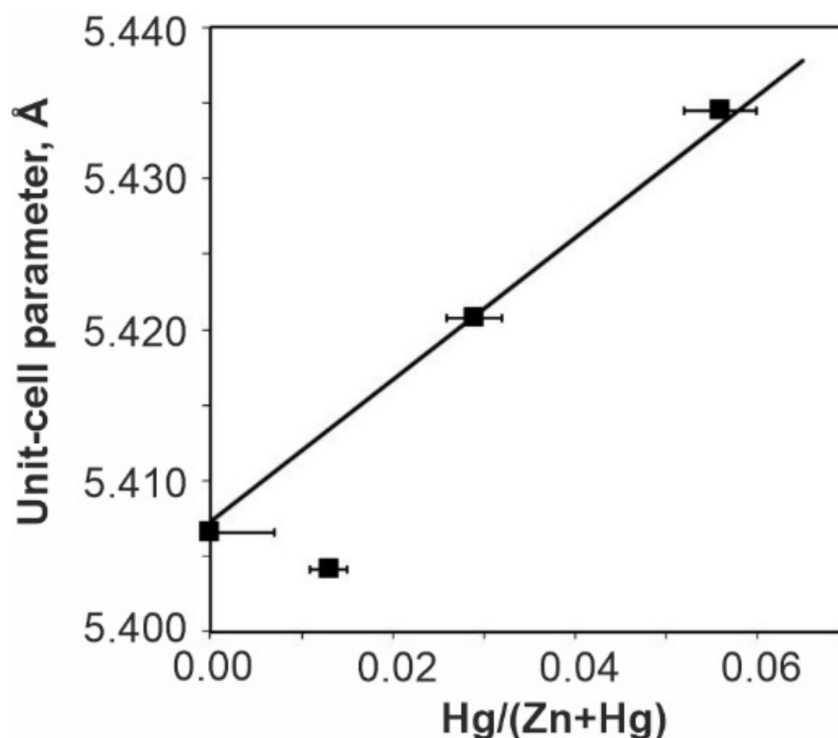


Figure 18. Unit-cell a -parameter of (Zn,Hg)S vs. Hg/(Zn + Hg) ratio.

5.3.4. Raman Spectroscopy

The Raman spectra of Hg-poor and Hg-rich sphalerites from South Sakhalin MV (Figure 19) exhibit one very strong band at 337–339 cm^{-1} and three weak bands at 300, 349 and 363 cm^{-1} . The 300 cm^{-1} band is the strongest in the zones of highest Hg contents and the weakest in the low-Hg zones of the grain. The spectra of high-Hg areas lack the single strong band at 253 cm^{-1} expected in the presence of cinnabar. Thus, the Hg-rich sphalerite sample was identified as a (Zn,Hg)S solid solution with a zincblende-type of structure (ZnS_{cub} , $F43m$).

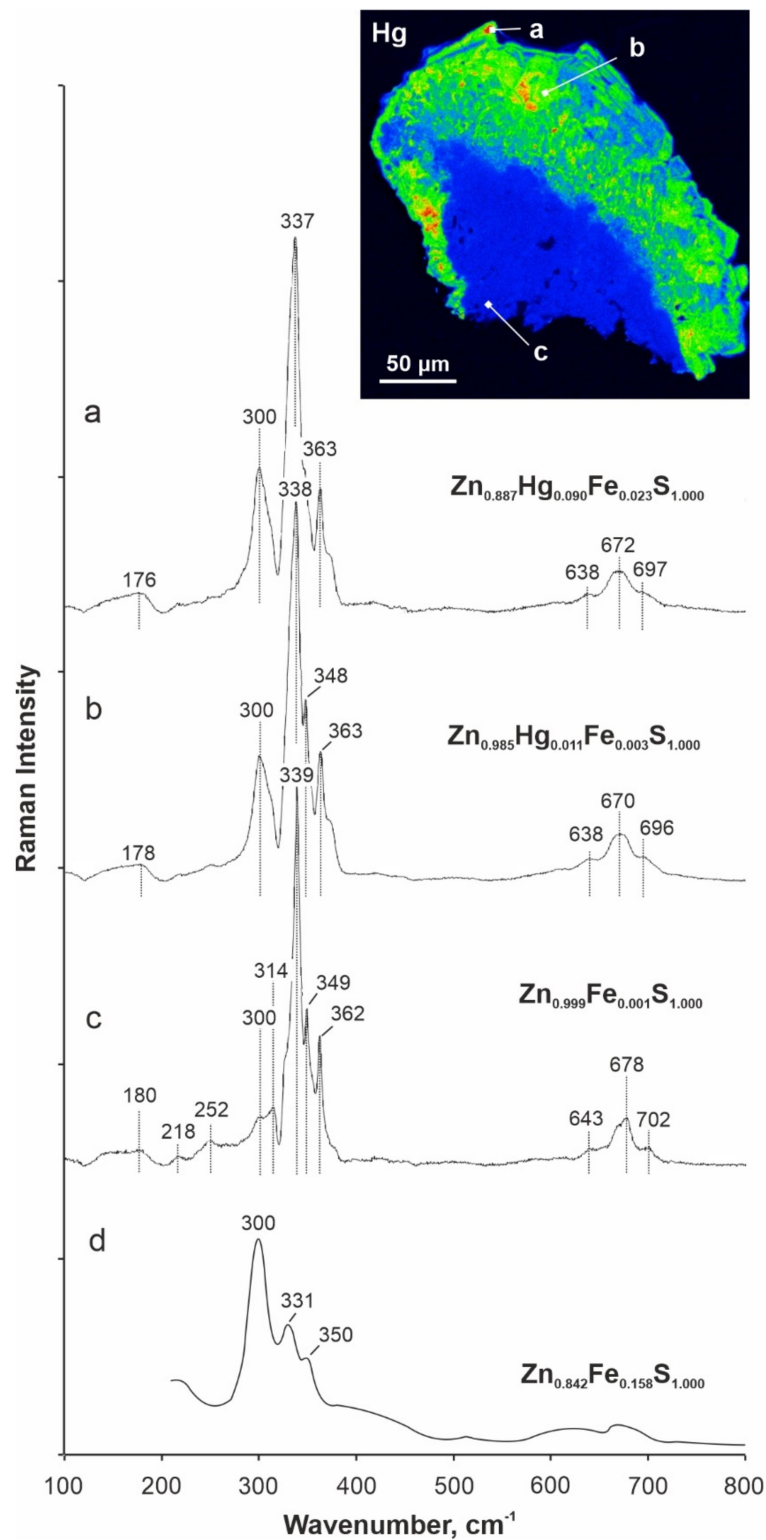


Figure 19. Raman spectra of high- (a) medium- (b) and low-Hg (c) sphalerite from South Sakhalin MV (grain 9-6, sample US-18-6-1) compared with Fe-enriched sphalerite (d) from Romania [72]. For details of Hg distribution see Figures 11 and 13. For sphalerite compositions see Tables 4 and 6.

6. Discussion

6.1. Trace-Element Fingerprints of Sakhalin MV Sphalerites

The sphalerites from the mud masses of South Sakhalin and Pugachev volcanoes have very low contents of In (1.41 and 3.14 ppm for low- and medium-Hg compositions,

respectively), low Fe, Ga (72.5 and 106 ppm average), and Co (~9 ppm and ~25 ppm on average), but are highly enriched in Ge (~3300 ppm average) and regularly bear 1–5 wt% up to 27 wt% Hg (Tables 6–8).

The contents of Ge are very high in all analyzed sphalerites and reach the maximum of 3000 ppm known so far [73]. This fact again demonstrates that germanium accumulates preferably in low-Fe sphalerite [74–77]. According to [1] and [16], Ge^{2+} would more likely incorporate into the sphalerite structure by complex heterovalent substitutions rather than substituting directly for Zn^{2+} in sphalerite and wurtzite. On the other hand, the presence of some other trace elements (e.g., Ag, Cu) would appear to enhance the incorporation accordingly [76,78], with a general coupled substitution mechanism for trivalent and tetravalent elements (including Ge^{4+}). However, the elements (Ag, Cu, Cd, Mn, Ga, Tl, In, Sn) that can be involved in complex heterovalent substitutions, together with Ge, have low concentrations in the Sakhalin sphalerites (Tables 7 and 8), and the Hg contents vary within four orders of magnitude while Ge remains nearly constant. Thus, the coupled substitution appears to be an unlikely mechanism of Ge incorporation into the Sakhalin sphalerites. The even distribution and poor variability of Ge in all analyzed grains (Figures 15 and 16, Tables 6 and 7) is rather consistent with direct $\text{Zn} \rightarrow \text{Ge}$ substitution, with or without M-site vacancies depending on the valence of Ge (Ge^{4+} or Ge^{2+}). Following [14] and [16], we propose that Ge^{4+} substitutes for Zn^{2+} in the Sakhalin sphalerites, while vacancies provide charge balance compensation.

The Hg contents in the sphalerite grains reach 27 wt% (17 mol% HgS). Mercury is distributed evenly in low-Hg sphalerites (<1500 ppm), but the patterns in higher-Hg varieties are highly heterogeneous and show no crystallographic control (Figures 11a,b,e and 12). In most of the analyzed grains, Hg concentrations locally increased from the 1000–500 ppm background to 8.6–11.4 wt% or even as high as 27 wt% (Table 5; grains 6-3 and 9-6) and then fell back to the background, with sharp Hg-poor/Hg-rich interfaces. The Hg heterogeneity was confirmed and visualized in 2D SEM-EDS images and elemental maps (grain sections), as well as in 3D LA-ICPMS data (Figures 11–13, 15 and 16). Specifically, we have discovered thin Hg-rich rims grown over crushed fragments of low-Hg sphalerites (Figure 11c,d and Table 5), which obviously postdated the formation of the low-Hg grains. Only two samples had Hg-rich cores (grain 9-5) or intermediate zones (grain 9-6) inside single crystals and/or twinned sphalerites (Figure 11f,g). The Hg contents in sphalerites have no correlation with other impurities, except for a trend of Hg-Fe co-accumulation in the Pugachev MV sphalerites (Figure 14).

6.2. Hg and Ge in the ZnS Structure

Although sphalerite with medium or high Hg contents and Zn-bearing metacinnabar in complex sulfide deposits are often found worldwide and have been largely studied [1,3,4,79–82], some issues remain unresolved, such as Hg incorporation into the ZnS structure, Hg valence, or ranges of $(\text{Zn,Hg})\text{S}_{\text{cub}}$ and $(\text{Hg,Zn})\text{S}_{\text{cub}}$ solid solutions [1,3,83].

High-temperature experiments on the synthesis of $(\text{Zn}_{1-x}\text{Hg}_x)\text{S}_{\text{cub}}$ solid solutions demonstrated the existence of homogeneous intermediate compounds in the sphalerite–metacinnabar series. The experiments were run in different pressure-temperature conditions: (i) >350 °C and 1 kbar [4,84]; (ii) 550, 700, and 800 °C, and ambient pressure [85]; (iii) 610–670 °C and ambient pressure [83]. The results showed complete miscibility between cubic HgS and ZnS phases at >350 °C, and the existence of a high-temperature solid solution with a sphalerite-like structure (Figure 20), the so-called “Hss” [4]. At lower temperatures, the ZnS–HgS diagram splits into two parts: Hss breaks down into zincian metacinnabar and Zn-free cinnabar in the Hg-rich domain (≥ 85 mol% HgS) and two distinct solid solutions (Zn- and Hg-rich), both with a ZnS structure, in the Zn-rich domain with 25–84 mol% HgS [84]. The stable low-temperature (<200 °C) assemblage includes cinnabar and Hg-sphalerite (with up to 22–25 mol% HgS). Thus, metacinnabar in equilibrium systems is a high-temperature HgS cubic polymorph, which is expected to convert into trigonal HgS (cinnabar) at lower temperatures. There is evidence, however, that high

contents of Fe and/or Zn in the natural (Hg,Fe,Zn)S phase severely retard or preclude the metacinnabar-to-cinnabar conversion under low temperatures, i.e., zincian metacinnabar can persist as a metastable phase in geological systems under ambient conditions [3,4]. According to the ZnS–HgS diagram [84], the equilibrium Hg content in sphalerite at 100 °C likewise remains high, up to 23 mol% HgS (48 wt% HgS).

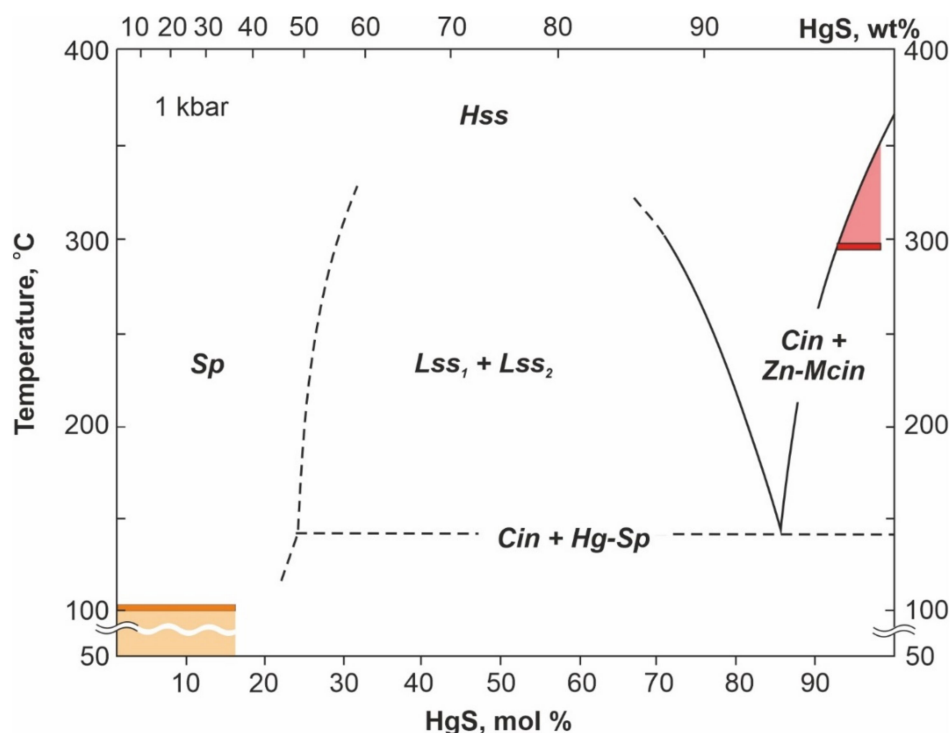


Figure 20. Phase diagram of the system ZnS–HgS after [4]. Brownish (sphalerite) and purple (zincian metacinnabar) colors highlight the composition ranges of sulfides from mud masses of Pugachev and South Sakhalin MVs, Sakhalin Island. Cin = cinnabar. Hg-Sp = mercury sphalerite. Hss = high-temperature (Zn,Hg)S solid solution with sphalerite structure. Lss = low-temperature solid solution. Sp = sphalerite. Zn-Mcin = zincian metacinnabar. Minimal temperature of metacinnabar formation was estimated as high as 295 °C based on its Zn content. Temperature interval (50–106 °C) of the formation of Sakhalin sphalerite was estimated by GGIMFis thermometer [86].

The available evidence from several Hg deposits, such as Nikitovka (Ukraine), Khaidarkan (Kyrgyzstan), Aktash, Azrak, and Kadyrel (Russia), Dzhizhikrut (Uzbekistan), Idermeg-Bayan-Khan-Ula (Mongolia), with ≤ 250 °C formation temperatures [3], demonstrates convincingly that Hg-rich sphalerites with up to 35–38 wt% Hg (commonly low-Fe but with low-medium or high Cd contents) often coexist with zincian metacinnabar (with 0.10–0.29 apfu Zn) instead of Zn-free cinnabar. Hg-sphalerite is often main carrier of mercury in assemblages that lack both cinnabar and metacinnabar. There is no correlation among Hg, Fe and Cd in the sphalerites. Although a $\text{ZnS}_{\text{cub}}\text{--HgS}_{\text{cub}}$ continuous solid solution series exists at >350 °C, no intermediate compositions between $(\text{Zn}_{0.75}\text{Hg}_{0.25})\text{S}$ and $(\text{Hg}_{0.54}\text{Zn}_{0.46})\text{S}$ have been ever discovered in nature [3].

All Hg deposits listed above contain only restricted solid solutions that belong to the sphalerite structural type: $\beta\text{-(Zn,Hg,Cd)S}$ and $\beta\text{-(Hg,Zn,Cd)S}$ (Figure 20), whereas neither hexagonal $(\text{Zn,Cd,Hg})\text{S}$ solid solutions (Hg-wurtzite or Hg-greenockite), nor potentially new $(\text{Hg,Zn})\text{S}_{\text{hex}}$ or $(\text{Hg,Cd})\text{S}_{\text{hex}}$ minerals are known in natural occurrence [3]. This is an expected fact because most of Hg chalcogenic compounds (metacinnabar HgS, tiemannite HgSe, and coloradoite HgTe) crystallize in the sphalerite type, but no wurtzite-type HgS(Se,Te) compounds are known [1,87].

Particular Hg-sphalerite-cinnabar intergrowths were reported [81] from the low-temperature Sb-As-Zn-Hg ore assemblage of the Helmo Au deposit (Ontario, Canada). The regular grid-like textures of cinnabar (~77%) and Hg-sphalerite (~23%) with 24 wt% HgS, which obviously have crystallographic controls, were interpreted to have exsolved from a high-temperature homogeneous phase with the $(\text{Hg}_{0.6}\text{Zn}_{0.4})\text{S}$ starting composition. To our knowledge, this is the only reconstructed composition of natural ZnS-HgS compounds that falls within the $(\text{Hg,Zn})\text{S}$ exsolution series. The solid solution compositions were restricted to the $(\text{Zn}_{1.00-0.75}\text{Hg}_{0.0-0.25})\text{S}$ interval, as the initial formation temperature of Hg-rich sphalerite was most often below 250–300 °C [3,4].

The sphalerite structure can accommodate many ions comparable in size with tetrahedrally-coordinated Zn^{2+} and has affinity to tetrahedral coordination due to sp^3 hybridization, which is typical of Cd^{2+} , Hg^{2+} , Fe^{2+} , Mn^{2+} , Ga^{3+} , In^{3+} , Ge^{4+} , and Ag^+ [87]. The group 12 metals, Zn, Cd and Hg share the greatest structural similarity with monosulfide compounds, since chemical and crystal-chemical properties of these d -elements are largely determined by the outer ns -electrons [88]. There is an overall similarity in the electronic structure of the valence region in ZnS, CdS and HgS compounds. The structure of the ZnS (sphalerite), CdS (hawleyite), and β -HgS (metacinnabar) monosulfides is based on identical MS_4^{6-} tetrahedral units, but there is a trend toward decreasing stabilization of the main metal-sulfur bonding orbitals across the ZnS-CdS-HgS series. The HgS_2^{2-} linear cluster exists as a basic unit in the cinnabar (α - HgS_{trig}) structure. Cinnabar is a compound with a spiraling system of short Hg–S bonds, with a triple period, which are similar to the Se–Se–Se chains in native selenium, and it is commonly referred to as a distortion derivative of the PbS archetype that has no analogs among ZnS modifications [87].

Both α -HgS (cinnabar, $T_{\text{max}} = 345$ °C) and β -HgS (metacinnabar, $T_{\text{max}} = 572$ °C) polymorphs deviate from stoichiometry, apparently due to intrinsic semiconduction mechanisms (p-type semiconductors) [89], while the natural HgS minerals are commonly cation-deficient compounds [90].

According to single-crystal XRD analyses and Raman spectroscopy, both Hg-poor and Hg-rich Sakhalin sphalerites are single-phase $(\text{Zn,Hg})\text{S}_{\text{cub}}$ compounds. The large Hg ranges in the analyzed grains (Table 10) cause no influence on the diffraction patterns. The high-Hg sphalerite grains are free from both wurtzite and HgS domains.

On the other hand, all analyzed Sakhalin sphalerites with constant elevated Ge and variable Hg contents have a block structure. The disorientation of low- and high-Hg grains turned out to be roughly constant, around 0.90–1.08° (Table 10). Previously, [14] reported a block structure for Ge-rich sphalerites from the Tres Marias Zn deposit (Mexico) and inferred that the disoriented domains in such crystals may be due to the presence of intergrowths between a Fe-Ge-rich 3C sphalerite matrix and Fe-Ge-poor 2H wurtzite lamellae (up to 20%). In our collection of Hg-rich sphalerites, such diffraction patterns were observed only in the Mongolian Hg-sphalerite with the highest (up to 29.48 wt%) and unevenly distributed Hg contents (Table 1). The presence of ~10% wurtzite in this sample (Figure 18) allows us, following [14], to attribute the distinct disorientation (4.88°) to the existence of some ZnS_{hex} domains. The sphalerite-to-wurtzite conversion might be associated with (111) polysynthetic twinning, leading to heterogeneity of the initial $(\text{Zn,Hg})\text{S}$ phase, in which the Hg-sphalerite matrix can host up to ~10% wurtzite. However, the sample has to be further analyzed by transmission electron microscopy, which is currently not possible.

The methods we applied (EDS SEM, microprobe, single-crystal XRD analyses and Raman spectroscopy) have neither revealed any HgS domains in the Mongolian Hg-rich sphalerite sample. Single crystal XRD analyses and Raman spectroscopy were applied to reveal polhemusite, a rare $(\text{Zn,Hg})\text{S}$ tetragon modification [5,6], whose composition partly matches the ranges in our Hg-rich sphalerites $(\text{Zn}_{0.83-0.92}\text{Hg}_{0.10-0.22})\text{S}$; 18.0–34.7 wt% Hg). However, that phase was also absent from the samples of both Sakhalin Island and the Idermeg–Bayan-Khan-Ula polysulfide–fluorite deposit.

Taken together, the results for impurity compositions and structure patterns of the Sakhalin Hg- and Ge-rich sphalerites provide evidence that both elements incorporated isomorphically into the sphalerite structure, with direct $\text{Zn}^{2+} \rightarrow \text{Hg}^{2+}$ substitution and, more likely, heterovalent $\text{Ge}^{4+} + \square \rightarrow 2\text{Zn}^{2+}$ substitution for Ge. For the latter, the reason is that Ge^{4+} shows the sp^3 hybridization typical of Zn^{2+} in the tetrahedral coordination, whereas Ge^{2+} contains one electron pair and requires an excessive, usually asymmetrically situated, structural space for its non-bonding s^2 pair [87]. Unfortunately, the techniques we used failed to reveal fine textural complexity of Ge-rich sphalerites intergrown between 3C sphalerite and 2H wurtzite, like those reported for the Fe-Ge-rich sphalerite from the Tres Marias Zn deposit in Mexico [14].

6.3. Conditions of Sulfide Mineralization and Sources of Material in Ejecta of Sakhalin MVs

The South Sakhalin and Pugachev MVs, the two largest edifices of the Sakhalin province, are located 240 km apart but erupt material of the same chemical and mineralogical type. The mud masses are mainly composed of sandy illite-smectite clay with relatively high percentages of diagenetic kaolinite or sometimes montmorillonite, as well as abundant fine debris of sedimentary or, less often, altered volcano-sedimentary rocks. They are, namely, the Upper Cretaceous Bykovo Formation sandy-clayey rocks and the Krasnoyarsk Formation sandstones that lie over Neogene coaliferous sandstones and tuffaceous sediments in the zone of the Tym-Poronay thrust (Figure 4). The abundance and diversity of the clastic material is due to the location of the two MVs within the damage zone of the Sakhalin largest active Tym-Poronay Fault. Drilling to a depth of 3 km in the area of South Sakhalin MV exposed its feeding channel in heavily faulted Neogene volcanic-sedimentary rocks (Figure 4), which are favorable hosts of Sb-Hg low-temperature hydrothermal mineralization [23,26]. The rocks near the channel dip almost vertically, and it is impossible to reconstruct the depth interval of the mud reservoirs from petrography and lithology of the erupted clastic material. The subsurface structure in the area of Pugachev MV remains poorly constrained, but it must be similar to that of South Sakhalin MV, judging by the similarity of the erupted material.

The temperatures and respective depths of fluid generation for the Sakhalin MVs were estimated by means of hydrochemical geothermometry, with reference to the $45\text{ }^\circ\text{C}/\text{km}$ local geothermal gradient for South Sakhalin MV [29]. The same approach has already been successfully applied to mud volcanic systems in the Taman and Kerch peninsulas, Azerbaijan, and Kakheti (Georgia) [55,91–94]. The fluid generation temperatures ($T_{\text{Mg-Li}}$, $^\circ\text{C}$) were estimated with the Mg–Li geothermometer of [95], which is valid up to $300\text{ }^\circ\text{C}$, using Mg and Li concentrations in mg/L:

$$T_{\text{Mg-Li}} = 2200 / (\log(\sqrt{\text{Mg}/\text{Li}}) + 5.47) - 273 \quad (1)$$

The initial data for calculations were reported previously [42,62,64]. The $T_{\text{Mg-Li}}$ estimates for the MV waters derived from numerous active (bubbling) salsas of South Sakhalin MV and by single gryphons with liquefied mud from Pugachev MV, fall within narrow ranges of 93 to $111\text{ }^\circ\text{C}$ and 102 to $107\text{ }^\circ\text{C}$, respectively. Therefore, the generation depth of MV waters at the two sites must be within 2.0 to 2.5 km , at the $45\text{ }^\circ\text{C}/\text{km}$ thermal gradient.

The South Sakhalin MV waters (Figure 5) are of $\text{HCO}_3\text{-Cl/Na-Mg}$ type, with low $(\text{SO}_4)^-$ and high Ba contents, three orders of magnitude different from the seawater values [42,64]. These waters have extremely high average Li contents ($X_{\text{av.}} = 6.23\text{ ppm}$; $n = 147$), prominent positive Cs, As, and Sb anomalies (Figure 5), and the B/Li ratio around 45, or 2–4 times as low as in the MV waters of Trinidad, Taiwan, and Kerch MV provinces [55]. The selective Li and Cs enrichment of the Sakhalin MV waters, at quite moderate B contents and low Na (lower than in the seawater), may be imprints of tuffaceous material leached by MV waters. This inference is also supported by the presence of abundant two-headed zircons, Cl-F apatites, and rutile free from wear/transport signatures in the erupted material. The genetically different waters circulating in the Tym-Poronay

Fault Zone are enriched in chalcophile elements. They have notable Zn contents, while thermal waters also contain As and Cu, and MV waters show As, Sb and occasionally Pb enrichment. The MV waters in Sakhalin Island, which is located in a wet climate zone, must be diluted with atmospheric precipitation [42,64,67]. The dilution effects (lower concentrations of HCO_3 , Cl, Br, Na, K, Mg, Ca, Li, and As) are commonly observed in the waters of small gryphons. Whereas the MV waters of strongly bubbling salsas are only slightly freshened. The enrichment of the diluted MV waters in the elements of Pb-Sb sulfosalts indicates prolonged interaction with minerals prone to oxidation, under oxic conditions. The oxidative dissolution of sulfosalts most likely occurs in near-surface mud reservoirs, like one discovered by shallow seismic surveys in the 5–40 m depth interval beneath South Sakhalin MV [43,44].

On the other hand, the content of Hg in MV waters is expectedly moderate, given the abundance of Hg as low-solubility sulfide minerals in the mud masses [96]. The Hg contents are quite high (0.64–0.74 ppm) in the As mineral water of Sinegorsk borehole and still higher (0.81 ppm Hg) in the rain of Jebi typhoon (05.09.2018), which arrived at Sakhalin from the Japan islands across the Sea of Japan (Figure 1a), through atmospheric zones of stable Hg enrichment [27].

Most of Hg inputs to the world ocean are by wet and dry atmospheric deposition [97,98]. Atmospheric mercury mainly comes from magmatic volcanoes [99–103], which emit annually 112–700 tons of gaseous Hg^0 in total [100,101]. Eventually, mercury becomes buried in marine sediments [97,98,104]. The sediments deposited in anoxic environments, under the influence of atmospheric Hg fluxes, are commonly enriched in sulfidic Hg, mainly hosted by pyrite [96]. For instance, data on sulfide mineralization in the material erupted by MVs of the Kerch-Taman (Black Sea) province [50,51,54] show that sulfidic Hg makes up 70% of the total mercury budget in the anoxic Oligocene–Lower Miocene Middle Maykop shales (source rocks for the deeply rooted MVs of the region), while the heavy mineral fractions extracted from the mud masses contain abundant Hg-bearing pyrite (up to 4810 $\mu\text{g}/\text{kg}$ total Hg) together with sporadic euhedral crystals of cinnabar. The Hg enrichment of Middle Maykop shales was mainly due to the local Oligocene–Lower Miocene volcanic activity in the Caucasus Continental Collision Zone.

In Neogene-Quaternary time, atmospheric Hg could come to Sakhalin and its water systems from strong eruptions of magmatic volcanoes in the Japan and Kurile islands, which caused substantial short-term increases to the atmospheric Hg in their surroundings [27]. However, the Bykovo and Krasnoyarsk Formations, the main sources of mud volcanic material in the area, were deposited in the Late Cretaceous, in the absence of volcanic activity. The contents of Hg in Upper Cretaceous shales are comparable with the UCC values, as in the mud masses extruded by South Sakhalin MV (Table 3).

Nevertheless, the mud erupted by the Sakhalin MVs bears diverse sulfide mineralization, including Hg species. The sources and formation conditions of this mineralization are constrained below using the approach applied previously to the mud volcanism of the Kerch Peninsula [54]. Generally, the assemblage of sulfide minerals, as well as the trend of selective incorporation of metals into pyrite during diagenesis, fit the model of [96]. The model implies that sedimentary pyrite uptakes metals in the sequence $\text{Mn} > \text{Zn} > \text{Pb} > \text{Cd}$, whereas other metals ($\text{Hg} > \text{As} = \text{Mo} > \text{Cu} \geq \text{Co} > \text{Ni}$) tend to form individual sulfides. Yet, this rule obviously fails in our case: the material erupted by the Sakhalin MVs is rich in Hg and As phases, as well as in sphalerite, galena, and Pb-Sb-(Cu, Bi) sulfosalts but contains only sporadic micrograins of Cu minerals. This composition of sulfides indicates that the mud masses may originate from other sources besides the Cretaceous marine sedimentation.

Pyrites from the Sakhalin MV ejecta generally have low trace-element loading, even the synsedimentary early framboidal pyrite from the Bykovo Formation rocks, which is depleted in all these elements, except for Mn and Ni. The Bykovo and Krasnoyarsk Formations framboidal pyrite contains low to moderate amounts of Hg (~13 ppm on average), while Hg in pyrite crystals is below the detection limit. The Sakhalin pyrites are remarkable

by Tl enrichment (31.0 ppm on average), which lacks in all other sulfides and sulfosalts we studied. Judging by its trace-element chemistry, specific morphology (Figure 6) and high $\delta^{34}\text{S}$ values (Figure 7), pyrite is of diagenetic origin. The Upper Cretaceous shale deposition occurred in a setting of moderate sulfate reduction outside the influence of volcanism, which would supply chalcophile elements, including Hg, to marine sediments.

Galena, Pb-Sb-(Cu,Bi) sulfosalts, realgar, metacinnabar, and cinnabar occur as subangular to rounded grain fragments in the mud masses (Figure 8). This morphology differs from that in pyrite and sphalerite occurring as euhedral grains free from wear signatures (Figures 6 and 9). Such elements as Se, Sb, As, Bi, and Ag are geochemical tracers common for galena and sulfosalts, while metacinnabar may also contain up to 3.4 wt% Se. Many of these minerals are intergrown, which is evidence of their origin from a single source. Hg sulfides were found only in the Pugachev mud masses, especially zincian metacinnabar (sometimes with Se impurity), which crystallized at 295 °C, the minimum value according to the ZnS-HgS diagram (Figure 20). The presence of this sulfidic assemblage accounts for the high contents of Hg, As, Se, Sb and Pb in the heavy fractions extracted from the mud masses (Table 3). The Pb-Sb-(Hg) mineralization, with moderate amounts of As, Cu, Ag, Bi and Se and very low Tl, can be identified as a separate genetical type not related to the Cretaceous marine sedimentation, unlike pyrite.

The new data on the sulfide mineralization of the Sakhalin MV ejecta contribute to the knowledge of metallogeny in the Tym-Poronay Fault zone and confirm the inference that the MV-related Hg-Sb mineralization in the area is of hydrothermal origin [23,35]. Generally, Hg-Sb mineralization within the Tym-Poronay zone is localized at intersections of major and pinnate faults, in the crests of narrow folds, and in the thrust hanging walls. Small ore occurrences in Late Cretaceous strata are associated with fractured brittle tuffaceous sandstones under clay caps [23,26]. The damage zone of MVs (Figure 4) encompasses all lithological and structural features favorable for the generation of Sb-Hg mineralization. Mud volcanism appears to have been the principal transport agent: the pressurized pulp carried to the surface the ore material, which formed during the Neogene volcano-sedimentary events and became entrapped and spread in the mud [23,26]. The sizes and abundances of sulfide mineral grains in heavy fractions decrease markedly on transition from viscous ejecta to liquefied mud, which is additional evidence for the transportation rather than mineral-forming role of the pulp. This inference is further supported by the notable difference between the MV fluid generation temperature ($T_{\text{Mg-Li}}$) and the minimum temperature of zincian metacinnabar crystallization: ~100 °C against 295 °C, respectively (Figure 20).

Sphalerites from two large Sakhalin MVs share similarity in morphology, size distribution and trace-element compositions (except for Hg) between grains, samples and even domes. Consistent SEM-EDS, EPMA, and LA-ICPMS data for representative samples (Tables 4–8), as well as elemental maps (Figures 12 and 13), confirm the uniform distribution of Ge, Cd, Se, and commonly Fe, at highly uneven Hg distribution in the Hg-enriched sphalerites. These sphalerites are remarkable due to their sporadically very high Hg enrichment coupled with permanent abnormal enrichment in Ge (average contents of 3286 ppm and 3195 ppm for Pugachev and South Sakhalin MVs, respectively), which is the highest of reported before [1,14], at uniform Ge distribution recorded in smooth ablation profiles (Figures 15 and 16).

Previously, a wealth of data was used to demonstrate that the trace-element composition of sphalerites was a sensible and reliable proxy of crystallization conditions [1,8,16,86]. According to published evidence [1,3,86], low-temperature sulfide assemblages typically include sphalerites depleted in Fe, Mn, In and Co but containing relatively high amounts of Ga, Ge, Hg and Sn. As noted by [1], the formation temperatures for Ge-rich sphalerite are lower than those for Ga-rich varieties, while In contents are the lowest in Ga-Ge-enriched ores. In terms of these criteria, the Sakhalin MV sphalerites possess the whole scope of trace-element fingerprints common to the lowest-temperature mineral assemblages.

The patterns of trace elements in sphalerites from the Pugachev and South Sakhalin mud masses were compared with those in low-temperature ($T < 200\text{ }^{\circ}\text{C}$) sphalerites from Vein-type and Mississippi Valley-type (MVT) Pb–Zn deposits [1,8,16,105]. The Sakhalin sphalerites turned out to contain much less Tl, Ni, Mn, As (two or three orders of magnitude difference) and Ag, Pb, Sb and Cd (one or two orders of magnitude difference) (Figure 21), but the contents of Ga, Cu, Co, In, and Fe were comparable with those in their counterparts from Vein-type and MVT type deposits (Figure 22). Sporadic spikes of Pb, Bi, Sb, Ag and less often Cu, As and Se in the Sakhalin sphalerites are due to microinclusions of galena and Pb–Sb–(Cu,Bi) sulfosalts.

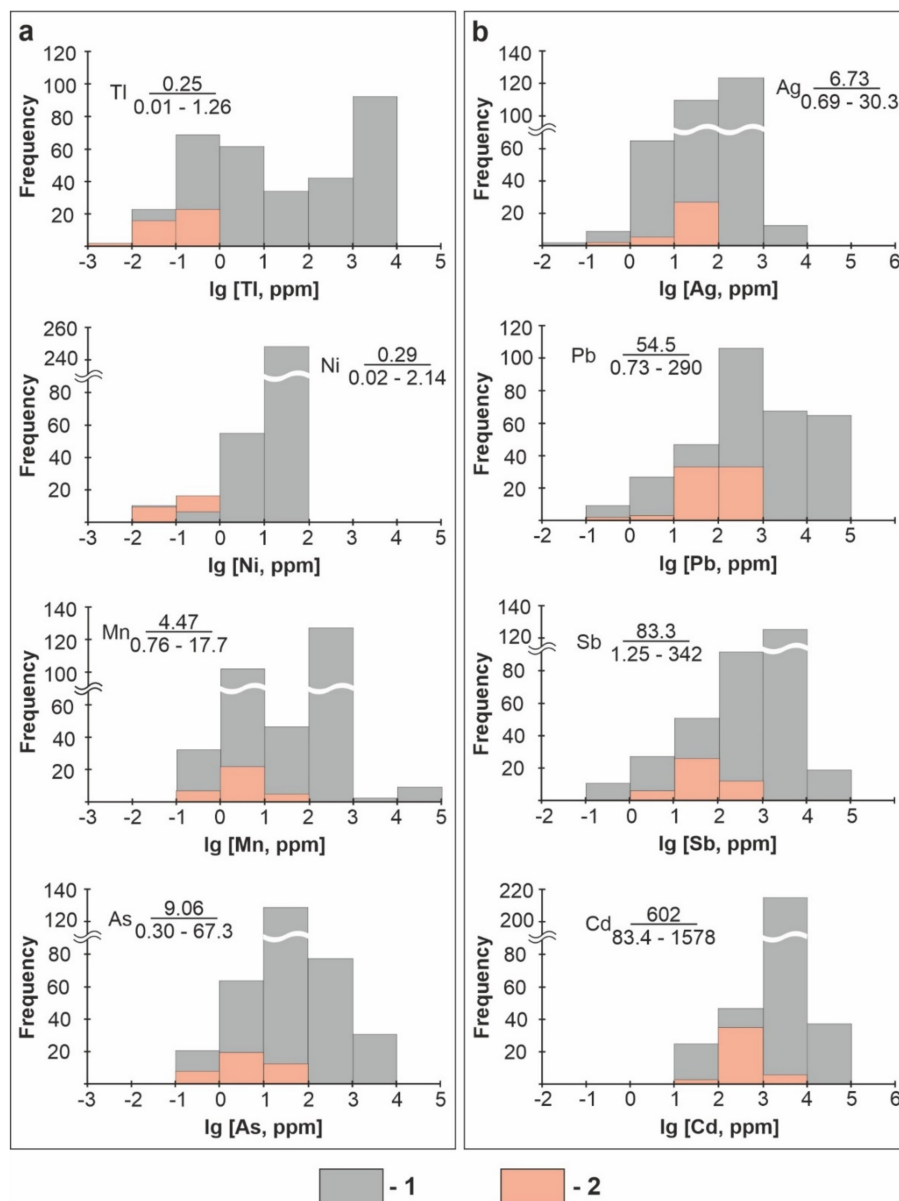


Figure 21. Trace-element contents in sphalerites from Pugachev and South Sakhalin MVs compared to those from the low-temperature ($T < 200\text{ }^{\circ}\text{C}$) sphalerites from different Pb–Zn deposits worldwide: (a) very low, (b) low. 1 = trace-element contents (LA-ICPMS data) in sphalerites from Vein-type and Mississippi Valley-type Pb–Zn deposits of Romania [1], China [8], Germany [16] and Iran [105]. 2 = trace-element contents (LA-ICPMS data) in Sakhalin MVs sphalerites. The numbers next to the histograms are element contents: average values above the bar and the averaging range below the bar.

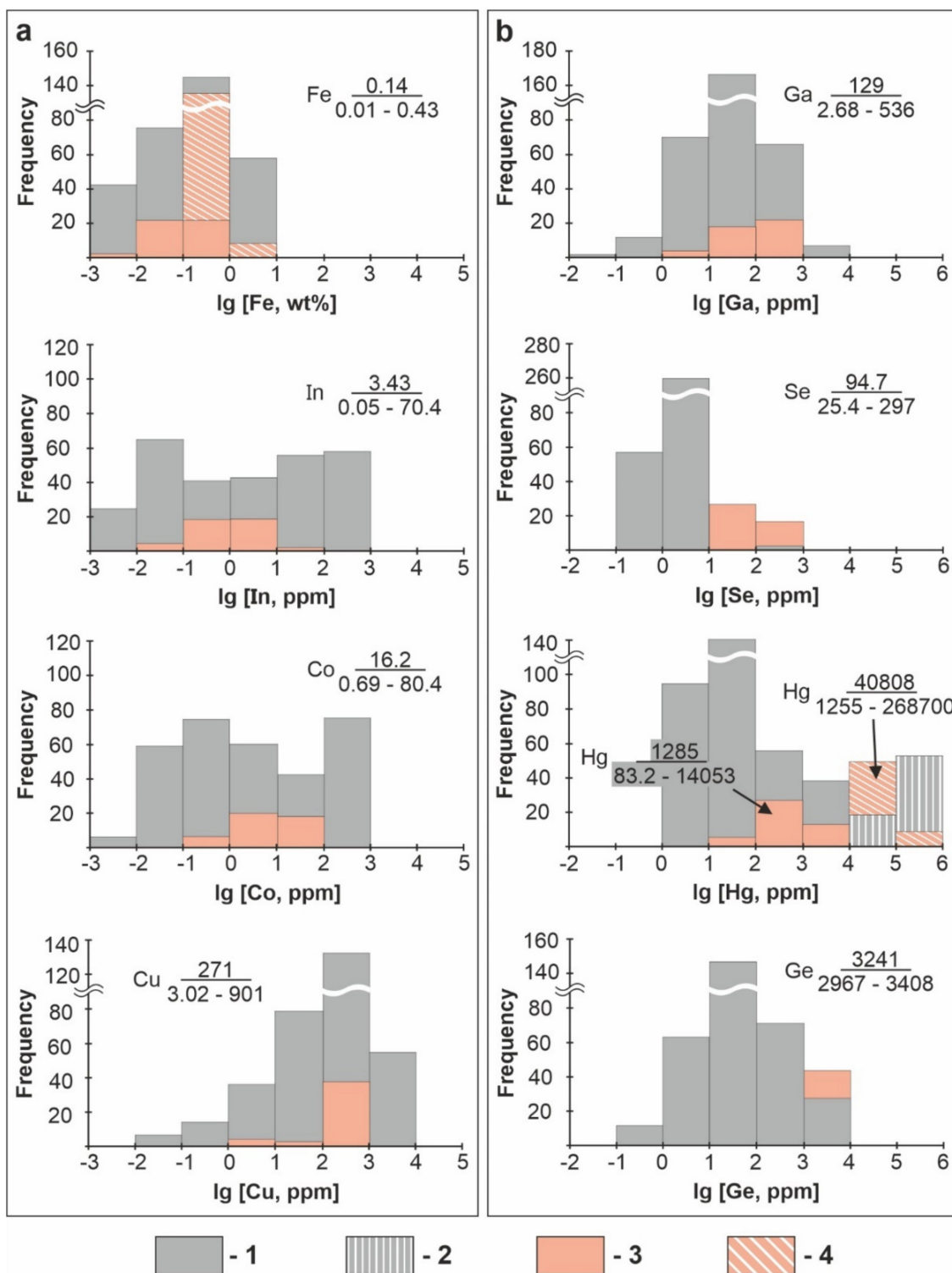


Figure 22. Trace-element contents in sphalerites from Pugachev and South Sakhalin MVs compared to those of low-temperature ($T < 200\text{ }^{\circ}\text{C}$) sphalerites from different deposits worldwide: (a) comparable amounts, (b) abnormal amounts. 1 = trace-element contents in sphalerites (LA-ICPMS data) from Vein-type and Mississippi Valley-type Pb-Zn deposits of Romania [1], China [8], Germany [16] and Iran [105]. 2 = Hg contents in sphalerites (EDS-WDS data) from different Hg deposits of Canada [1], Russia, Ukraine, Mongolia, Kyrgyzstan, Uzbekistan [3], and China [82]. 3 = trace-element contents (LA-ICPMS data) in Sakhalin MVs sphalerites. 4 = Hg contents (EDS-WDS data) in Sakhalin MVs sphalerites. The numbers next to the histograms are element contents: average values above the bar and the averaging range below the bar.

We undertook special efforts to check the homogeneity of the Sakhalin MV sphalerite grains with abnormal concentrations of Ge and Hg (Figure 22) by means of XRD analysis and Raman spectroscopy, but found no inclusions of Hg or Ge phases, which supported the isomorphic incorporation of both Hg and Ge into the sphalerite structure. Compared to the sphalerites of Vein-type and MVT deposits, those from Sakhalin have two orders of magnitude greater contents of Ge (3008–3408 ppm) and one or two orders of magnitude greater Hg contents (83.2 ppm to 27 wt%), even in low- and medium-Hg varieties [2,3,82].

The crystallization temperatures of the Sakhalin sphalerites were estimated using GGIMFis thermometry [86] as

$$PC_1 = \ln ((C_{Ga}^{0.22} \cdot C_{Ge}^{0.22}) / (C_{Fe}^{0.37} \cdot C_{Mn}^{0.20} \cdot C_{In}^{0.11})), \quad (2)$$

with Ga, Ge, In and Mn concentrations in ppm, and Fe concentration in wt%. Using this, we proceeded from the idea [86] that the sphalerite chemistry (especially Ga, Ge, Fe and Mn, and to a lesser degree In) may be strongly controlled by fluid temperature. The empirical relationship between PC_1 and the homogenization temperature (T) of fluid inclusions is:

$$T = -(54.4 \pm 7.3) \cdot PC_1 + (208 \pm 10) \quad (3)$$

Most of GGIMFis geothermometry estimates for the crystallization temperature of the Sakhalin sphalerites fall within a range of 50 to 80 °C, with a maximum of 106 °C. However, the method is reliable between 100 to 400 °C, as noted by [86], who warned against extrapolation beyond this range, as long as the thermodynamics of (or other controls on) the relationship between PC_1 and temperature are not well understood yet. Judging by the composition of impurities, the sphalerites from the Pugachev and South Sakhalin mud masses crystallized at temperatures under ~100 °C, corresponding to the conditions of MV water generation. The absence of intergrowths with other sulfide phases and a unique Ge tracer, along with predominant euhedral crystals and ubiquitous Mg-Ca siderite inclusions, indicate that the Sakhalin sphalerites apparently formed separately from diagenetic pyrite and hydrothermal Pb-Sb-Hg-(Bi, Cu, Se) sulfide assemblages.

The redistribution of Hg-Sb ores was possibly assisted by MV waters, as suggested by [23] who studied the fate of Hg mineralization in rocks mobilized by the Sakhalin mud volcanism. Hot (100 °C) saline MV waters can be efficient leaching agents and may have extracted chalcophile elements (including Zn and Hg) from the disintegrated Neogene volcano-sedimentary rocks. The HCO_3^- -Cl/Na(\pm Mg) MV aqueous fluids interacting with rocks till the 2.0–2.5 km depths of MV roots leached ore components, in the same way as hydrothermal solutions did previously. Low contents of sulfate in the MV waters, the Zn enrichment, high redox potential, and the presence of H_2S provided the conditions for binding zinc to a sulfide. The predominant perfect habits and twinning of the sphalerite crystals, as well as their multi-headed growth with uptake of clay particles, provide evidence for their formation in soft mud.

Inhomogeneous Hg-bearing sphalerite is the main Hg host in the sulfide assemblages from South Sakhalin MV, whereas cinnabar or metacinnabar are absent. The spiky Hg patterns of the sphalerites, with later high-Hg sphalerite making rims around and healing cracks in low-Hg crystals, are consistent either with episodic injections of limited Hg-rich water batches into the mineral-forming system, or with abrupt thermodynamic changes in the solution. In the latter case, the crystallization reactions of sulfides may have involved Hg^{2+} and Zn^{2+} ion species released by the breakdown of Hg and Zn compounds. Note, however, that mercury failed to form its own sulfides, despite the low solubility of HgS phases [96]. In a similar case of marine sediments exposed to diagenesis [96], where Hg is mainly incorporated into pyrite, mercury showed the strongest chloride complexation and highest hydrolysis constant, which should retard its reactivity with S^{2-} and allow it to incorporate into another dominated sulfide, namely FeS_2 . Unlike mercury, which is prone to chloride complexation, zinc in HCO_3^- -Cl/Na(\pm Mg) solutions mainly forms carbonate and bicarbonate complexes. Their breakdown may be induced by abrupt degassing of

HCO₃-rich MV aqueous fluids in the subsurface level. These may be the conditions in which Sakhalin sphalerites could develop their Hg-rich zones.

Neogene coal and coaliferous sediments, found in abundance in the mud masses, especially at South Sakhalin MV, appear to be a unique possible source of high Ge in the Sakhalin MV sphalerites. The latter could only inherit the Hg and Ge enrichment from solutions where the two elements coexisted and reached extremely high concentrations unusual for most of natural settings. They were the MV waters in the damage zones that interacted simultaneously with volcano-sedimentary and coal-bearing rocks. This fact highlights the importance of the major-element diversity at the MV sites and MV water leaching that controlled the geochemical composition of mud erupted by the Sakhalin MVs.

7. Conclusions

The obtained data on the mineralogy and geochemistry of Fe, Zn, Pb, Sb, As, Hg, and Ag sulfide assemblages from mud masses extruded by large South Sakhalin and Pugachev MVs in Sakhalin Island (Russian Far East) lead to the following inferences.

1. All ejecta of the Sakhalin MVs bear unique geochemical signatures, which have never been reported before from any other mud volcanic provinces. The unusual geochemical markers appear in sulfide mineralization of heavy mineral fractions (abundant Zn, Pb, Sb, As, Hg, and Ag phases), as well as in MV water and bulk mud masses with distinct As-, Sb-, Zn-, Pb-, and Ge-enrichment.

2. The geochemical specificity of the Sakhalin MVs must be largely due to their location in a subduction zone, with their feeder channels in the zone of the Tym-Poronay active fault. Mud volcanism in Sakhalin Island mobilized thick mud strata, as well as coexisting rock complexes of different ages, compositions, and origin, including hydrothermally altered volcanoclastics rich in chalcophile elements and Sb-Pb-Hg mineralization, as well as Ge-rich coal-bearing sediments. The elements are transported by two main mechanisms: mechanic transport of disintegrated material with mud masses or leaching of different rocks by hot (up to 100 °C) saline HCO₃-Cl/Na(±Mg) aqueous fluids.

3. The integrated data on the studied sulfide assemblages have implications for their formation conditions and sources of material. The Sakhalin MVs erupt three genetically different groups of sulfides. Authigenic pyrite with poor trace element loading and specific Tl enrichment formed during early diagenesis under depositional conditions with moderate sulfate reduction, at the account of Upper Cretaceous sediments. The Pb-Sb-(Hg, As, Cu, Ag, Bi, Se) sulfides are of hydrothermal origin and source from Neogene volcano-sedimentary strata. Ge-rich sphalerites with variable Hg contents crystallized with participation of saline MV waters, which leached Zn and Hg from Neogene volcano-sedimentary rocks, and Ge from Ge-rich Neogene coal-bearing sediments.

4. The main impurities in the studied MV sphalerites are Hg, reaching 27 wt%, and Ge with constant concentrations of ~3000 ppm, whereas all other impurities (Fe, Cd, Se, Mn and In) typical of the low-temperature sphalerites are low to below detection limit. Most of the mercury in the mud erupted by Sakhalin MVs resides in the intermediate members of the (Zn,Hg)S solid solution series ((Zn_{1.00-0.88}Hg_{0.00-0.12})S and (Hg_{1.00-0.92}Zn_{0.00-0.08})S). Single-crystal XRD and Raman spectroscopy data provide consistent evidence that Ge-rich sphalerite crystals with unevenly distributed Hg are single-phase (Zn,Hg)S_{cub} compounds. Both Hg²⁺ and Ge⁴⁺ are incorporated into the ZnS structure via direct iso- and heterovalent isomorphic substitutions for Zn²⁺, respectively. Zincian metacinnabar crystallized at a temperature no lower than 295 °C, while the reconstructed temperature range for sphalerite is 50 to 106 °C.

Author Contributions: Project idea: E.V.S., S.N.K.; Conceptualization: E.V.S.; Mineralogy: E.V.S., S.N.K., A.V.N., Y.V.S. and A.S.D.; Field work: E.V.S., S.N.K., V.V.E., O.A.N. and A.S.D.; SEM analyses: E.V.S., A.V.N.; EPMA analyses: A.V.N.; LA-ICPMS analysis: A.A.; XRD analysis Y.V.S.; Raman spectroscopy and interpretation: A.S.D. and A.V.N.; Interpretation of analytical data: E.V.S., S.N.K., Y.V.S., A.A. and A.V.N.; Visualization: A.V.N. and S.N.K.; Writing: E.V.S., S.N.K., A.A., Y.V.S. All authors have read and agreed to the published version of the manuscript.

Funding: The study of sulfidic mineralization from the Sakhalin MVs was supported by grant 17-17-01056P from the Russian Science Foundation. Hg-rich sphalerite from the Idermeg–Bayan-Khan-Ula deposit (Mongolia) was analyzed on government assignment to the V.S. Sobolev Institute of Geology and Mineralogy (Novosibirsk).

Data Availability Statement: The data set is presented directly in the present study.

Acknowledgments: We thank the anonymous reviewers for their valuable comments and suggestions, which we accepted with gratitude. We kindly appreciate fruitful scientific collaboration with our colleagues Vasilii Yu. Lavrushin and Altyn Aydarkozhina from Geological Institute Russian Academy of Sciences (Moscow), Elena N. Nigmatulina, Vadim N. Reutsky, Mikhail V. Khlestov, and Zhimnit Badmaeva from V.S. Sobolev Institute of Geology and Mineralogy (Novosibirsk), and Andrey Vishnevsky from Central Siberian Geological Museum of the IGM (Novosibirsk). Special thanks go to T. Perepelova for helpful advice.

Conflicts of Interest: The authors declare no conflict of interest.

References

1. Cook, N.J.; Ciobanu, C.L.; Pring, A.; Skinner, W.; Shimizu, M.; Danyushevsky, L.; Saini-Eidukat, B.; Melcher, F. Trace and minor elements in sphalerite: A LA-ICPMS study. *Geochim. Cosmochim. Acta*. **2009**, *73*, 4761–4791. [[CrossRef](#)]
2. Grammatikopoulos, T.A.; Valeyev, O.; Roth, T. Compositional variation in Hg-bearing sphalerite from the polymetallic Eskay Creek deposit, British Columbia, Canada. *Geochemistry* **2006**, *66*, 307–314. [[CrossRef](#)]
3. Vasil'ev, V.I. New data on the composition of metacinnabar and Hg-sphalerite with an isomorphous Cd admixture. *Russ. Geol. Geophys.* **2011**, *52*, 701–708. [[CrossRef](#)]
4. Dini, A.; Benvenuti, M.; Lattanzi, P.; Tanelli, G. Mineral assemblages in the hg-Zn(Fe)-S system at Levigliani, Tuscany, Italy. *Eur. J. Miner.* **1995**, *7*, 417–428. [[CrossRef](#)]
5. Costagliola, P.; Benvenuti, M.; Tanelli, G.; Cortecchi, G.; Lattanzi, P. The barite-pyrite-iron oxides deposit of Monte Arsiccio (Apuane Alps). Geological setting, mineralogy, fluid inclusions, stable isotopes and genesis. *Boll. Della Soc. Geol. Ital.* **1990**, *109*, 267–277.
6. Leonard, B.F.; Desborough, G.A. Polhemusite, a new Hg-Zn sulfide from Idaho. *Am. Mineralog.* **1978**, *63*, 1153–1161.
7. Höll, R.; Kling, M.; Schroll, E. Metallogenesis of germanium—A review. *Ore Geol. Rev.* **2007**, *30*, 145–180. [[CrossRef](#)]
8. Ye, L.; Cook, N.J.; Ciobanu, C.L.; Yuping, L.; Qian, Z.; Tiegeng, L.; Wei, G.; Yulong, Y.; Danyushevskiy, L. Trace and minor elements in sphalerite from base metal deposits in South China: A LA-ICPMS study. *Ore Geol. Rev.* **2011**, *39*, 188–217. [[CrossRef](#)]
9. Belissant, R.; Boiron, M.C.; Luais, B.; Cathelineau, M. LA-ICP-MS analyses of minor and trace elements and bulk Ge isotopes in zoned Ge-rich sphalerites from the Noailhac-Saint-Salvy deposit (France): Insights into incorporation mechanisms and ore deposition processes. *Geochim. Cosmochim. Acta* **2014**, *126*, 518–540. [[CrossRef](#)]
10. Bonnet, J.; Cauzid, J.; Testemale, D.; Kieffer, I.; Proux, O.; Lecomte, A.; Bailly, L. Characterization of germanium speciation in sphalerite (ZnS) from Central and Eastern Tennessee, USA, by X-ray absorption spectroscopy. *Minerals* **2017**, *7*, 79. [[CrossRef](#)]
11. Wei, C.; Ye, L.; Hu, Y.; Danyushevskiy, L.; Li, Z.; Huang, Z. Distribution and occurrence of Ge and related trace elements in sphalerite from the Lehong carbonate-hosted Zn-Pb deposit, northeastern Yunnan, China: Insights from SEM and LA-ICP-MS studies. *Ore Geol. Rev.* **2019**, *115*, 103175. [[CrossRef](#)]
12. Liu, T.; Zhu, C.; Yang, G.; Zhang, G.; Fan, H.; Zhang, Y.; Wen, H. Primary study of germanium isotope composition in sphalerite from the Fule Pb-Zn deposit, Yunnan province. *Ore Geol. Rev.* **2020**, *120*, 103466. [[CrossRef](#)]
13. Saini-Eidukat, B.; Melcher, F.; Lodziak, J. Zinc-germanium ores of the Tres Marias mine, Chihuahua, Mexico. *Miner. Depos.* **2009**, *44*, 363–370. [[CrossRef](#)]
14. Cook, N.J.; Etschmann, B.; Ciobanu, C.L.; Geraki, K.; Howard, D.L.; Williams, T.; Rae, N.; Pring, F.; Chen, G.; Johannessen, B.; et al. Distribution and substitution mechanism of Ge in a Ge-(Fe)-bearing sphalerite. *Minerals* **2015**, *5*, 117–132. [[CrossRef](#)]
15. Goldmann, S.; Junge, M.; Wirth, R.; Schreiber, A. Distribution of trace elements in sphalerite and arsenopyrite on the nanometre-scale-discrete phases versus solid solution. *Eur. J. Mineral.* **2019**, *31*, 325–333. [[CrossRef](#)]
16. Bauer, M.E.; Burisch, M.; Ostendorf, J.; Krause, J.; Frenzel, M.; Seifert, T.; Gutzmer, J. Trace element geochemistry of sphalerite in contrasting hydrothermal fluid systems of the Freiberg district, Germany: Insights from LA-ICP-MS analysis, near-infrared light microthermometry of sphalerite-hosted fluid inclusions, and sulfur isotope geochemistry. *Miner. Depos.* **2019**, *54*, 237–262. [[CrossRef](#)]
17. Zonenshain, L.P.; Kuzmin, M.I.; Natapov, L.M.; Page, B.M. Sikhote-Alin-Sakhalin Foldbelt. In *Geology of the USSR: A Plate-Tectonic Synthesis*; Zonenshain, L.P., Kuzmin, M.I., Natapov, L.M., Page, B.M., Eds.; AGU: Washington, DC, USA, 1990; pp. 109–120.
18. Maruyama, S.; Isozaki, Y.; Kimura, G.; Terabayashi, M. Paleogeographic maps of the Japanese Islands: Plate tectonic synthesis from 750 Ma to the present. *Isl. Arc.* **1997**, *6*, 91–120. [[CrossRef](#)]
19. Koulakov, I.Y.; Dobretsov, N.L.; Bushenkova, N.A.; Yakovlev, A.V. Slab shape in subduction zones beneath the Kurile-Kamchatka and Aleutian arcs based on regional tomography results. *Russ. Geol. Geophys.* **2011**, *52*, 650–667. [[CrossRef](#)]

20. Koulakov, I.; Serdyukov, A.S.; Konovalov, A.V.; Mikhailov, V.I.; Safonov, D.A.; Duchkov, A.A.; El Khrepy, S. Possible sources of hydrothermal activity and mud volcanism in southern Sakhalin inferred from local earthquake seismic tomography. *Geochem. Geophys. Geosys.* **2017**, *18*, 1943–1958. [[CrossRef](#)]
21. Chelnokov, G.A.; Bragin, I.V.; Kharitonova, N.A. Geochemistry of mineral waters and associated gases of the Sakhalin Island (Far East of Russia). *J. Hydrol.* **2018**, *559*, 942–953. [[CrossRef](#)]
22. Maruyama, S.; Seno, T. Orogeny and relative plate motions: Example of the Japanese Islands. *Tectonophysics* **1986**, *127*, 305–329. [[CrossRef](#)]
23. Rozhdestvensky, V.S. Mercury mineralization of Sakhalin Island. In *Issues of Mercury Metallogeny (Based on Materials from Siberia and the Far East)*; Smirnov, V.I., Kuznetsov, V.A., Radkevich, E.A., Obolensky, A.A., Eds.; Nauka: Moscow, Russia, 1968; pp. 209–217. (In Russian)
24. Khanchuk, A.I. Pre-Neogene tectonics of the Sea-of-Japan region: A view from the Russian side. *Earth Sci.* **2001**, *55*, 275–291. [[CrossRef](#)]
25. Grannik, V.M. Reconstruction of the Sakhalin marginal paleobasin by geological and petrochemical data. *Doklady. Earth Sci.* **2012**, *442*, 215–219. [[CrossRef](#)]
26. Vereshchagin, V.N. The main features of the geological structure of the Sakhalin Island. In *Geology of USSR, Volume XXXIII (Sakhalin Island), Geological Description*; Sidorenko, A.V., Ed.; Nedra: Moscow, Russia, 1970; pp. 29–38. (In Russian)
27. Kalinchuk, V.V.; Astakhov, A.S. Atmochemical mercury dispersion aureoles over active geologic structures of the northern Sea of Japan. *Russ. Geol. Geophys.* **2014**, *55*, 1379–1386. [[CrossRef](#)]
28. Merenkov, A.M. *Mineral Resources of the Sakhalin Region*; Sakhalin Publishing House: Yuzhno-Sakhalinsk, Russia, 2002; pp. 55–74. (In Russian)
29. Veselov, O.V.; Soinov, V.V. The heat flow of Sakhalin and the southern Kuril Islands. In *Structure and Composition of the Sedimentary Cover of the Northwest Pacific Ocean*; Iliev, A.Y., Ed.; Institute of Marine Geology and Geophysics Far Eastern Branch Russian Academy of Sciences: Yuzhno-Sakhalinsk, Russia, 1997; Volume 4, pp. 153–176. (In Russian)
30. Melnikov, O.A.; Ershov, V.V. Mud (gas-water-lithoclastite) volcanism of the Sakhalin Island: History, results and prospects in research. *Vestnik Far East. Branch Russ. Acad. Sci.* **2010**, *6*, 87–93. (In Russian)
31. Kopf, A.J. Significance of mud volcanism. *Rev. Geophys.* **2002**, *40*, 1–2. [[CrossRef](#)]
32. Lobodenko, I.Y. Holocene Tectonic Fractures in the Zones of the Hokkaido-Sakhalin and Central Sakhalin Faults. Ph.D. Thesis, Lomonosov Moscow State University, Moscow, Russia, 2010. (In Russian)
33. Veselov, O.V.; Volgin, P.F.; Lutaya, L.M. Structure of the sedimentary cover of the Pugachevo mud volcano area in Sakhalin: Evidence from geophysical modeling. *Russ. J. Pac. Geol.* **2012**, *6*, 413–422. [[CrossRef](#)]
34. Kovtunovich, Y.M.; Gritsenko, I.I.; Rozhdestvensky, V.B.; Semenov, D.F. *Geology of USSR, Volume XXXIII (Sakhalin Island), Mineral Resources*; Sidorenko, A.V., Ed.; Nedra: Moscow, Russia, 1974; pp. 123–131. (In Russian)
35. Sorochinskaya, A.V.; Shakirov, R.B.; Obzhirov, A.I.; Zarubina, N.V.; Karabtsov, A.A. Gasgeochemical and mineralogical features of mud volcanoes on the Sakhalin Island. *Vestnik Far East. Branch Russ. Acad. Sci.* **2008**, *4*, 58–65. (In Russian)
36. Melnikov, O.A.; Ershov, V.V.; Ung, K.C.; Se, S.R. Dynamics of the gryphon activity of gas-water lithoclastic (mud) volcanoes and their relation to the natural seismicity as exemplified by Yuzhno-Sakhalinsk Volcano (Sakhalin Island). *Russ. J. Pac. Geol.* **2008**, *2*, 397–411. [[CrossRef](#)]
37. Ershov, V.V.; Mel'nikov, O.A. Unusual eruption of the main Pugachevo gas-water-lithoclastic (mud) volcano in Sakhalin during the winter of 2005. *Russ. J. Pac. Geol.* **2007**, *1*, 366–370. [[CrossRef](#)]
38. Melnikov, O.A. On the Dynamics and Origin of the Pugachevo Group of Gas-Water-Lithoclast (“Mud”) Volcanoes on Sakhalin Island: Visual Observations and Orohydrography. *J. Volcanol. Seismol.* **2011**, *5*, 409–420. [[CrossRef](#)]
39. Mishurinskij, D.V.; Ershov, V.V.; Zharkov, R.V.; Kopanina, A.V.; Kozlov, D.N.; Lebedeva, E.V.; Abdullaeva, I.V.; Vlasova, I.I.; Mikhalev, D.V. Geological-geomorphological and landscape-ecological features of the Pugachev Mud Volcano as a basis for organization and information support of the tourist route (Sakhalin Island). *Geosys. Transit. Zones* **2018**, *2*, 398–408. (In Russian) [[CrossRef](#)]
40. Poplavskaya, L.N.; Nagornyykh, T.V.; Fokina, T.A.; Poplavsky, A.A.; Permikin, Y.Y.; Streltsov, M.I.; Kim, C.U.; Safonov, D.A.; Melnikov, O.A.; Obrabin, L.S.; et al. Ulegorsko-Ainu earthquake on August 4, 2000 with MS=7.0, I₀=8-9 (Sakhalin). In *Earthquakes of Northern Eurasia in 2000*; Starovoit, O.E., Ed.; GS RAS: Obninsk, Russia, 2006; pp. 265–284. (In Russian)
41. Melnikov, O.A.; Sergeev, K.F.; Rybin, A.V.; Jarkov, R.V. Nature of mud volcanism: Evidence from the latest active eruption of a mud (gas-water-lithoclastite) volcano in Sakhalin. *Dokl. Earth Sci.* **2005**, *400*, 168–172.
42. Nikitenko, O.A.; Ershov, V.V. Hydrogeochemical characteristic of mud volcanism manifestations on Sakhalin Island. *Geosys. Transit. Zones* **2020**, *4*, 321–350. (In Russian) [[CrossRef](#)]
43. Argentov, V.V.; Zhigulev, V.V.; Melnikov, O.A.; Patrikeev, V.N. The experience in application of small-depth seismic investigations for revealing of structure of the Yuzhny-Sakhalin gas-water-mud volcano. *Tikhookeansk. Geol.* **2001**, *20*, 3–11. (In Russian)
44. Zhigulev, V.V.; Gurinov, M.G.; Ershov, V.V. Deep structure of the Yuzhno-Sakhalinsk mud volcano: Results of multidisciplinary seismic surveys. *Russ. J. Pac. Geol.* **2008**, *2*, 294–298. [[CrossRef](#)]
45. Ershov, V.V.; Levin, B.W.; Mel'nikov, O.A.; Domansky, A.V. Manifestations of the Nevelsk and Gornozavodsk Earthquakes of 2006–2007 in the dynamics of gryphon activity of the Yuzhno-Sakhalinsk Gas-Water-Lithoclastic (Mud) Volcano. *Dokl. Earth Sci.* **2008**, *423*, 1443–1447. [[CrossRef](#)]

46. Ershov, V.V.; Shakirov, R.B.; Melnikov, O.A.; Kopanina, A.V. Variations in the parameters of mud volcanic activity and their relationship with the seismicity of the south of Sakhalin Island. *Reg. Geol. Metallog.* **2010**, *42*, 49–57. (In Russian)
47. Shatsky, V.; Sitnikova, E.; Kozmenko, O.; Palessky, S.; Nikolaeva, I.; Zayachkovsky, A. Behavior of incompatible elements during ultrahigh-pressure metamorphism (by the example of rocks of the Kokchetav massif). *Russ. Geol. Geophys.* **2006**, *47*, 482–496.
48. Sokol, E.V.; Kokh, S.N.; Seryotkin, Y.V.; Deviatiiarova, A.S.; Goryainov, S.V.; Sharygin, V.V.; Khoury, H.N.; Karmanov, N.S.; Danilovsky, V.A.; Artemyev, D.A. Ultrahigh-temperature sphalerite from Zn-Cd-Se-rich combustion metamorphic marbles, Daba Complex, Central Jordan: Paragenesis, chemistry, and structure. *Minerals* **2020**, *10*, 822. [[CrossRef](#)]
49. Shuvaeva, O.V.; Gustaytis, M.A.; Anoshin, G.N. Mercury speciation in environmental solid samples using thermal release technique with atomic absorption detection. *Anal. Chim. Acta* **2008**, *621*, 148–154. [[CrossRef](#)]
50. Kokh, S.N.; Sokol, E.V.; Gustaytis, M.; Sokol, I.A.; Deviatiiarova, A.S. Onshore mud volcanoes as a geological source of mercury: Case study from the Kerch Peninsula, Caucasus continental collision zone. *Sci. Total Environ.* **2021**, *751*, 141806. [[CrossRef](#)]
51. Kokh, S.N.; Sokol, E.V.; Gustaytis, M.A. Mercury Anomaly in Oligocene-Miocene Maykop Group Sediments (Caucasus Continental Collision Zone): Mercury Hosts, Distribution, and Sources. *Minerals* **2021**, *11*, 751. [[CrossRef](#)]
52. Lavrushin, V.Y.; Guliev, I.S.; Kikvadze, O.E.; Aliev, A.A.; Pokrovsky, B.G.; Polyak, B.G. Waters from mud volcanoes of Azerbaijan: Isotopic-geochemical properties and generation environments. *Lithol. Miner. Res.* **2015**, *50*, 1–25. [[CrossRef](#)]
53. Karandashev, V.K.; Leikin, A.Y.; Khvostikov, V.A.; Kutseva, N.K.; Pirogova, S.V. Water analysis by inductively coupled plasma mass spectrometry. *Inorg. Mater.* **2016**, *52*, 1391–1404. [[CrossRef](#)]
54. Sokol, E.; Kokh, S.; Kozmenko, O.; Novikova, S.; Khvorov, P.; Nigmatulina, E.; Belogub, E.; Kirillov, M. Mineralogy and geochemistry of mud volcanic ejecta: A new look at old issues (a case study from the Bulganak field, Northern Black Sea). *Minerals* **2018**, *8*, 344. [[CrossRef](#)]
55. Sokol, E.V.; Kokh, S.N.; Kozmenko, O.A.; Lavrushin, V.Y.; Belogub, E.V.; Khvorov, P.V.; Kikvadze, O.E. Boron in an onshore mud volcanic environment: Case study from the Kerch Peninsula, the Caucasus continental collision zone. *Chem. Geol.* **2019**, *525*, 58–81. [[CrossRef](#)]
56. Lavrent'ev, Y.G.; Karmanov, N.S.; Usova, L.V. Electron probe microanalyses of minerals: Microanalyzer or scanning electron microscope? *Russ. Geol. Geophys.* **2015**, *56*, 1154–1161. [[CrossRef](#)]
57. Sharygin, V.V.; Yakovlev, G.A.; Wirth, R.; Seryotkin, Y.V.; Sokol, E.V.; Nigmatulina, E.N.; Karmanov, N.S.; Pautov, L.A. Nataliakulikite, $\text{Ca}_4\text{Ti}_2(\text{Fe}^{3+}, \text{Fe}^{2+})(\text{Si}, \text{Fe}^{3+}, \text{Al})\text{O}_{11}$, a new perovskite-supergrout mineral from Hatrurim Basin, Negev Desert, Israel. *Minerals* **2019**, *9*, 700. [[CrossRef](#)]
58. Sharygin, V.V. Phase CuCrS_2 . In *Iron Meteorite Uakit (IIAB), Buryatia, Russia: Preliminary Data*; Earth and Environmental Sciences Book Series, Minerals: Structure, Properties, Methods of Investigation; Votyakov, S., Kiseleva, D., Grokhovsky, V., Shchapova, Y., Eds.; Springer: Berlin/Heidelberg, Germany, 2020; pp. 229–236.
59. Goldstein, J.I.; Newbury, D.E.; Echlin, P.; Joy, D.C.; Lyman, C.E.; Lifshin, E.; Sawyer, L.; Michael, J.R. Quantitative X-ray Analysis: The Basics. In *Scanning Electron Microscopy and X-ray Microanalysis*; Springer: Berlin/Heidelberg, Germany, 2003; pp. 391–451. [[CrossRef](#)]
60. Sheldrick, G.M. Crystal structure refinement with SHELXL. *Acta Crystallogr. Sect. C Struct. Chem.* **2015**, *71*, 3–8. [[CrossRef](#)] [[PubMed](#)]
61. Ershov, V.V.; Shakirov, R.B.; Obzhairov, A.I. Isotopic-geochemical characteristics of free gases of the South Sakhalin mud volcano and their relationship to regional seismicity. *Dokl. Earth Sci.* **2011**, *440*, 1334–1339. [[CrossRef](#)]
62. Nikitenko, O.A.; Ershov, V.V.; Perstneva, J.A.; Bondarenko, D.D.; Baloglanov, E.E.; Abbasov, O.R. Substance composition produced by mud volcanoes of Sakhalin Island and Azerbaijan: The first comparison. *Geosys. Transit. Zones* **2018**, *2*, 346–358. (In Russian) [[CrossRef](#)]
63. Ershov, V.V. On the problem of variability of the chemical composition for mud-volcanic waters using the example of the Yuzhno-Sakhalinsk mud volcano. *Rus. J. Pac. Geol.* **2017**, *11*, 73–80. [[CrossRef](#)]
64. Nikitenko, O.A.; Ershov, V.V.; Levin, B.W. The first identification of hydrogeochemical indicators of mud volcanic activity. *Dokl. Earth Sci.* **2017**, *477*, 1445–1448. [[CrossRef](#)]
65. You, C.F. Thermal ionization mass spectrometry techniques for boron isotopic analysis: A review. In *Handbook of Stable Isotope Analytical Techniques*, 1st ed.; de Groot, P.A., Ed.; Elsevier: Amsterdam, The Netherlands, 2004; Volume 1, pp. 142–152.
66. Ershov, V.V.; Nikitenko, O.A.; Perstneva, Y.A. Geochemistry of mud and fluid migration in mud volcanoes. *Vestn. Far East. Branch Russ. Acad. Sci.* **2016**, *5*, 52–58. (In Russian)
67. Chudaeva, V.A.; Chudaev, O.V.; Yurchenko, S.G. Chemical composition of precipitation in the southern part of the Russian Far East. *Water Res.* **2008**, *35*, 58–70. [[CrossRef](#)]
68. Bruland, K.W.; Lohan, M.C. Controls of trace metals in seawater. In *Treatise on Geochemistry: The Oceans and Marine Geochemistry*; Elderfield, H., Ed.; Elsevier: New York, NY, USA, 2004; Volume 6, pp. 23–47.
69. Burton, J.D. The Ocean: A Global Geochemical System. In *Oceanography an Illustrated Guide*; Summerhayes, C.P., Thorpe, S.A., Eds.; CRC Press: Boca Raton, FL, USA, 1996; pp. 165–181.
70. Rudnick, R.L.; Gao, S. Composition of the continental crust. In *The Crust. Treatise on Geochemistry*, 1st ed.; Rudnick, R.L., Ed.; Elsevier: Amsterdam, The Netherlands, 2003; Volume 3, pp. 1–64.
71. Rickard, D. Sulfidic Sediments and Sedimentary Rocks. In *Developments in Sedimentology*; van Loon, A.J., Ed.; Elsevier: Amsterdam, The Netherlands, 2012; Volume 6.

72. Buzatu, A.; Buzgar, N.; Damian, G.; Vasilache, V.; Apopei, A.I. The determination of the Fe content in natural sphalerites by means of Raman spectroscopy. *Vib. Spectrosc.* **2013**, *68*, 220–224. [[CrossRef](#)]
73. Bernstein, L.R. Germanium geochemistry and mineralogy. *Geochim. Cosmochim. Acta* **1985**, *49*, 2409–2422. [[CrossRef](#)]
74. Johan, Z.; Oudin, E.; Picot, P. Analogues germanifères et gallifères des silicates et oxydes dans les gisements de zinc des Pyrénées centrales, France. argutite et carboirite, deux nouvelles espèces minérales. *Tscherm. Mineral. Petrogr. Mitt.* **1983**, *31*, 97–119. [[CrossRef](#)]
75. Johan, Z.; Oudin, E. Présence de grenats, $\text{Ca}_3\text{Ga}_2(\text{GeO}_4)_3$, $\text{Ca}_3\text{Al}_2((\text{Ge}, \text{Si})\text{O}_4)_3$ et d'un équivalent ferrifère, germanifère et gallifère de la sapphirine, $\text{Fe}_4(\text{Ga}, \text{Sn}, \text{Fe})_4(\text{Ga}, \text{Ge})_6\text{O}_{20}$, dans la blende des gisements de la zone axiale pyrénéenne. Conditions de la formation des phases germanifères et gallifères. *C. R. Acad. Sci. Ser. IIA* **1986**, *303*, 811–816.
76. Johan, Z. Indium and germanium in the structure of sphalerite: An example of coupled substitution with copper. *Mineral. Petrol.* **1988**, *39*, 211–229. [[CrossRef](#)]
77. Cassard, D.; Chabod, J.C.; Marcoux, E.; Bourguin, B.; Castaing, C.; Gros, Y.; Kosakevich, A.; Moisy, M.; Viallefond, L. Mise en place et origine des minéralisations du gisement à Zn, Ge, Ag, (Pb, Cd) de Noailhac—Saint-Salvy (Tarn, France). *Chron. Recherche Minière* **1996**, *514*, 3–37.
78. Moh, G.H.; Jäger, A. *Phasengleichgewichte des Systems Ge-Pb-Zn-S in Relation zu Germanium-Gehalten Alpiner Pb-Zn-Lagerstätten; Verhandlungen der Geologischen Bundesanstalt*: Vienna, Austria, 1978; pp. 437–440.
79. Gruzdev, V.S. Isomorphism of zinc and mercury in natural sphalerites and metacinnabarites. *Dokl. USSR Acad. Sci.* **1975**, *225*, 661–664. (In Russian)
80. Vasiliev, V.I.; Lavrentiev, Y.G. New findings of mercury-containing sphalerites and their significance. *Geol. Geophys.* **1976**, *1*, 48–53. (In Russian)
81. Powell, W.G.; Pattison, D.R. An exsolution origin for low-temperature sulfides at the Hemlo gold deposit, Ontario, Canada. *Econ. Geol.* **1997**, *92*, 569–577. [[CrossRef](#)]
82. Liu, J.; Rong, Y.; Zhang, S. Mineralogy of Zn-Hg-S and Hg-Se-S Series Minerals in Carbonate-Hosted Mercury Deposits in Western Hunan, South China. *Minerals* **2017**, *7*, 101. [[CrossRef](#)]
83. Tonkachev, D.E.; Chareev, D.A.; Tagirov, B.R.; Merkulova, M.V.; Trigub, A.L.; Vikentiev, I.V.; Kovalchuk, E.V. Chemical state of Hg in synthetic crystals of Hg-sphalerite and Zn-metacinnabarite according to X-ray absorption spectroscopy. In Proceedings of the IX Russian Scientific School with International Participation, Moscow, Russia, 25–29 November 2019; Institute of Geology of Ore Deposits, Petrography, Mineralogy and Geochemistry of Russian Academy of Sciences: Moscow, Russia, 2019. (In Russian).
84. Tauson, V.L.; Abramovich, M.G. A Study of the System ZnS-HgS by the Hydrothermal Method. *Geochem. Int.* **1980**, *17*, 117–128.
85. Osadchii, E.G. The kesterite-velikite ($\text{Cu}_2\text{Zn}_{1-x}\text{Hg}_x\text{SnS}_4$) and sphalerite-metacinnabarite ($\text{Zn}_{1-x}\text{Hg}_x\text{S}$) solid solutions in the system Cu_2SnS_3 -ZnS-HgS at temperatures of 850°, 700° and 500 °C. *Neues Jahrbuch für Mineralogie. Monatshefte* **1990**, *H1*, 13–34.
86. Frenzel, M.; Hirsch, T.; Gutzmer, J. Gallium, germanium, indium, and other trace and minor elements in sphalerite as a function of deposit type—A meta-analysis. *Ore Geol. Rev.* **2016**, *76*, 52–78. [[CrossRef](#)]
87. Makovicky, E. Crystal structures of sulfides and other chalcogenides. *Rev. Mineral. Geochem.* **2006**, *61*, 7–125. [[CrossRef](#)]
88. Rickard, D.; Luther, G.W., III. Metal sulfide complexes and clusters. *Rev. Mineral. Geochem.* **2006**, *61*, 421–504. [[CrossRef](#)]
89. Pearce, C.I.; Patrick, R.A.; Vaughan, D.J. Electrical and magnetic properties of sulfides. *Rev. Mineral. Geochem.* **2006**, *61*, 127–180. [[CrossRef](#)]
90. Fleet, M.E. Phase equilibria at high temperatures. *Rev. Mineral. Geochem.* **2006**, *61*, 365–419. [[CrossRef](#)]
91. Lavrushin, V.Y.; Kopf, A.; Deyhle, A.; Stepanets, M.I. Formation of mud-volcanic fluids in Taman (Russia) and Kakhetia (Georgia): Evidence from boron isotopes. *Lithol. Miner. Res.* **2003**, *38*, 120–153. [[CrossRef](#)]
92. Ershov, V.V.; Levin, B.V. New data on the material composition of mud volcano products on Kerch Peninsula. *Dokl. Earth Sci.* **2016**, *471*, 1149–1153. [[CrossRef](#)]
93. Kikvadze, O.E.; Lavrushin, V.Y.; Polyak, B.G. Chemical geothermometry: Application to mud volcanic waters of the Caucasus region. *Front. Earth Sci.* **2020**, *14*, 738–757. [[CrossRef](#)]
94. Lavrushin, V.Y.; Aydarkozhina, A.S.; Sokol, E.V.; Chelnokov, G.A.; Petrov, O.L. Mud Volcanic Fluids of the Kerch–Taman Region: Geochemical Reconstructions and Regional Trends. Communication 1: Geochemical Features and Genesis of Mud-Volcanic Waters. *Lithol. Miner. Res.* **2021**, *56*, 461–486. [[CrossRef](#)]
95. Kharaka, Y.K.; Mariner, R.H. Chemical geothermometers and their application to formation waters from sedimentary basins. In *Thermal History of Sedimentary Basins. Methods and Case Histories*; Naeser, N.D., McCulloh, T.H., Eds.; Springer: New York, NY, USA, 1989; pp. 99–117. [[CrossRef](#)]
96. Morse, J.W.; Luther, G., III. Chemical influences on trace metal-sulfide interactions in anoxic sediments. *Geochim. Cosmochim. Acta* **1999**, *63*, 3373–3378. [[CrossRef](#)]
97. Fitzgerald, W.F.; Lamborg, C.H.; Hammerschmidt, C.R. Marine biogeochemical cycling of mercury. *Chem. Rev.* **2007**, *107*, 641–662. [[CrossRef](#)]
98. Gworek, B.; Bemowska-Kalabun, O.; Kijeńska, M.; Wrzosek-Jakubowska, J. Mercury in marine and oceanic waters—A review. *Water Air Soil Pollut.* **2016**, *227*, 1–19. [[CrossRef](#)]
99. Ferrara, R.; Mazzolai, B.; Lanzillotta, E.; Nucaro, E.; Pirrone, N. Volcanoes as emission sources of atmospheric mercury in the Mediterranean basin. *Sci. Total Environ.* **2000**, *259*, 115–121. [[CrossRef](#)]

100. Nriagu, J.; Becker, C. Volcanic emissions of mercury to the atmosphere: Global and regional inventories. *Sci. Total Environ.* **2003**, *304*, 3–12. [[CrossRef](#)]
101. Pyle, D.M.; Mather, T.A. The importance of volcanic emissions for the global atmospheric mercury cycle. *Atmos. Environ.* **2003**, *37*, 5115–5124. [[CrossRef](#)]
102. Witt, M.L.I.; Mather, T.A.; Pyle, D.M.; Aiuppa, A.; Bagnato, E.; Tsanev, V.I. Mercury and halogen emissions from Masaya and Telica volcanoes, Nicaragua. *J. Geophys. Res. Solid Earth* **2008**, *113*, B06203. [[CrossRef](#)]
103. Mason, R.P. Mercury emissions from natural processes and their importance in the global mercury cycle. In *Mercury Fate and Transport in the Global Atmosphere*; Masson, R., Pirrone, N., Eds.; Springer: Boston, MA, USA, 2009; pp. 173–191. [[CrossRef](#)]
104. Mason, R.P.; Choi, A.L.; Fitzgerald, W.F.; Hammerschmidt, C.R.; Lamborg, C.H.; Soerensen, A.L.; Sunderland, E.M. Mercury biogeochemical cycling in the ocean and policy implications. *Environ. Res.* **2012**, *119*, 101–117. [[CrossRef](#)] [[PubMed](#)]
105. Zhuang, L.; Song, Y.; Liu, Y.; Fard, M.; Hou, Z. Major and trace elements and sulfur isotopes in two stages of sphalerite from the world-class Angouran Zn-Pb deposit, Iran: Implications for mineralization conditions and type. *Ore Geol. Rev.* **2019**, *109*, 184–200. [[CrossRef](#)]